



UNIVERSITY OF MILANO-BICOCCA

Faculty of Mathematical, Physical and Natural Sciences
Department of Materials Science

PhD in Nanostructures and Nanotechnologies

**COMPUTATIONAL AND EXPERIMENTAL
CHARACTERIZATION OF SELF-ASSEMBLING PEPTIDES
FOR NANOBIO MEDICAL APPLICATIONS**

Author: FRANCESCA TARABALLI

Cycle: XXII – 2006/2009

Tutor: Dr. RITA GRANDORI

Supervisors: Dr. FABRIZIO GELAIN, Prof. ANGELO VESCOVI

*To my big family
and to all my friends*

*What I want to talk about is the problem of
manipulating and controlling things on a small scale.*

Richard Feynman

INDEX

1	ABSTRACT	4
2	AWNKOLEDGMENTS	6
3	BACKGROUND	8
3.1	Nanotechnology and Biology	8
	<i>3.1.1 <u>Nanotechnology in Medical Diagnostic</u></i>	10
	<i>3.1.2 <u>Nanotechnology in Therapies</u></i>	10
	<ul style="list-style-type: none">• <i>Vaccination</i>• <i>Gene Therapy</i>• <i>Drug delivery</i>• <i>Cell Therapy and Regenerative Medicine</i>	11 11 11 12
3.2	Biomaterials	12
	<i>3.2.1 <u>Natural Materials</u></i>	13
	<i>3.2.2 <u>Synthetic Materials</u></i>	14
	<i>3.2.3 <u>SemiSynthetic Materials</u></i>	15
	<i>3.2.4 <u>Design of Nanostructures</u></i>	16
	<ul style="list-style-type: none">• <i>Electrospinning</i>• <i>Self- assembling</i>• <i>Phase separation</i>	16 17 18
	<i>3.2.5 <u>Nanostructured materials design for nervous regeneration</u></i>	19
3.3	Structural characterization of self-assembling peptides	21
	<i>3.3.1 <u>Computational characterization</u></i>	22

•	<i>All atoms model</i>	22
•	<i>Coarse-grained model</i>	26
	3.3.2 <u><i>Experimental characterization</i></u>	28
•	<i>Spectroscopic techniques</i>	28
•	<i>Imaging techniques</i>	32
4	MATERIALS AND METHODS	34
4.1	Synthesis and purification of self-assembling peptides	34
4.2	AFM imaging	34
4.3	Raman spectra collection and analysis	35
4.4	ATR/FTIR spectra collection and analysis	36
4.5	Thermal denaturation follows by FTIR in D₂O	37
4.6	Molecular Dynamic Simulation scheme	38
4.7	Neural stem cell cultures growth on self-assembling peptides	38
4.8	Biopolymer electrospinning and tube synthesis	39
4.9	Histochemical, immunofluorescence and immunoistochemical analysis	40
5	RESULTS AND DISCUSSION	41
5.1	From the theory to the new design and <i>in vitro</i> application	41
	5.1.1 <u><i>Effect of functionalization on the self-assembling propensity of β-sheet forming peptides</i></u>	41
	5.1.2 <u><i>Glycine-Spacers Influence Functional Motifs Exposure and Self-Assembling Propensity of Functionalized Substrates Tailored for Neural Stem Cell Cultures</i></u>	54

5.1.3	<i>Further investigations about hydrophobic component in nanostructure stabilization</i>	64
5.2	Example of biomaterial application <i>in vivo</i>	67
5.2.1	<i>Electrospun micro- and nanofiber tubes for functional nervous regeneration in sciatic nerve transections</i>	67
6	WORK IN PROGRESS	75
7	CONCLUSIONS	77
8	APPENDIX	79
9	BIBLIOGRAFY	81

1 ABSTRACT

The design and application of bionanotechnologies aimed at the nervous system provide powerful new approaches for studying cell and molecular biology and physiology. The successful development of bionanotechnologies designed to interact with the nervous system as research or clinical tools requires an understanding of the relevant neurophysiology and neuropathology, and an understanding of the relevant chemistry and materials science and engineering.

Materials designed molecularly for regeneration of tissues are becoming of great interest in advanced medicine and improvements in the understanding of self-assembly process offer new opportunities in molecular design of biomaterials for vary applications.

In this project, two classes of biomaterials were studied with the same final achievement: the application to the regeneration of nervous systems.

RADA16-I (AcN-RADARADARADARADA-CNH₂), representative of a class of self-assembling peptides with alternate hydrophobic and hydrophilic residues, self-assembles into β -sheet bilayer filaments. Though molecular studies for this class of peptides has been recently developed, new investigations are required to explain how RADA16-I functionalization with biological active motifs, may influence the self-assembling tendency of new functionalized peptides (FP). Since FPs recently became a promising class of biomaterials, a better understanding of the phenomenon is necessary to design new scaffolds for cell biology and nanobiomedical applications.

The first part of this project was based on the investigation with computational and experimental tools about the self-assembly of different FPs showing diverse sequences and "in vitro" behaviors. For the first time spectroscopic techniques (Raman and ATR/FTIR) was applied to these class of peptides and new vibrational modes were used to describe the nanostructure. Thanks to molecular dynamic simulations it was possible increase the experimental findings. The functionalizing self-assembling peptides can strongly influence or prevent assembly into nanostructure. Moreover the designing strategies were enhanced thanks to a deep investigation about the Glicines hinge between self assembling core and biological functionalization. The study of this structural group involved a refinement of a functionalized self-assembling peptide with the direct application on neural stem cells, and a then a future *in vivo* application.

In the second part of this project electrospun tubes, formed by micro and nanofibers, were used to regenerate a 10-mm nerve gap in rat

sciatic nerve *in vivo*. This work provided evidence that electrospun micro- and nanofiber PCL/PLGA channels are promising bioabsorbable scaffolds for stimulating and guiding peripheral nerve regeneration in rat models of sciatic nerve transection. This nanotechnological approach shows very encouraging results in peripheral nervous system regeneration that can ameliorate with surgery shrewdness, rehabilitative training and biomaterial modification, or better a combination of both eletrospun and self-assembling fibers.

Finally in this project it was shown how a deeply investigation about self-assembling process, starting from theoretical part, could be applied directly in the development of many new biomaterials for specific nanobiomedical applications with the hope of increasing of the application range.

2 ACKNOWLEDGMENTS

I know that this section could seem too prolix, but in my opinion the acknowledgments for a PhD thesis are mandatory.

By first I want to give thanks to Prof. A.L. Vescovi and also to Dr. F. Gelain because they always believed in my faculties and because they trust in me for the entire period of my doctorate. I want acknowledge Prof. A. Paleari for the patience that he shown for three years to collaborate with a biochemist and because he taught me all the physics that I know. Many thanks go also to Prof. R. Grandori because she was a very good tutor for the whole PhD school period. Special thanks go to Dr. L.D. Unsworth because he had the painful job to be the reviewer of this thesis.

This thesis project was developed also in other university spread in the world, so I want to acknowledge my foreign collaborator: Prof. W. Hwang for his huge expertise in molecular dynamic simulations that he passed on me in the middle of nowhere (Texas A&M University), also Dr. S. Whitelam because it was the first that introduce me to Monte Carlo simulations.

I am pretty sure that this project might never be finished without the support of my coworkers.

First of all, special thanks go to Dr. Silvia Panseri because we approached to the research world together, we helped and supported each other day by day for three long years, for this reason I will bring her always in my heart not only like a coworker but like a friend. I want acknowledge also Dr. Livia Modica to be the first undergraduate student that worked with me, and she will be always my favorite undergrad. My work was done in three different places that I summarize in biological lab, materials science lab and foreigners lab.

The biological lab: very special thanks goes to Dr. Carla Dos Santos Cunha (and the future family) because she learnt me portuguese language and culture, sometimes also something about stem cells, Dr. Omar Villa (the chemist friend) because we spent together a beautiful period in California even if not for vacation (and also because we share the hate for some amino acids) and Dr. Stefania (Antuàn) Antonini because she went to fill a big lack and she made supergood. Thanks also to Dr. Elena Binda and Dr. Alberto Visioli for our sacred breaks spent together. Thanks to the fashion office: Dr. L. Rota Nodari, Dr. D. Ferrari and L. de Filippis to be always trend-setter. Thanks also to Dr. Laura Russo (Dottoressa). I want also to acknowledge all the undergraduate students that stayed in these years in the lab, and all the people that then went everywhere.

The materials science lab: I want acknowledge in particular way Dr. Roberto Lorenzi and Dr. Alessandro Lauria because they taught me a lot of physics stuff in a very funny manner, and I hope that they learnt from me a lot of interesting biological skills. I want to give thanks also to Dr. N. Chiodini for his hysterical mood, but also for his exciting songs and tails, and sometimes for his huge expertise in inorganic chemistry. Thanks to Dr. M. Campione for the 2 thousands hours spent together at the AFM looking a PC screen. Thanks to Dr. Federico Moretti, Dr. Alessia LeDonne, Dr. Mauro Fasoli and all to the other undergrad students. Special thanks to Dr. Luca Lamagna for the period spent together at the doctorate courses and our meeting abroad.

The foreign labs: special thanks go to the Texas A&M coworker, Dr. Sirish Kaushik Lakkaraju and Dr. Krishnakumar Mayuram Ravikumar because they were my first teachers of statistical mechanics, and Dr John Noel and his wife and dog for the exciting moments spent togheter. I want acknowledge also the people met at the Molecular Foundry and their support to my last period of doctorate: Dr. Ron Zuckermann, Dr. Dina Mirijanian, Heater Jensen, Dr. Cheryl Goldbeck, and Dr. Byoung-Chul Lee and the entire Italians supporter, Dr M. Moretti, Ing. V. Giacometti, Ing. F. Dutto, Ing. S. Stassi, Ing. S. Rigante, Ing. L. Mazzucchetti, Ing. R. Movva, Ing. F. Bartoloni and Ing. L. Maserati.

It is mandatory acknowledge all my friends outside the research world, the problem is that they are really a lot of persons so I hope to remember them all. The first special thanks goes to "the father of my sons" Desiree Terenghi because she always trust in me better than me, and the second cowner goes to the "rich manager aunt of my sons" Penza (fiore) to be at my side since I was 4 years old, and so I am pretty sure that she knows me better than me. First come women, so...thanks to all my girlfriends: Sarini (you see that at the end I did it), Aura (forever at my side), Kappina, Cinzi, CICCIfemale (Silvia), Eliana, The Little Marghe, LauraFerretti, Grazia, Chicca, Laura and Diana (the magic trio), Betta and her new family, Giulia, Laura, Nico ,Vale and Mara.

Special thanks go to: Melus to support and help me always in spite of physical distance, to Richino to make me feel good every times I need. To the entire group Comfortable: Ceppo (our favorite Wales boy), Lucino (CICCImale) and our beautiful song (surfin'bird), Kattà (thanks for our philosophic dissertation), Folle (i want to be your secretary), Biella (and the night spent at his house), Luchino (in Brasil), Stallone (KurtCobain), Mirko, Piero, and Ciccia. Special thanks to my Nerds friends: Sergio (one day we will meet each other at the Nobel Conference), Luca and Lawrence. There will be also a place in my heart (così) for Dario and (unpo'menodicosi) for Glenn.

Last, but for this reason the most important, (as the authors order), I want to thank my family: my Father for the patience and my Mother for trusting in my scientific faculties, my sister Michela with my niece Erika (I hope she will make better than me), my sister Elena, Mariano and their two cute babies and my brother Federico, for their constant and unwavering support during all my life. I want acknowledge also my uncle Antonio, Andrea and Aziz for the many dinners spent to make fun of my parents. Special thanks go also to my Aunt Sandra and my cousin Michele and all the Tuscany relatives (Davide, Antonella, Valeria, Andrea, and Gino).

3 BACKGROUND

3.1 Nanotechnology and Biology

The broad field of Nanotechnology has undergone explosive growth and development over the past 10 years. There isn't any science field in the history more interest or larger government investment. The reasons of this involvement are principally two: first, interest is due to understanding the chemical and physical property of nanostructure, often surprisingly different from the bulk materials from which come from, and second the use of these "new" properties in the development of novel devices and materials can impact and transform many aspect of modern life. The Project on Emerging Nanotechnologies estimates over 800 new nanotech products available at the end of 2008 (<http://www.nanotechproject.org/>) involved in many different life facets, as energy, clothes, cosmetics, medicine, informatics and so on.

The branch of Nanotechnology with biological application is called Nanobiotechnology. There is not a correct definition of this applied science but often is defined as an overlapping multidisciplinary activity (chemistry, biology, biophysics and engineering) that exploits the elements of Nature in order to fabricate new devices. Indeed, advances in Nanobiotechnology have the potential to make a revolution in the old concept of Medicine. This branch of science has many different faces that all share a central concept: the ability to design molecular machinery to atomic specification. Macroscopic structures will be built to atomic precision with existing biomolecular assemblers or using biological models. Sometimes the aims of Nanobiotechnology were taken with skepticism; instead the firs nano-molecular diagnostic systems are commercially available from 2007. However, nanoscale materials technology has already found widespread use in medicine (also called Nanomedicine), including biocompatible materials and analytical techniques, surgical and dental practice, nerve cell research using intracellular electrodes, biostructures research and biomolecular research using near-field optical microscopy, scanning-probe microscopy and optical tweezers, and vaccine design, and also many 20th century bulk chemical and biochemical manufacturing techniques along with much of classical pharmacology (Riehemann et al 2009).

As for "biotechnology," the original meaning of this word contemplated "the application of biological systems and organisms to technical and industrial processes". In recent times, the field has expanded to include genetic engineering and now takes as its ultimate goal no less than the engineering of all biological systems, even completely artificial organic living systems, using biological instrumentalities.

Nanomedicine refers to future developments in medicine that will be based on the ability to build nanorobots. In the future these nanorobots could actually be programmed to repair specific diseased cells, functioning in a similar way to antibodies in our natural healing processes.

In the Table 1 is shown a partial nanomedicine technologies taxonomy. Although nanomedicine is still in its infancy, this branch clearly demonstrates an enormous potential. In contrast to conventional medicine, nano-medicine attempts to use sophisticated approaches to solve a health problem at molecular level, using nanodevices for diagnostic and therapies. Thus nanomedicine needs not only to apply and adopt nanotechnology concept, but will need to feedback information to nanotechnology such that the two fields can cross and develop jointly (Caruthers, et al 2007).

Raw nanomaterials	Cell simulations and cell diagnostics	Biological research
Nanoparticle coatings	Cell chips	Nanobiology
Nanocrystalline materials	Cell simulators	Nanoscience in life sciences
Nanostructured materials	DNA manipulation, sequencing, diagnostics	Drug delivery
Cyclic peptides	Genetic testing	Drug discovery
Dendrimers	DNA microarrays	Biopharmaceutics
Detoxification agents	Ultrafast DNA sequencing	Drug delivery
Fullerenes	DNA manipulation and control	Drug encapsulation
Functional drug carriers		Smart drugs
MRI scanning (nanoparticles)	Tools and diagnostics	
Nanobarcode	Bacterial detection systems	Molecular medicine
Nanoemulsions	Biochips	Genetic therapy
Nanofibers	Biomolecular imaging	Pharmacogenomics
Nanoparticles	Biosensors and biodetection	
Nanoshells	Diagnostic and defense applications	Artificial enzymes and enzyme control
Carbon nanotubes	Endoscopic robots and microscopes	Enzyme manipulation and control
Noncarbon nanotubes	Fullerene-based sensors	
Quantum dots	Imaging (cellular, etc.)	Nanotherapeutics
	Lab on a chip	Antibacterial and antiviral nanoparticles
Artificial binding sites	Monitoring	Fullerene-based pharmaceuticals
Artificial antibodies	Nanosensors	Photodynamic therapy
Artificial enzymes	Point of care diagnostics	Radiopharmaceuticals
Artificial receptors	Protein microarrays	
Molecularly imprinted polymers	Scanning probe microscopy	Synthetic biology and early nanodevices
		Dynamic nanopatform "nanosome"
Control of surfaces	Intracellular devices	Tecto-dendrimers
Artificial surfaces—adhesive	Intracellular assay	Artificial cells and liposomes
Artificial surfaces—nonadhesive	Intracellular biocomputers	Polymeric micelles and polymersomes
Artificial surfaces—regulated	Intracellular sensors/reporters	
Biocompatible surfaces	Implants inside cells	Biotechnology and biorobotics
Biofilm suppression		Biologic viral therapy
Engineered surfaces	BioMEMS	Virus-based hybrids
Pattern surfaces (contact guidance)	Implantable materials and devices	Stem cells and cloning
Thin-film coatings	Implanted bioMEMS, chips, and electrodes	Tissue engineering
	MEMS/Nanomaterials-based prosthetics	Artificial organs
Nanopores	Sensory aids (artificial retina, etc.)	Nanobiototechnology
Immunoisolation	Microarrays	Biorobotics and biobots
Molecular sieves and channels	Microcantilever-based sensors	
Nanofiltration membranes	Microfluidics	Nanorobotics
Nanopores	Microneedles	DNA-based devices and nanorobots
Separations	Medical MEMS	Diamond-based nanorobots
	MEMS surgical devices	Cell repair devices

Table 1. Taxonomy of Nanomedicine

3.1.1 Nanotechnology in Medical Diagnostic

Many of the advances and much of research in the field of Nanotechnology, particularly in the development of nanoparticles and optical methods have taken place only in the last decade. Diagnostics has a crucial role in medicine for the development of prevention and for

the treatment of disease. The aim of nanostructure-based diagnostics is their potentially higher sensitivity and selectivity in comparison to classical methods. The increased demand for sensitivity requires that a diagnostically significant interaction occur between analyte molecules and signal generating particles. Taking advantage to physical effects (as quantum confinement effects) it is possible use nanomaterials as very specific and sensitive biosensors. Developments of research in this area (Table 1), like metallic and semiconductor quantum dot structures, nanocluster, nanopowder and nanoparticles are increasing day by day. In medical application, some types of these particles could be used in vitro and overall in vivo as markers in many imaging techniques (IR or NMR) in order to increase the resolution and sensitivity and detect the disease at earlier levels.

A nanoprobe that is to function in a biological system must be watersoluble and stable with minimal interaction with the surrounding environment. Moreover the functionalization of nanoparticle surfaces with chemical recognition groups allows the identification of complementary groups on, for example, cancer cell surfaces, and the same concept can also be applied to specific drug-delivery rendering the therapy more specific and less invasive. The potential of nanodiagnostics arises from the fact that most biological molecules fall within the nanometer scale. Current diagnostic methods measure a particular property as an average of individual contribution of an ensemble of units particles, thus these methods do not give any information about a heterogeneous population. Nanodiagnosis could settle these limitations and, moreover, the entire nanotechnology-based assay are amenable to automation and the cost of diagnostic assay could become comparable or lower than the old modalities (Azzazy et al, 2006).

3.1.2 Nanotechnology in Therapies

Unfortunately early diagnosis is futile if not coupled with effective therapy. Currently, there are limited numbers of nanomedical products available (Ebbesen et al, 2006) instead, cosmetological and dermatological applications are well represented, especially with liposomal version of existing drugs (de Silva et al, 2007). It is expected that the global market of nanomedicine will expand very fast. National Institutes of Health (NIH) estimated that by the 2010, more than 50% of all biomedical advances will be in the nanotechnological sector.

Biological therapies mean the application of molecular biology in therapeutics. In this broad field are included: vaccines, gene therapy, antisense therapy, RNA interference, cell therapy and drug delivery. Some of these applications involve the use of nucleic acids and proteins,

instead, others, involve genetic manipulation. Although we are still far from the ideal "perfect bullet", today, nanotechnology has already completed several key achievements to reach this goal. For example in the application in cancer therapy several marketed compounds are currently available (Caelyx, Doxil) and many others are investigated in clinics. Also the field of infectious disease is growing and many drugs are already approved for clinical uses (Ambisome) (de Silva et al, 2007). Nanotechnology also seems to be as a promising alternative to overcome the problems of the administration of peptides and proteins used as molecular carrier, functionalizers of surface and are also used in tissue engineering.

- *Vaccination*

Nanoparticles are very promising as delivery systems for DNA vaccines. Many compound based on nanoparticles technologies are under development. Proteosomes™ (GlaxoSmithKline) serve as vaccine delivery vehicles by virtue of their nanoparticulate nature. Nanoencapsulating potent viral antigens in biodegradable polymer nanospheres for controlled release can induce the production of protective and neutralizing antibodies. This is an example of controlled release vaccine that can be applied to different types of vaccines.

- *Gene therapy*

The field of gene therapy could be defined as the transfer of selected genetic material to specific target cells of a patient in order to preventing or altering a particular disease state (Wei et al 2007). Genes and DNA are now introduced without any vector, instead a variety of nanoparticles and other nanostructures can be used for gene delivery.

- *Drug delivery*

Some drug delivery devices are implanted in the body for release of therapeutic substances. Formation of microcapsules by depositing coatings onto the particle surface will make it possible to control drug release kinetics by: (a) diffusion of the drug through a polymeric coating, (b) degradation of a biodegradable polymer coating on the drug particles, releasing the core drug material. A self-assembling cube-shaped perforated microcontainer, no larger than a dust speck, could serve as a delivery system for medications and cell therapy (Sanhai, et al 2008). Moreover thanks to their metallic nature, the location these containers can be tracked easily by MRI. These therapeutic containers can be inserted directly at the site of an injury or an illness in a very less invasive method (Allen, et al 2009). The microcontainers could someday incorporate electronic components that would allow the cubes to act as biosensors within the body or to release medication on demand

in response to a remote-controlled radio frequency signal. A nanovalve has been devised that can be opened and closed at will to trap and release molecules.

- *Cell therapy and Regenerative Nano-medicine*

The application of nanotechnology tools to the development of structures at molecular level enables the improvement of the interaction between material surfaces and biological entities. This field of nanotechnology keeps growing and has brought high expectations in regenerative medicine. Regenerative medicine is a multidisciplinary field that aims to restore, maintain or enhance tissues and hence organ functions. Regeneration of tissue can be achieved by the combination of living cells and materials, which act as scaffold to support cell proliferation and in the special case of stem cells, allow the correct differentiation (Chun and Webster, 2009). Nanomaterials used in biomedical applications include nanoparticles for molecules delivery, nanofibers for tissue scaffolds, surface modifications of implantable materials or nanodevices such biosensor (Tsai et al., 2007). The hypothetical goal of regenerative medicine is the “in vivo” regeneration or, “in vitro” generation of a complex functional organ (Engel et al., 2008).

In the next section will be explained in detail the different features of nanomaterials used in regenerative medicine with the special case of neural regenerative medicine that is the final application of this PhD thesis.

3.2 Biomaterials

Over the last decades, several approaches, coming from tissue engineering and nanotechnology, have demonstrated an unquestionable potential to regenerate damaged tissues and organs by using biomaterials capable of creating favorable microenvironments for tissue ingrowth.

An appropriate biomaterial has to exhibit good biocompatibility with extreme low inflammatory, immunogenic and cytotoxic responses. Additionally, it is desirable that the conduit presents a porous wall that mimics the size scales of fibers composing the ECM of native tissue and organs being permeable to the nutrients and permits the cell adhesion.

These characteristics have been recently introduced by innovative nanotechnology approaches, which allow the design and modification of nanoscale suitable biomaterials for the scope of cell migration, proliferation and differentiation on the injured site and subsequent tissue regeneration.

The principle aim of tissue engineering is to design a well-defined biomimetic environment that surrounds the cells and promotes specific cell interactions in order to control and direct cell behavior to reassemble into structures that resemble the original tissue.

Materials must be able to conform to the dimensions of the implantation site and maintain an appropriate shape after implantation. Additional points to consider include how to sterilize the material prior to implantation and if the material will cause an immune response. After these issues have been considered, an appropriate scaffold can be selected based on degradation rate, ability to provide controlled release and chemical physical properties.

It has long been believed that the adult mammalian central nervous system (CNS) does not regenerate after injury (Ramon et al., 2007). However, recent progress in stem cell biology has provided the hope that regeneration of the injured CNS might be achieved. CNS 'regeneration' includes the (i) regeneration of neuronal axons, (ii) replenishment of lost neural cells, and (iii) recovery of neural functions. The breakthrough of CNS regeneration will require the recapitulation of at least some aspects of the normal CNS developmental process, which is initiated by the induction of neural stem cell (NSCs) or NSC-like cells (Goodman et al., 1984, Alvarez-Buylla and Lim, 2004). This is the basic rationale behind the strategy of using NSCs for regeneration.

The biomaterials used for enhancement of nervous tissue regeneration can be divided in natural, synthetic and semi-synthetic materials.

3.2.1 Natural materials

Natural materials possess several properties that make them attractive for tissue engineering. They are obtained from natural sources, exhibiting similar properties to the tissues they are replacing and many of them contain sites for cell adhesion, allowing for cell infiltration.

Collagen and fibronectin are the main structural proteins of the ECM and continue to be the common natural materials employed. The use of collagen-based matrix has been reported in several studies (Chamberlain et al., 1998, Spilker et al., 2001). Despite their advantages, natural materials may induce foreign body response, so that they must be purified prior to implantation. Yet, residual growth factors and undefined and/or non-quantified constituents still remain (Kleinman et al., 1986) and for this reason homogeneity of product between lots can be an issue with natural materials. Moreover, natural materials are less amenable to modification compared to synthetic materials, which are cheaper and more easily characterized.

3.2.2 Synthetic materials

Synthetic materials have several advantages: they can be tailored to produce a wide range of prosthesis by reacting together different polymers to combine the properties that are unique to each, so that it is possible to obtain tubular scaffolds with different mechanical properties by varying the relative amounts of each copolymer (polymer derived from two, or more, monomeric species).

An important class of biomaterials used to develop nerve tubular guides is poly (α -hydroxy esters). These synthetic polymers are readily made into three-dimensional scaffolds that biodegrade via hydrolysis in CO₂ and H₂O resulting therefore bioresorbable. Researchers have tested several tubular nerve guides that have shown negligible inflammatory response, made of poly(glycolic acid)(PGA) (Keeley et al., 1991), poly(lactide acid)(PLA) (Cai et al., 2005), poly(lactide-co-glycolide acid)(PLGA) (Hadlock et al., 1998, Luis et al., 2008), poly(L-lactic acid)(PLLA) (Evans, 2000, Yang et al., 2005), poly(L-lactic acid)-caprolactone (PLLA-PCL) (Meek et al., 1997) and poly(DL-lactide-co-glycolide) and poly(ϵ -caprolactone) (PCL/PLGA) (Panseri et al., 2008). Hydrogels, insoluble hydrophilic polymers are a very promising class of synthetic materials for nervous regeneration. The high water content and tissue-like mechanical properties of hydrogels make them highly attractive scaffolds for implantation in empty tubular nerve prosthesis or to directly inject them in the lesion site to enhance cell attachment and growth.

Self-assembling peptides belong to the hydrogel class of biomaterials. They consist in a specific amino acid sequence that self-assemble under physiological conditions forming a nanoscaffold with very thin fibers (~10 nm in diameter). In the last few decades, they have been studied as biomaterials not only useful for specific 3-Dimensional (3D) tissue cell cultures but also for tissue repair and regenerative therapies. These peptide scaffolds can be commercially and custom-tailor synthesized, modified readily at the single amino acid level at will inexpensively and quickly.

Furthermore, these designer self-assembling peptide scaffolds have recently become powerful tools for regenerative medicine to repair infarctuated myocardia (Davis et al., 2005), to stop bleeding in seconds (Ellis-Behnke et al., 2006) and to repair nervous tissue (Ellis-Behnke et al., 2006), as well as being useful medical devices for slow drug release (Riehemann et al., 2009).

Ellis-Behnke and colleagues showed that the self-assembling peptide RADA16-I is a promising scaffold for neural regeneration in optic nerve lesions in hamster pups. Animals were treated by injection of RADA16-I into their surgical wounds. The authors showed that only in

animals treated with multiple injections of the self-assembling scaffold the brain tissue appears to have healed, while in untreated animals functional damage was still evident after weeks (Ellis-Behnke et al., 2006). The greatest disadvantage of synthetic materials, however, is the lack of cell-recognition signals and presenting therefore few cellular interactions. Toward this end, efforts are being made to incorporate cell-adhesion peptide motifs into synthetic biomaterials.

3.2.3 Semi-synthetic materials

The concept of combining synthetic materials with cell-recognition sites of naturally derived materials is very attractive. These new and versatile hybrid biomaterials could possess the favorable properties of synthetic materials, including widely varying mechanical and biodegradable properties, reproducible large-scale production, and good processability, as well as similar biological activity of natural materials.

Many researchers have been focusing on the development of these semi-synthetic biomaterials that due to their characteristics hold clinical promise in serving as implants to promote wound healing and tissue regeneration. Placed at the site of a defect, such materials should actively and temporarily participate in the regeneration process by providing a scaffold on which cell-triggered remodeling could occur (Elbert and Hubbell, 2001, Marchesi et al., 2007).

Lately Koh and colleagues have enhanced the neurite outgrowth using nanostructured scaffolds coupled with lamin (Koh et al., 2008), a well known component of the ECM that is continuously synthesized after nerve injury and it plays a crucial role in cell migration, differentiation and axonal growth. Lamin was coupled into PLLA nanofibers using three different methods: covalent binding using water-soluble carbodiimide and N-hydroxysuccinimide as the coupling reagents, physical adsorption, and physical blending of lamin together with PLLA solution for electrospinning procedure. The last method, blended electrospinning, demonstrated to be the more efficient technique to introduce lamin on the surface and in the interior of the nanofibers.

Self-assembling peptides provide the opportunity to incorporate a number of different functional motifs and their combinations to study cell behavior in a well-defined ECM-analogue microenvironment, not only without any chemical cross-link reactions but also with fully bioresorbable scaffolds. Using peptide altering the amino acid sequences containing RADA as a support material (RADA16-I), Gelain and colleagues conjugated a range of bioactive peptides including fibronectin, collagen VI, laminin, as well as two bone marrow homing peptides BMHP1 and BMHP2 (Gelain et al., 2006). Adult mouse NSCs were cultured on these surfaces and assayed for adhesion level, viability

and differentiation. Interestingly, the BMHPs supported greater adhesion than all other peptides.

The BMHPs seemed to induce differentiation nonspecifically as there were approximately equal proportions of neurons, glia, and undifferentiated cells at seven days in culture. The gene expression profiling array experiments showed selective gene expression, possibly involved in NSC adhesion and differentiation. These results show very promising approaches for the employment of these functionalized hydrogels in nervous regeneration.

3.2.4 Design of Nanostructures

In the last few decades, most of the strategies used in nervous tissue engineering made use of rigid channel guides that eventually caused cell loss or neuropathy due to unphysiological local stress exerted over the nervous tissue during patient's movement. For these reasons, the future of graft technology depends on optimization of the scaffold geometry, mechanical properties and cross-sectional area, in order to increase the number and efficacy of ascending and descending axons. The development of nanofibers has greatly enhanced the scope of fabricating scaffolds that can potentially meet this challenge. Polymeric nanofiber matrices are among the most promising ECM-mimetic biomaterials because their physical nanostructures are similar to that of fibrous proteins in native ECM.

Currently, there are three major methods to fabricate polymeric nanofibers: electrospinning, self-assembly and phase separation.

- *Electrospinning*

Electrospinning represents an attractive technique for the processing of polymeric biomaterials into nanofibers. This technique offers the opportunity for control over thickness and composition of the nanofibers along with porosity of the nanofiber meshes, using a relatively simple experimental setup.

Although polymer melt can also be electrospun, the resultant fiber is generally above 1 μm in diameter, while for electrospun polymer solution, average fiber diameter of 19 nm has been obtained (Davis et al., 2005).

The material to be electrospun, which can be natural, synthetic or semi-synthetic, is first dissolved in a suitable solvent to obtain a viscous solution. The solution is passed through a spinneret and a high voltage supply is used to charge the solution. At a critical voltage, typically above 200 V/m, the repulsive forces of the charged solution particles result in a jet of solution erupting from the tip of the spinneret (Fig.1).

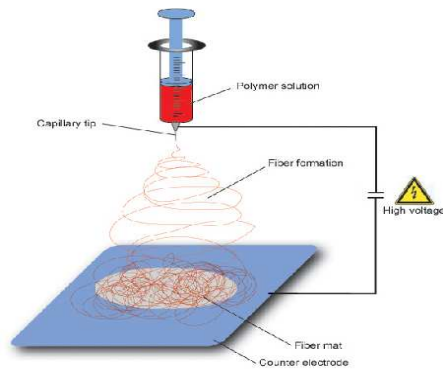


Fig1. Schematic illustration of electrospinning apparatus.

Conventional electrospinning produces nanofibers that are randomly oriented; instead, the use of an electric field on the charged polymer solution makes it possible to control its trajectory, enabling the production of oriented nanofibers that can be useful in the designing of scaffolds for tissue engineering.

Among the synthetic polymers explored for the fabrication of nanofibers, poly(glycolic acid)(PGA) (Keeley et al., 1991), poly(lactic acid)(PLA) (Cai et al., 2005), poly(lactic-co-glycolic acid)(PLGA) (Hadlock et al., 1998) and poly(L-lactic acid)(PLLA) (Evans, 2000) have been well studied.

Researchers have tested several tubular nerve guides, that have shown negligible inflammatory response, made of a blend of poly(L-lactic acid)-caprolactone (PLLA-PCL) (Meek et al., 1997) and poly(L-lactic acid)-poly(ϵ -caprolactone) (Panseri et al., 2008) in order to ameliorate the stability and the mechanical properties of the scaffold.

- *Self-assembly*

Molecular self-assembly has recently emerged as a new approach in engineering artificial scaffolding materials that emulate natural ECM both structurally and functionally. Unlike electrospinning, this technology not only incorporates specific biological components of the ECM, but also mimics the process of ECM assembly from the bottom up (Dunetz et al., 2005). Specific polypeptide sequences have the capacity to self-assemble into various structures, ranging from assembly of β -sheets via hydrogen bonding to cylindrical micelles via hydrophobic interactions.

Zhang and colleagues developed a scaffolding material that self-assembled from amphiphilic oligopeptides, which consist of alternating

positively (lysine or arginine) and negatively (aspartate or glutamate) charged residues separated by hydrophobic residues (alanine or leucine). This scaffold material, RADA16, was used to test neuronal growth using rat hippocampal neurons and the growth of these cells in culture accompanied by functional synapse formation was observed (Zhang et al., 1995).

To improve these self-assembling biomaterials for a specific cell/tissue response, it is possible to functionalize them by including in the core amino acidic sequence specific motifs that do not impair the capacity of the material to self-assemble. Using the RADA16-I self-assembling peptide as a support material, Gelain and colleagues conjugated a range of bioactive peptides including fibronectin, collagen VI, laminin, as well as two bone marrow homing peptides BMHP1 and BMHP2 (Gelain et al., 2006). Adult mouse NSCs were cultured on these surfaces and assayed for adhesion level, viability, and differentiation. Interestingly, the BMHPs supported greater cell adhesion than all other peptides. The BMHPs seemed to induce differentiation nonspecifically as there were approximately equal proportions of neurons, glia, and undifferentiated cells at seven days in culture. The gene expression profiling array experiments showed selective gene expression, possibly involved in NSC adhesion and differentiation.

- *Phase separation*

The motivation to mimic the 3D structure of collagen, present in the natural ECM, led to develop a new technique, called thermally induced liquid - liquid phase separation, for the formation of nanofibrous foam materials (Arrondo and Goni, 1999, Aggeli et al., 2001). The nanofibrous foams produced using the phase separation technique are very similar in size to the natural collagen present in the ECM; 50 to 500 nm. For this reason, this method is frequently used to prepare 3D tissue engineering scaffolds.

Phase separation of a polymer solution can produce a polymer-rich domain and a solvent-rich domain, of which the morphology can be fixed by quenching under low temperature. Removal of the solvent through freeze-drying or extraction can produce porous polymer scaffolds. Of much interest is that this freeze-drying method might be adjusted to produce pores of various orientations in the same cylindrical specimen. Pores in the central region of the prosthesis could be oriented axially whereas peripheral pores could be oriented radially. This may provide the opportunity to selectively seed peripheral pores with certain cell types, which could support regeneration of peripheral tissue, such as the epineurium, while allowing the central region to remain orientated to accommodate elongation of nerve fibers.

Phase separation can be induced by changing the temperature or by adding nonsolvent to the polymer solution, thus called thermal induced or non-solvent-induced phase separation, respectively. Polymer scaffolds obtained by the phase separation method usually have a spongelike porous morphology with microscale spherical pores (Hua et al., 2002). However, if the conditions such as solvent, polymer concentration, gelation temperature and gelation time are precisely controlled, micro- or nanoscale polymer fibers can be obtained.

3.2.5 Nanostructured materials design for nervous regeneration

Tissue engineering scaffolds should be analogous to native ECM in terms of both chemical composition and physical structure. For the achievement of this goal, functionalized nanofibers are continuously developed in order to induce the best tissue response and to enhance regeneration.

In native tissues cells are often regularly oriented and this cell orientation is of crucial importance for tissue function. This is particularly true for neural tissue, where neuronal/axonal growth have a precise directionality. When seeking to regenerate the peripheral nervous tissue it is very important to enhance the neurite growth direction in order to connect the two lesioned nerve stumps. The scope of the application of aligned polymer nanofiber in tissue engineering is exactly to control cell orientation.

Aligned electrospun PCL fibers were tested with human Schwann cells and it was shown to reproduce the formation of bands of Büngner. Schwann cells were observed to elongate and align along the axes of the electrospun fibers and to enhance the rate and extent of neurite elongation (Chew et al., 2008). Another aligned electrospun PLLA nano/micro fibrous materials investigated the suitability of the scaffold for NSC culture in terms of their fiber alignment and dimension. The results suggest that the aligned nanofibers help to improve neurite outgrowth when they are in a highly oriented status, whereas the fiber diameter do not show any significant effect on cell orientation. On the contrary, the NSC differentiation rate is higher for the nanofibers scaffold than that of microfibers, but it was independent of the fiber alignment (Yang et al., 2005).

For tissue engineering scaffold applications, different fiber diameters are required depending on the tissue. The typical diameter of proteins in native ECM range from several tens to 300 nm, therefore nanofibers are usually desired. In electrospinning, self-assembling and phase separation the diameter of the nanofiber should be controlled by adjusting parameters including polymer concentration, amino acid

sequence, flow rate of the polymer solution, solvent conductivity and temperature.

A new electrospinning technology to prepare polymer nanofibers with a core-shell structure has been introduced. This technique uses a specifically designed plunger with a coaxial opening structure, which contains a core opening and a surrounding annular opening. Different solutions can be introduced into the core opening and the annular opening and electrospun into a core-shell-structured nanofiber. The most likely application of this technique is to embed drugs, growth factors or genes into the core of the biodegradable polymer nanofibers, producing polymer nanofibers able to release drugs. In addition to drug carriers, the core-shell strategy can be used in another way. By setting synthetic polymer as the core material and natural polymer such as collagen as the shell material, nanofibers with strong mechanical strength and good biocompatible surface can be obtained. This strategy may solve the problem of poor biocompatibility of synthetic polymer nanofibers.

Surface modification of biomaterials, with the intent to improve not only biocompatibility but also target cell/tissue response has been extensively studied in order to recreate the native nervous structure and to do it in the shortest time possible. An increasingly employed approach for emulating the ECM involves identifying bioactive motifs present in these molecules and grafting synthetic analogues of these signals onto a material. For example, cells engage with ECM ligands via receptors such as integrins. They are known to bind to several common polypeptide motifs like arginine-glycine-aspartic acid (RGD). The possibility to include these motifs in the biomaterials structure can promote cell interactions and enhance nervous regeneration.

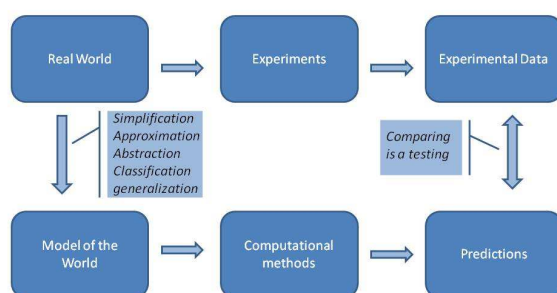
An important feature for promising biomaterials is its porosity. Regeneration through microporous grafts is not only superior to regeneration through either synthetic nonporous or macroporous grafts but even nearly as good as regeneration through autografts (Vleggeert-Lankamp et al., 2007, Vleggeert-Lankamp et al., 2008). Pores positively influence the size of tissue bridge by allowing inward diffusion of growth factors and ECM proteins, and outward diffusion of waste products.

A further modification of nanomaterials is to obtain a controlled diameter and orientation pore. Collagen-based matrix with axially oriented pores from about 20 to 60 μm of range was obtained by phase separation (Madaghiele et al., 2008). The use of a porous oriented scaffold facilitates peripheral nerve regeneration. In addition, the oriented scaffold may also be used as a delivery vehicle for exogenous cells and growth factors in case where the regenerative response induced by the scaffold alone is insufficient.

Hydrogels are highly hydrated and very porous. In particular the use of self-assembling peptides can be very useful in nervous regeneration because it is possible of being mixed with cells and/or growth factors with the amino acid sequence in liquid phase. After self-assembling, the cells and the growth factors are incorporated directly into the nanomaterials, in which cells can adhere and grow through the pores and the growth factors can be released with a specific drug delivery kinetic (Nagai et al., 2006).

3.3 Structural characterization of Self –Assembling Peptides

As just elucidated in the paragraph 2.4 the self-assembling mechanism is becoming increasingly important in the fabrication of novel supramolecular structures. Peptides represent the most favourable building blocks to design and synthesize novel nanostructures with a wide range of application and different physical and chemical features. The study of self-organization properties of peptides is crucial; understanding the determinants that underlie peptide self-assembling is a fundamental step to develop new ones. This requires the combined effort of experimental and theoretical approaches (as shown in the scheme 1). Combining knowledge form both fields will improve our understanding of the firsts principles that govern the organization of the nanostructures formed by peptides system, and then it will be possible applied the same rules to develop new target applications.

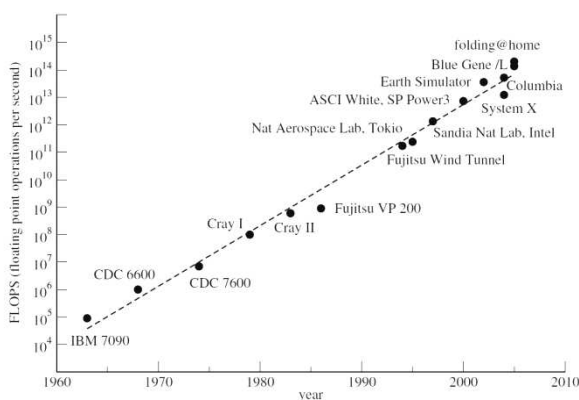


Scheme 1. Combination of theoretical and experimental approaches

3.3.1 Computational characterization

The high degree of complexity of the self-assembling process and the difficulties in obtaining X-ray or NMR structures of the aggregates, have severely hampered the experimental characterization of the

process. Theoretical and computational methods hold this important role, in the development of a framework for understanding the mechanism leading to the ordered aggregates formation and in the design of new sequences with selected properties for nanobiotechnological applications. The development of new algorithms and theories, combined with the increasing of computer power (scheme 2) (Riehemann et al., 2009), has rendered this way of investigation more possible than in the past and consistent at biomolecular resolution. Computational methodologies are, at present, the only possibility for atomic-resolution investigation of many processes involved in nanotechnologies, despite the recent progresses in the development of experimental analysis techniques.



Scheme 2. Growth of computational power

- *All-atoms Simulations*

The great growth of computational power over the past two decades has led to the development of large-scale simulation techniques whose aim is to directly reproduce or simulate processes on a molecular level. Molecular dynamics (MD) simulations, have proven to be invaluable in elucidating the structural, mechanical and chemical properties of different kinds of materials (Karplus, 2003). For example, MD simulations have been used to study the liquid state, the bulk solid, glasses, conductive materials, polymers, and protein dynamics. Indeed, MD simulations could represent the future of theoretical techniques in the broad fields of nanotechnology.

Simulation of biomolecules represents one of the hardest problems of computational scientists. When contemplating an MD simulation of biomolecules, one would ideally like to carry out a quantum mechanical calculation, based for example on the density functional theory approach (DFT). Some methods as the Fast-Fourier transform based Car-Parrinello or the real-space multigrid methods are tested, with truly

predictive powers (Colombo et al., 2007). However, they require substantial computational investments.

Such simulations are still impractical for many biological systems, which typically contain many thousands of atoms with relevant timescales.

In classical MD simulations, the trajectories of interacting atoms are calculated through a simplification of Newton's laws. Forces generated by atom-atom interactions, are usually given in terms of an empirical potential. The step of parameterization of potential energy is the crucial step of all MD simulations. Parameters for the potential are usually obtained by fitting to either ab-initio calculations or experimental data.

$$E = \sum_{\text{bonds}} \frac{a_i}{2} (l_i - l_{i0})^2 + \sum_{\text{angles}} \frac{b_i}{2} (\theta_i - \theta_{i0})^2 + \sum_{\text{torsions}} \frac{V_n}{2} (1 + \cos(n\omega - \gamma))$$

$$+ \frac{1}{2} \sum_{i=1}^N \sum_{j \neq i}^N 4\epsilon_{ij} \left[\left(\frac{\sigma_{ij}}{r_{ij}} \right)^{12} - \left(\frac{\sigma_{ij}}{r_{ij}} \right)^6 \right] + \frac{1}{2} \sum_{i=1}^N \sum_{j \neq i}^N \frac{q_i q_j}{r_{ij}}, \quad 1.$$

The first term of expression 1 is a harmonic potential between bonded atoms that gives the contribution to the energy. Similarly, the second term is a harmonic potential in the valence angles of the molecules. The third term is a torsional potential describing the periodic variation in energy due to bond rotations.

The last two terms represent nonbonded interactions. The fourth contribution is a Lennard-Jones potential representing the van der Waals interactions, and the last term is the Coulomb electrostatic potential. Note that the first four terms deal with mainly short-ranged interactions. Long-range forces were mainly ignored in macromolecular simulations, being truncated with the use of artificial, non bonded cutoffs. From knowledge of the force on each atom, it is possible to determine the acceleration of each atom in the system. Integration of the equations of motion then yields a trajectory that describes the positions, velocities and accelerations of the particles as they vary with time. From this trajectory, the average values of properties can be determined. The method is deterministic; once the positions and velocities of each atom are known, the state of the system can be predicted at any time in the future or the past. Therefore, to calculate a trajectory, only the initial positions of the atoms, an initial distribution of velocities and the acceleration are due. The acceleration is determined by the gradient of the potential energy function. The initial positions can be obtained from experimental structures, such as the x-ray crystal structure of the protein or the solution structure determined by NMR spectroscopy. The initial distribution of velocities are usually determined from a random

distribution with the magnitudes conforming to the required temperature and corrected so there is no overall momentum. The velocities, v_i , are often chosen randomly from a Maxwell-Boltzmann or Gaussian distribution at a given temperature, which gives the probability that an atom i has a velocity v_x in the x direction at a temperature T . There is no analytical solution to the equations of motion due to its complicated nature, however many numerical algorithms have been developed to integrate the equations of motion and solve it in a numerical way.

The Verlet algorithm is one of the most used algorithm to integrate the equation of motion. The basic idea is to write second-order Taylor expansion for the position $r(t)$, one forward and one backward in time. Calling v the velocities, a the accelerations, one has:

$$r(t + \Delta t) = r(t) + v(t)\Delta t + \frac{1}{2}a(t)\Delta^2 \quad 2.$$

$$r(t - \Delta t) = r(t) + v(t)\Delta t + \frac{1}{2}a(t)\Delta^2 \quad 3.$$

Summing these two equations (2, 3), one obtains:

$$r(t + \Delta t) = r(t) + v(t + \frac{1}{2}\Delta t)\Delta t \quad 4.$$

The Verlet algorithm uses positions and accelerations at time t and the positions from time $t-dt$ to calculate new positions at time $t+dt$. The Verlet algorithm uses no explicit velocities. The advantages of the Verlet algorithm are, *i*) it is straightforward, and *ii*) the storage requirements are modest. The disadvantage is that the algorithm has a moderate precision.

To solve the precision problems of Verlet algorithm, Leap-Frog method was created as a modified version of Verlet. In this algorithm, the velocities are first calculated at time $t+1/2dt$; these are used to calculate the positions, r , at time $t+dt$. In this way, the velocities *leap* over the positions, and then the positions *leap* over the velocities. The advantage of this algorithm is that the velocities are explicitly calculated, however, the disadvantage is that they are not calculated at the same time as the positions. The velocities at time t can be approximated by the relationship:

$$v(t) = \frac{1}{2} \left[v \left(t - \frac{1}{2}\Delta t \right) + v \left(t + \frac{1}{2}\Delta t \right) \right] \quad 5.$$

Another example of algorithm could be the Beeman's one that produce the same positions of the Verlet algorithm but the velocities are more accurate introducing also the error $O(\Delta t^3)$.

The equation to compute the positions at the time $(t + \Delta t)$ becomes:

$$r(t + \Delta t) = r(t) + v(t)\Delta t + \frac{2}{3}a(t)\Delta t^2 - \frac{1}{6}a(t - \Delta t)\Delta t + O(\Delta t^3) \quad 6.$$

And the equation to obtain the velocities is:

$$v(t + \Delta t) = v(t) + \frac{1}{3}a(t + \Delta t)\Delta t + \frac{5}{6}a(t)\Delta t - \frac{1}{6}a(t - \Delta t)\Delta t \quad 7.$$

With MD simulation important information can be gained using different strategies. MD simulation was used in the past decade to describe some protein stability in different solvent, moreover was a potent tool to investigate about the conformational transition from the soluble to aggregating β -sheet-rich conformation of peptides. The interest in this last field is motivated by the direct application to the neurodegenerative diseases in which amyloid proteins are involved.

Self-assembly process is still an extreme challenge for all-atom models because simulations must handle many chains and find ways to follow the dynamics during some of the crucial steps. By the way, with MD is it possible to investigate about effects on the stability of a certain assembly of different hypothetical arrangements (Hwang et al., 2004) or the effects of sequence mutation on a certain supramolecular conformation. This approach was introduced by Nussinov and coworker to investigate about several peptides comes from Syrian Hamster prion, and others peptides from the Alzheimer's $A\beta$ that demonstrated that the final structure of the fibril depends on the protein sequence (Colombo et al., 2007).

For the self assembling forming fibers, one of the crucial mile stone is the work of Hwang et al (Hwang et al., 2004). in which self assembling synthetic peptides were used as a model system for amyloid fibrillogenesis. Hwang explored the kinetic of aggregation formation starting from the dimerization of two single molecules of $A\beta_7$ (KLVFFAE), $A\beta_{7g}$ (KLVFFAG), K_I (KTVIIE), K_L (KTVLIE), and KFE8 (FKFEFKFE). In this work, for the first time, MD simulations were used to describe the process of β -sheet formation and the role of kinetic trapping in the process of peptide folding.

The essential driving forces behind the growth and development of the field of biomolecular modeling were principally two. The first one in the increasing in computing power than grew with a factor of 10 about every 5 years over the past few decades (as is shown in the Scheme 2). The second driving force behind biomolecular modeling is the advancement of modeling techniques. For example, efficient algorithms to compute long-range electrostatic forces have become available (Tirion, 1996). Methods have been developed to extend and enhance

sampling and biomolecular force fields have been refined. By the way, it still remains mandatory to formulate simple and approximate models that contain just the necessary degrees of freedom to adequately represent the phenomenon of interest. The combination of coarse-grained and atomic resolution approach might hold great promise in the simulation of biomolecular processes.

- *Coarse-grained simulations*

Coarse-grained model for proteins and peptides have recently renewed interest. Although these techniques still cannot be considered as predictive as all-atom simulations, advances have recently been achieved, concerning the use of more rigorous parameterization techniques and novel algorithm for sampling configurational space.

The complexity, time and length scale of the self-assembling process implies that coarse-grained models have to be used. In this kind of methodology, the finest resolution atomic details are neglected, and only relevant degrees of freedom of the peptide molecules are taken in account. Thus, the idea of using simplified descriptions through the integration of a large number of degree of freedom into a few arises spontaneously. At this stage a large variety of different simplified descriptions and rigorous methodologies for the parameterization are currently available. However the step of parameterization could represent the hardest starting-point of a coarse-grained model, because more specific interactions must be included in fewer parameters and functional forms (Tirion, 1996). Different model represent a compromise between accuracy and transferability.

In the elastic network models (ENMs), for example, the system is represented by a network of beads connected by elastic spring. This method is very simple and included also the topology of the system; in this way it is able to reproduce the correct pattern of the principal modes. ENMs are methods that can be applied to the investigation of certain protein behaviours: decompose proteins in structural domains (Zhang et al., 2003) or identify signature of secondary structure (Micheletti et al., 2004). Recent applications include fitting atomic structure into electron density map (Hinsen et al., 2005) or a reconstruction of molecular aggregates (Chacon et al., 2003). ENMs are used with normal mode analysis (NMA) for the analysis of the principal mode of very different systems.

Another method that includes the representation of one-bead aminoacid is the Gō-like model. In this method the bead are connected trough simple attractive or repulsive non-bonded interactions (Y. et al., 1978). In this way it is possible to describe many thermodynamic processes. In recent works, this method was updated because it failed in described intermediate metastable folding states. In the study of Jang and co-

workers Gō-model was used to study the folding and the stability of β -sheet complexes in combination with and all atom description, and shown to elucidate important sequence-dependent features(Y. et al., 1978).

Moreover the Monte Carlo technique provides a flexible framework to use a coarse-grained with dynamical procedure, moving the particles according to potential energy gradients without explicitly integrating equations of motion (explained in all-atoms simulation paragraph). This technique involve sequential moves of individual particles and so neglect the correlated motion of particles on timescales less that the fundamental discrete time step Δt . However, for many systems, this kind of neglecting leads to unphysical relaxation, particularly for long times.

To solve this problem, such algorithms indentify collections of particles to be moved in concert by recursively linking particles according to a set of criteria, such as the pairwise energy or the proximity of neighboring particles. The ‘virtual-move’ Monte Carlo is one of these algorithms. It is a dynamic procedure able to identify, on the basis of potential energy gradient explored in a timescale Δt , the extent to which motion of one particle is correlated with its neighbors. With this kind of correlation this motion is effected with a frequency designed to approximate physical dynamics. The scheme of algorithm is the following:

- i) Start in μ microstate.
- ii) Define a pseudocluster C , choosing a ‘seed’ the particle i .
- iii) Link i to a neighbor j with probability $p_{ij}(\mu \rightarrow \nu)$, that depends on the virtual move of i that define a new microstate ν .
- iv) Particles linked to the members of pseudocluster join the pseudocluster.

The acceptance criterion of move ($\mu \rightarrow \nu$) has the probability:

$$W_{acc}^{\mu \rightarrow \nu} = \Theta(n_c - n_C) \mathcal{D}(C) \min \left\{ 1, e^{-\beta(E_\nu - E_\mu)} \times \frac{\prod_{v \rightarrow \mu} q_{ij}(v \rightarrow \mu)}{\prod_{\mu \rightarrow \nu} q_{ij}(\mu \rightarrow \nu)} \prod_{(i,j) \in C} \frac{p_{ij}(v \rightarrow \mu)}{p_{ij}(\mu \rightarrow \nu)} \right\}$$

$\mathcal{D}(C) \leq 1$: Factor that is introduced to modulate the diffusivity of pseudocluster according to the size.

E_α is the energy of the system in the microstate α .

$q_{ij} \equiv 1 - p_{ij}$ is the probability of not linking particle i and j .

R denotes a particular realization of formed and failed links.

n_c size of pseudocluster.

n_c specified cutoff.

The probability to link particles i and particle j is:

$$p_{ij}(\mu \rightarrow \nu) = \Theta(n_c - n_C) \times I_{ij}^{(\mu)} \max(0, 1 - e^{\beta \varepsilon(i,j) - \beta \varepsilon(i',j)})$$

$\varepsilon(i, j)$ is the pairwise energy of the bond ij in the microstate μ .

$\varepsilon(i', j)$ is the bond energy of the bond ij following the virtual move of i .

$I_{ij}^{(\mu)}$ is 1 if i and j interact in the microstate μ 1 otherwise is 0.

This algorithm is recently applied to self-assembling process, and it could be a good tool to extend also to self-assembling peptides.

3.3.2 Experimental characterization

- Spectroscopic techniques

Since the early X-ray studies of Kendrew that revealed the folding of a protein chain, there were a hard work to relate the amino acid sequence of a protein to its three-dimensional structure. Despite great effort, this goal remains elusive. However, the need to predict the conformation of proteins is becoming ever more acute as the flood of new sequences arising from the human genome project provides an array of possible new targets for biomedical research.

Experimental verification of folding motif may be gained by measurements of protein secondary structural elements of which the motif is composed. In many cases the fraction of peptide bonds in α -helical, β -pleated sheet, and unfolded conformations may be estimated from highly sensitive optical measurements, such as CD (circular dichroism), IR (infrared) and Raman spectroscopies. In addition, spectroscopic measurements of secondary structures are a valuable tool for assessing protein aggregation and stability. In fact, in the recent years these spectroscopic techniques were used to investigate about the amyloid proteins behavior with great results (Apetri et al., 2006, Nevin et al., 2008). For these reason it was reasonable to apply these techniques to the investigation of secondary structure of self-assembling peptides forming fibers.

The secondary structure of a protein is determined by the set of dihedral angles (ϕ, ψ) , which define the spatial orientation of the peptide backbone, and the presence of specific hydrogen bonds.

The principal geometry for the α -helix is $\phi \sim 260^\circ$ and $\psi \sim 245^\circ$ with hydrogen bonds from the NH of the fifth residue in the chain to the C=O group on the first residue, or between residues i and $(i + 4)$. It forms a compact, rodlike structure with 3.6 amino acids (1.5 Å) per repeating unit and a radius, excluding side chains, of 2.3 Å.

The dihedral angles of the β -sheet are $\phi \sim -130^\circ$ and $\psi \sim 120^\circ$ (as it shown in Fig.2), forming an extended structure with some right-handed twist. Hydrogen bonds between protein chains oriented either in a parallel or in an antiparallel fashion, stabilize β -sheets in proteins and protein complexes. Turns allow a protein to fold back on itself and are stabilized by a hydrogen bond that holds the ends together. They are

classified according to the number of residues involved in the hydrogen-bonded structure.

The peptide backbone in a β -turn forms a rough plane that contains the intramolecular hydrogen bond. However, the amide bond between the ($i+1$) and the ($i+2$) residues is perpendicular to this plane and must hydrogen-bond elsewhere. In addition, the side chains of turns project outward. Thus, β -turns are often found on the surface of proteins where hydrogen bonding with the solvent is favorable. Because of their surface location, turns play major roles in molecular recognition. Unordered or random structure is generally defined as a conformation that is not helix, sheet, or turn.

Circular dichroism is observed when molecules absorb left and right circularly polarized light to different extents (view also appendix A). The amide chromophore of the peptide bond in proteins dominates their CD spectra below 250 nm. In an α -helical protein, a negative band near 222 nm is observed due to the strong hydrogen-bonding environment of this conformation. This transition is relatively independent of the length of the helix. A second transition at 190 nm is split into a negative band near 208 nm and a positive band near 192 nm. Both bands are reduced in intensity in short helices. The CD spectra of β -sheets display a negative band near 216 nm, a positive band between 195 and 200 nm, and a negative band near 175 nm. The position and magnitude of these bands is variable, resulting in less accurate predictions for β -structure than for α -helices by CD. However, this spectroscopic technique was used in many works of Zhang and coworkers (Zhang, 2003, Yokoi et al., 2005) to investigate about the secondary structures of self-assembling peptides forming fibers in different surround conditions, revealing CD spectroscopy a good tool to develop the nanostructure of these peptides.

Raman scattering spectrum provides essentially the same type of information as the *infrared (IR) absorption* spectrum, namely, the energies of molecular normal modes of vibration. However, the two methods differ fundamentally in mechanism and selection rules, and each has specific advantages and disadvantages for biological applications. Instrumentation is typically more complex for Raman (light scattering) than for IR (light absorption)(view also Appendix); also Raman data collections are generally slower and more tedious, often leading to signal-to-noise levels inferior to those obtainable by modern Fourier-transform IR (FTIR) methods. Additionally, it is problematic to compare quantitatively the scattering intensities of Raman bands, whereas IR absorption intensities are governed by Beer's Law. Conversely, water is a notoriously strong IR-absorbing medium, and aqueous systems cannot be investigated with ease by IR methods. In contrast, water (H₂O or D₂O) interferes only feebly with Raman

spectra of aqueous solutions and hydrated solids. Indeed, samples of virtually any hydration level can generally be investigated more favorably by Raman than by IR spectroscopy.

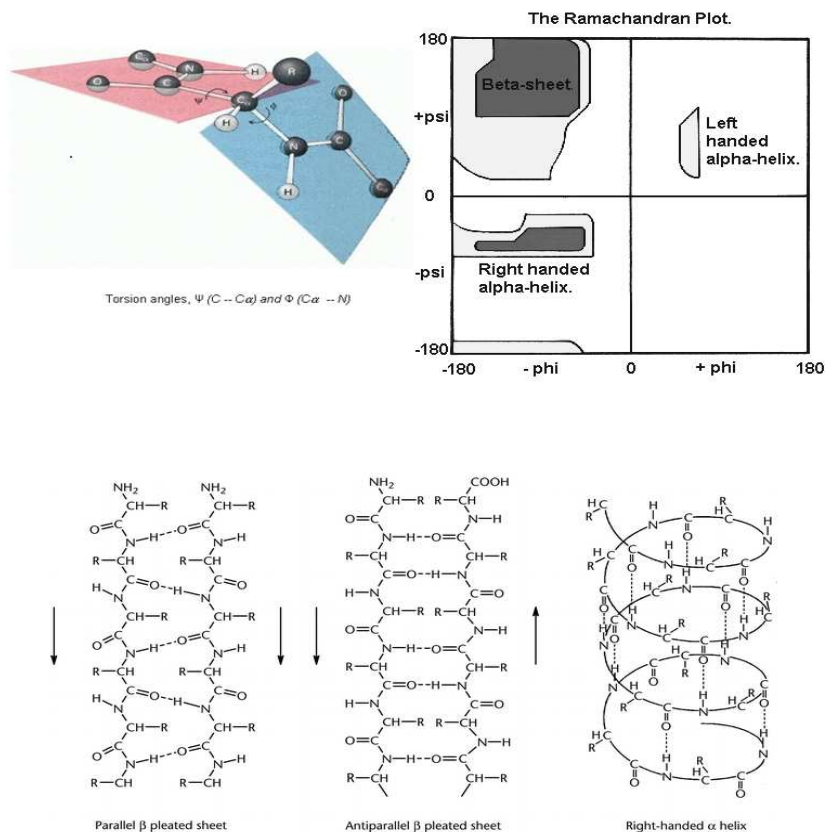


Fig2. Schemes of α -helix and β -sheet. A) represent a classic Ramachandran plot in which are shown areas for the different secondary structures for proteins. B) typical h-bonds that stabilized proteins secondary structure

However, the two techniques provide complementary information. IR results from the absorption of energy by vibrating chemical bonds (primarily stretching and bending motions). Raman scattering results from the same types of transitions, but the selection rules are somewhat different so that weak bands in the IR may be strong in the Raman and vice versa. Raman spectra are reported as the difference between the incident and scattered radiation frequencies. These frequencies depend on the types of bonds and their modes of vibration. Characteristic groups of atoms give rise to vibrational bands near the same frequency regardless of the molecule in which they are found. The precise wavenumbers of bands within this range depend on interand

intramolecular effects, including peptide-bond angles and hydrogen-bonding patterns. Thus, vibrational spectra can be used to estimate the secondary structure of proteins by inspection of the frequencies at which the amide bonds absorb infrared radiation. The application of infrared and Raman spectroscopies to protein secondary structure (Torreggiani et al., 2003) has undergone a renaissance with the development of Fourier transform spectrometers and improved computers. Nine normal modes are allowed for the amide band of proteins. These are called A, B, and I-VII in order of decreasing frequency (Thomas, 1999). The amide bands I (80% C=O stretch, near 1650 cm⁻¹), II (60% N-H bend and 40% C-N stretch, near 1550 cm⁻¹), and III (40% C-N stretch, 30% N-H bend, near 1300 cm⁻¹) are generally employed to study protein structure. The amide I and III bands have appreciable Raman intensities with visible light excitation. In practice, the amide I band in FT-IR and the amide I and III bands in Raman are primarily used to assign secondary structures to proteins (Carrier and Pezolet, 1984).

Identification of particular frequencies with secondary structures has been made by reference to spectra of homo-polypeptides and proteins with primarily α -helical or β -sheet structures, theoretical calculations (normal mode analysis), synthetic peptides, and proteins with known three-dimensional structures. Raman also provides information on aromatic residues in the region below about 1620 cm⁻¹ (Fig.2).

Accordingly, the Raman spectrum of a protein is largely dominated by bands associated with the peptide main chain, aromatic side chains, and sulfur-containing side chains. Instead, IR absorption spectra of proteins and nucleic acids, more so than Raman spectra, are complicated by overlapping bands from many types of residues. Other notable advantages of Raman spectroscopy are (a) applicability to samples in different physical states (solutions, suspensions, precipitates, gels, films, fibers, single crystals, amorphous solids, etc) and to large macromolecular assemblies, (b) a spectroscopic timescale that is short in comparison with either either biomolecular structure transformations or protium/deuterium exchanges, (c) nondestructiveness of data collection protocols, (d) minimal requirements of sample mass ($\gg 1$ mg) and volume ($\gg 1$ μ L), (e) no requirement for chemical labels or probes, and (f) existence of a large database of Raman spectra of model compounds for which reliable band assignments, normal mode analyses, and spectra-structure correlations have been made. The correlations are generally transferable to proteins and nucleic acids and facilitate interpretation of spectra.

The most important vibrational mode used for characterized proteins and peptides in both Raman and FT-IR is the amide I (Susi and Byler, 1986). Amide group vibrations of the backbone receive the most

attention in protein spectroscopy because they are native to all proteins and report on secondary conformation and solvation. These include amide I (primarily CO stretch), amide II (CN stretch and NH in-plane bend), amide III (CN stretch, NH bend, and CO in-plane bend), and amide A (NH stretch). The amide I band (1600–1700 cm⁻¹) is by far the most studied because its line shape is sensitive to the type and amount of secondary structures and is not strongly influenced by side chains. Well-established empirical structure frequency correlations find that β -sheets have a strong absorption band near 1630–1640 cm⁻¹ and a weaker band at high frequencies (>1680 cm⁻¹) (Natalello et al., 2008). The peaks for α -helices and random coils are located at 1640–1660 and 1640–1650 cm⁻¹, respectively (Natalello et al., 2005). The secondary structure sensitivity of amide I results from coupling between amide I oscillators that leads to vibrational states delocalized over large regions of the protein. Literature lacks about vary applications of these methods to self-assembling peptides forming fibers apart for the work of Di Foggia et al (Tinti et al., 2008) and for the work of Miller group (Yan et al., 2008). But it was demonstrated that these two methods could be perfectly applied to the study of the assembly of this kind of peptides.

- *Imaging techniques*

The atomic force microscopy (AFM) or scanning force microscopy (SFM) is included in a wider group of techniques named scanning probe microscopies (SPM). In all these techniques, the surface of the sample is scanned by a probe, following parallel lines, measuring a local interaction in the near-field region, and registering its value for each position. Thus, the probe is always the basic component of SPM, conditioning the resolution of each microscope.

It should be stressed that AFM and STM are only the most used and further developed SPM techniques. While AFM is based on the detection of repulsive and attractive surface forces, and STM on the electron tunnel effect, there are other SPM techniques based on the measurement of other physical properties. Citation of AFM experiments have grown exponentially since its birth. The applicability of AFM for biological imaging in their native environment was demonstrated shortly after the discovery of this technique. Through time AFM has become a successful tool, which complements other structural techniques as electron microscopy, above cited spectroscopy or NMR. There are three main modes to operate with AMF: contact mode (CM), non contact mode (C) and tapping mode (TM). Data gained in non contact mode are also processed in phase mode or aplitude mode. In the c-mode the biomolecules need to be bound to the surface and this are not easily moved away from their place by the force applied through the AFM tip. The principles on how the AFM works are very simple. An atomically sharp tip is scanned over a surface with feedback mechanisms that enable the piezoelectric

scanners to maintain the tip at a constant force or height above the sample surface. Tips are made from Si_3N_4 or Si, and extended down from the end of cantilever. The AFM head uses an optical detection system in which the tip is attached to a reflective cantilever. A diode laser is focused onto the back of reflective cantilever. When the tip scans the sample surface, the laser beam is deflected from the position in the detector. The signal is the difference in light intensities.

The architecture of a typical AFM is shown in the Fig.3.

Since the self-assembling peptides was discovered in the past ten years the AFM technique was used to investigate about the morphologies adopted by the peptides in dry mode or in different kind of solution. Many works of the Zhang's group (Park et al., 2006) (Hwang et al., 2004) shown how this is a powerful methodologies to confirm simulation data or support other structural data.

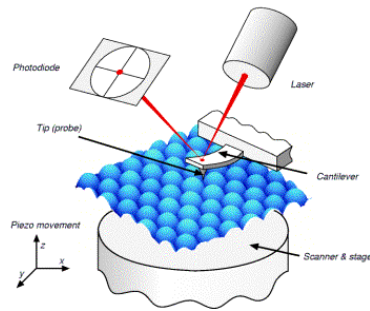


Fig3. Example of AFM architecture

4 MATERIALS AND METHODS

4.1 Synthesis and purification of self-assembling peptides

The functionalized self-assembling peptides were made by extending the original RADA16 sequence at the C-terminus with different biologically active motifs.

Solid-phase synthesis (Fmoc-synthesis) of functionalized peptides was performed by using the CEM Liberty automated microwave peptide synthesizer on 0.200g Rink amide MBHA resin (0.50 meq/g substitution). Deprotection was performed using 20% piperidine with 0.1 M HOBt in DMF. Cleavage was performed using 15 ml of Reagent K (TFA/phenol/water/thioanisole/EDT; 82.5/5/5/2.5) for 180 min. Following removal of the TFA and scavengers, peptides were precipitated and washed with clean diethyl ether.

Prior to LC-MS analysis, peptide was dissolved in 25% acetonitrile solution and lyophilized to dryness. The crude peptide was analysed and purified by reverse phase HPLC using a Waters HPLC system equipped with an analytical and semi-preparative BioBasic C4 300 °A (Thermo Scientific, UK). The gradient elution system for the columns was 0.1% TFA in water (buffer A) and 0.1% TFA in acetonitrile (buffer B). The BioBasic column was eluted with a gradient from 10% to 100% of buffer B in 35 min at a flow rate respectively of 1 ml/min and 20 ml/min in analytical and semi-preparative conditions. The peaks were detected at 214 and 254 nm. After HPLC, HCl exchange was performed at a volume of 1:1 in order to extract residual TFA. Then, the purified peptides were dried again. The peptides used in this work were dissolved in sterile water (SALF, Bergamo, Italy) at a final concentration of 1% (w/v) and sonicated for 30 min before use.

4.2 AFM imaging

FPs at a concentration of 1% w/v solution were diluted (in a ratio of 1:100) in sterile water, 5 µl of these solutions were placed on mica muscovite substrates and kept at room temperature for 1 minute. The mica surfaces were then rinsed with Millipore-filtered water to remove loosely bound peptides and dried under a gentle stream of gaseous nitrogen. AFM images were collected in tapping™ mode by a MultiMode Nanoscope IIIa (Digital Instruments) under dry nitrogen atmosphere using single-beam silicon cantilever probes (Veeco RTESP: resonance frequency 300 KHz, nominal tip radius of curvature 10nm, forces constant 40 N/m). For high spatial resolution a cantilever probe with a resonance frequency 320 KHz, nominal tip radius of curvature 2-5 nm, forces constant 42 N/m (Veeco TESP-SS) was also used. If

necessary, data sets were subjected to a first-order flattening. Measured fiber dimensions with RSTEP were corrected because of the convolution effect arising from the finite size of the AFM tip. Being the observed tabular nanofiber heights (between 1 and 1.5 nm) far lower than the tip radius (10nm) the observed widths were corrected with the formula: (Jun et al., 2004, Taraballi et al., 2009)

$$\Delta x = \sqrt{2[h(2r_t - h)]}$$

Where Δx is the width broadening effect, h is the nanofiber height, and r_t is for tip radius. The diameter of globular aggregates has to be corrected with the formula:

$$R = w^2/(16r_t)$$

Where R is the corrected radius, w is the measured width, and r_t is the tip radius. In both cases the tip is assumed to be a perfect sphere and fibers are considered as tabular structures, and aggregates as spherical ones.

4.3 Raman spectra collection and analysis

Raman spectra were collected both on solutions and on dried samples obtained either from water evaporation or 12h treatment in a lyophilizer (Labconco). Powder samples were deposited on a silicon wafer after the latter procedure gave the best signal-to-noise ratio with no interference from the water phonon spectrum. No detectable modification of the Raman pattern resulted from water removal. Measurements were carried out using the 632.8 nm line of a He-Ne laser as the light source and collecting the scattered light signal in backscattering geometry by a Raman spectrometer (Labram Dilor). The laser was focused on the sample with a spot diameter of about 2 μm . Care was taken to avoid laser induced sample heating. For this purpose, direct measurements of the sample temperature in the chosen experimental configuration at various laser power values and exposure times were collected analyzing the ratio between Stokes and anti-Stokes Raman modes of reference samples. In all cases the estimated sample temperature was lower than 30 °C. The signal was detected by means of a CCD (Jobin-Yvon Spectrum One 3000), with a spectral resolution of 1 cm^{-1} , by averaging 10 spectra obtained with an acquisition time of 180 s each. Background from the silicon micro-Raman spectrum, although almost negligible in the investigated 900–1800 cm^{-1} spectral range containing the main features of the protein spectra, was subtracted. Spectra were then normalized to the peak at $\sim 970 \text{ cm}^{-1}$ from C–C stretching.

A protein's vibration mode, amide I band, appears in the 1600–1700 cm^{-1} region of the Raman spectrum. This region is a function of the secondary structure of the protein. The amide I region was fitted with Origin 7. A Gaussian interpolation function was employed.

The amide I band at $\sim 1610 \text{ cm}^{-1}$, accounting for ring modes from Phe and Tyr side-chains, has been included along with other amide I bands only when necessary (for RADA16-I-BMHP1 and RADA16-I-ALK). The region considered in the band fitting procedure goes from 1630 cm^{-1} to 1700 cm^{-1} . The baseline from 1550 cm^{-1} to 1750 cm^{-1} was assumed to be linear. Comparison of the χ^2 values and R^2 value was used as the criteria for assessing the quality of fit. The high-energy spectral region around 2900 cm^{-1} was also analyzed, looking at the relative intensities, to observe the solvent effects on the CH_2 , CH_3 , and aromatic CH_2 stretching modes.

4.4 ATR/FTIR spectra collection and analysis

Each peptide was dissolved at a final concentration of 0,1%(w/v) in different buffers with a specific pH to test the assembling process.

Two buffers were employed to analyze the peptide structure: buffer 1 at pH 8 (NaOH 5 mM); buffer 2 at pH 2 (HCl 1.2 mM). The sample pH was measured by a digital pH-meter. Moreover, in order to displace the samples pH, other two buffers were used: buffer 3 (NaOH 15 mM) to shift pH from 2 to 8; buffer 4 (HCl 25 mM) to shift the pH from 8 to 2. We adopted this notation for sake of simplicity during tractation. Buffer 3 was used to resuspend the sample in buffer 1 after the evaporation of buffer 1. The same procedure was used for buffer 4, after the evaporation of buffer2.

FTIR spectroscopy was employed for the peptide characterization, since it enables to detect their secondary structure and the formation of β -sheet intermolecular interactions in peptide assembly. In addition, it can work at the same peptide concentration used in their vitro and in vivo experiments, while Circular Dichroism (CD) spectroscopy requires lower concentrations different from those of their standard use.

FTIR measurements in attenuated total reflection (ATR) were performed using a single reflection diamond element (Golden Gate, Specac, USA). The FTIR spectrometer FTS-40A (Bio-Rad, Digilab Division, Cambridge, MA), equipped with a nitrogen cooled mercury cadmium telluride detector and an air purging system, was employed under the following conditions: 2 cm^{-1} spectral resolution, 20 kHz scan speed, 1000 scan co-addition, and triangular apodization. 5 μl of each peptides sample at pH 2 and pH 8 were deposited on the ATR plate and spectra were recorded after solvent evaporation to allow the formation of a hydrated peptide film. After these measurements, the same samples

were re-suspended using buffer 3 (for the pH 2 samples) or buffer 4 (for pH 8 samples), and the spectra were recorded again after the solvent evaporation. The spectra of 0,1 mg of the same peptide in lyophilized state was also recorded.

ATR/FTIR spectra were reported after normalization on the Amide I band area to compensate for possible differences in the peptide content.

4.5 Thermal treatment monitored by FTIR spectroscopy

For thermal unfolding studies, peptide samples were dissolved in deuterated water (D₂O) at 4 mg/ml concentration and 15 μ l of the above solutions were placed in a temperature-controlled cell (Wilma, Buena, NJ, U.S.A.), made of two BaF₂ windows separated by a 100 μ m Teflon spacer. The samples were then heated at a constant rate of 0.2 $^{\circ}$ C/min over the range from 30 $^{\circ}$ C to 100 $^{\circ}$ C and FTIR measurements of peptide solutions were recorded in the transmission mode under the same condition employed for ATR/FTIR spectra. The absorption spectra of the peptides were obtained after subtraction of the D₂O solvent absorption from that of the peptide solutions. The Amide I components, reflecting the different secondary structures and β -sheet intermolecular interaction in peptide assemblies, were identified via second derivative analysis of the measured the absorption spectrum (Susi and Byler, 1986) following the Savitsky-Golay procedure (5 points) after a binomial smoothing (11 points) of the spectrum (GRAMS/32 software). During thermal treatment, the dissolution of the intermolecular β -sheet structures was reported as percentage variation of the 1618 cm^{-1} band intensity, evaluated from the second derivatives of the absorption spectra (Javor et al., 2008).

4.6 Molecular Dynamic Simulation scheme

We ran molecular modeling simulations with CHARMM (Brooks et al., 1983) version 29 software with PARAM19 force field (Brooks et al., 1983). In all MD simulations the solvation effect was incorporated by using the analytic continuum electrostatics (ACE2) (Schaefer and Karplus, 1996) module in CHARMM. It calculates the solvation free energy including the entropic contribution from water, based on a linearized treatment of the generalized Born solvation model, which has been shown to describe solvation effect properly unless there are specific effects mediated by discrete water bridges. Histidine residues were protonated, to account for the experimental condition of neutral pH. The filament structures were constructed as a β -sheet bilayer using 15 peptides on each sheet. As described previously, backbone hydrogen bonds between peptides on each sheet were formed between the

RAD16-I part of the peptide, thus leaving the functional groups to “stick out” from the filament. After building the filament structure, the system was initially energy-minimized for 200 steps using the steepest descent method, followed by 3000 steps of the adopted-basis Newton-Raphson (ABNR) method. The system was then heated from 0 K to 300 K over 100 ps, and equilibrated for 300 ps. The final production run lasted for 1 ns with the leap-frog integration method using a time step of 2 fs, and a frequency of saving coordinates of 0.8 ns. Simulations were repeated five times for each peptide with different values of random number seeds. Moreover 200 ps MD simulations for each peptide were run at different temperatures (300 K, 350 K, 400 K and 450 K), to test the stability of the structure (data not shown). Lengths of the bonds connecting hydrogens to heavy atoms were fixed by using the SHAKE algorithm. Visualization of molecular conformations, each one representative of the five runs, and MD trajectories were performed using VMD. A long equilibration period of the aligned peptides in extended conformations was to ensure full relaxation of the initial structure. A separate, 2 ns MD at 450 K was performed on a single peptide and the solvent accessible surface area (ASA) of the side-chains was calculated every 80 ps. To calculate ASA, we used the algorithm of Shrake and Ripley, with a probe of radius 1.4 Å. We also calculated the mean ASA per residue as a function of time as another indicator of the average solvent accessible surface area of each peptide.

4.7 Neural stem cell cultures growth on self-assembling peptides

Briefly, neural precursors isolated from the sub ventricular zone (SVZ) of 8-week-old CD-1 albino mice striata, at passage 10, were used. Cell proliferation was performed in Neurocult basal medium serum-free medium (StemCellTechnologies, Canada), in the presence of basic fibroblast growth factor (β FGF from PeproTech, Rocky Hill, NJ) and epidermal growth factor (EGF from PeproTech) at final concentrations of 10 ng/ml and 20 ng/ml. The medium without growth factors was used as a basal medium. Cell seeding (at a concentration of $2-8 \times 10^4$ cells/cm²) was performed two days after the last mechanical dissociation in order to seed the maximum percentage of stem cells. Cells were seeded on the top-surface of each assembled nanofibrous scaffold. NSCs were cultured with basal medium supplemented with β FGF (10 ng/ml), added to enhance neuronal progeny differentiation. After 3 days, the medium was shifted to a medium containing Leukemia Inhibitory Factor (LIF, Chemicon) (20 ng/ml) and Brain Derived Neurotrophic Factor (BDNF, Peprotech) (20 ng/ml) to pursue the neuronal and glial population maturation in NSC progeny. Serum-free cell culture media were chosen to avoid random serum proteins

adsorption within the scaffolds. Cells were fed every three days with the same fresh culture medium. The MTT assay, MTT [3-(4,5-dimethylthiazol-2-yl)-2,5-diphenyl tetrazolium bromide], has been used to test the proliferation of the cells grown on the biomaterial. Cellular viability was determined by measuring the absorbance of the converted dye at a wavelength of 595 nm. Phase contrast images of the adhering cells were acquired via inverted microscope (Axiovert, Zeiss) at one week after seeding. Experiments were repeated twice with three replicates at each time.

4.8 Biopolymer electrospinning and tube synthesis

Poly(DL-lactide-co-glycolide) (PLGA, 75:25, MW 66,000-107,000) and poly(ϵ -caprolactone) (PCL, MW 80,000) were purchased from Sigma-Aldrich, St. Louis, Missouri. Chloroform and methanol solvents were purchased from Mallinkrodt and Sigma-Aldrich, respectively. A solution of 5.5% (W/W) PCL and 4% (W/W) PLGA, was mixed in 3:1 chloroform:methanol. A solution of 15% PCL in chloroform was also created.

The electrospinning apparatus was designed with a Gamma High Voltage Research HV power supply linked to a 16 cm-wide flat plate. A Harvard Apparatus PHD 2000 infusion syringe pump dispersed solution at a rate of 0.05 ml/min through a 35 cm Teflon tube connected to a metal needle (inner diameter: 1.06 mm) protruding through the flat plate. Fiber lumen mats were collected on a round, flat target coated with nonstick Reynolds aluminium foil. The distance between the charged plate and grounded target was 32 cm. Current was measured using a Fluke 189 True RMS Multimeter in series with a 1 Megohm resistor. Voltage was set at 34 kV for the 15% PCL solution and 25 kV for the PCL/PLGA solution (Hohman M, 2001) To create the sciatic nerve tube implants, micro- and nanofibers were deposited on a 16-gauge copper wire (diameter: 1.29 mm) held near the grounded target. The wire was grounded and rotated to assure even coating. A base of larger PCL fibers was deposited for 60 seconds followed by a 120 second coating of smaller PCL/PLGA fibers (total wall thickness: ~ 155 μ m). The coating of larger PCL fibers grants mechanical stability and elasticity while the smaller PCL/PLGA fibers form a tight-knit outer mesh. Samples were annealed for 24 hours at 55°C under vacuum to remove any possible residual solvent and further crystallize PCL segments for added mechanical strength.

Fiber diameter and wall thickness were measured using a JEOL JSM-6060 Scanning Electron Microscope. Samples were coated with 10 nm of Au/Pd using a Polaron Range sputter coater prior to imaging.

AnalySIS software by Soft Imaging Systems was used to measure individual fiber diameters in SEM images.

Pure PCL fibers ranged in diameter from 2.5 μm to $\sim 8.0 \mu\text{m}$, with an average of $7.48 \pm 2.02 \mu\text{m}$. The surface of these fibers was found to be quite rough, with grooves $\sim 200 \text{ nm}$ wide running parallel to the fiber axis. PCL/PLGA fibers possessed a diameter of $279 \pm 87 \text{ nm}$, with fibers spanning 140 nm to 500 nm.

4.9 Histochemical, immunofluorescence and immunoistochemical analysis

For histochemical analysis, slices were stained with hematoxylin-eosin and Bielschowsky reaction, a silver staining for axons in which nervous fibers are sensitized with a silver solution, the sections are treated with ammoniacal silver, and then reduced to a visible metallic silver (Bielschowsky, 1908). For immunofluorescence analysis, the following primary antibodies were used: anti-neurofilament NF200 (Sigma, Sant Louis), anti-myelin MBP (Sternberger Monoclonals Incorporated, Lutherville) and anti-CNPase (Chemicon International, Temecula), anti-rat macrophage marker CD68 (Serotec, Dusseldorf), anti-prolyl 4-hydroxylase fibroblast marker (Acris Antibodies, Hiddenhausen), anti- β -tubulin (Berkeley Antibody Company, Berkeley), anti-rat Collagen IV (Cedarlane, Hornby).

Primary antibodies were then probed with the secondary antibody ALEXA 488 (Molecular Probes) or CY3 (Jackson Immuno Research, West Grove). Cell nuclei were stained with DAPI (Molecular Probes). Sections were mounted with FluorSave reagent (Calbiochem, Darmstadt) and examined by an upright Nikon200 fluorescence or confocal microscope (Zeiss). In the case of neural tracer imaging, sections were mounted with FluorSave and inspected.

Confocal and upright fluorescence microscope images (4x and 10x magnification) of the sciatic nerve transversal sections of group 3 (N = 12 rats) were acquired to quantify the regenerated nerve area. Areas were quantified at specific location numbers representing the distance from the proximal side as a percentage of the total length: -25% and 125% represent sections obtained outside of the conduit on the proximal and distal sides respectively (Rutkowski et al., 2004). Measurements of the cross-sectional area positive to Bielschowsky staining and to β -tubulin and neurofilament NF200 antigens were carried out with NIH image software ImageJ. Positive pixel area was then converted to mm^2 scale.

5 RESULTS AND DISCUSSION

This thesis section is divided in two subsections: the first chapter will introduce the theoretical and experimental investigation about the stability of β -cross structure adopted by self-assembling peptides forming fibers. Indeed the second chapter will describe an example of use of biomaterial for the nerve tissue regeneration.

5.1 From the theory to the new design and *in vitro* application

5.1.1 Effect of functionalization on the self-assembling propensity of β -sheet forming peptides

The mechanism underlying self-assembly of short peptides has not been fully understood despite a few decades have passed since their serendipitous discovery. RADA16-I, representative of a class of self-assembling peptides with alternate hydrophobic and hydrophilic residues, self-assembles into β -sheet bilayer filaments. Though a sliding diffusion model for this class of peptides has been developed in previous works, this theory need further improvements, supported by experimental investigations, to explain how RADA16-I functionalization with biological active motifs, added at the C-terminus of the self-assembling core sequence, may influence the self-assembling tendency of new functionalized peptides (FP). Since FPs recently became a promising class of biomaterials for cell biology and tissue engineering, a better understanding of the phenomenon is necessary to design new scaffolds for nanotechnology applications. In this work we investigated via Atomic Force Microscopy and Raman spectroscopy the assembly of three RADA16-I FPs that have different hydrophobic/hydrophilic profiles and charge distribution. We performed molecular dynamic simulations to provide further insights into the experimental results: functionalizing self-assembling peptides can strongly influence or prevent molecular assembly into nanofibers. We also found certain vibrational molecular modes in Raman spectroscopy as useful indicators for elucidating the assembly propensity of FPs. Preliminary FPs designing strategies should therefore include functional motif sequences with balanced hydrophobicity profiles avoiding hydrophobic patches, causing fast hydrophobic collapses of the FP molecules, or very hydrophilic motifs capable of destabilizing the RADA16-I double layered β -sheet structure.

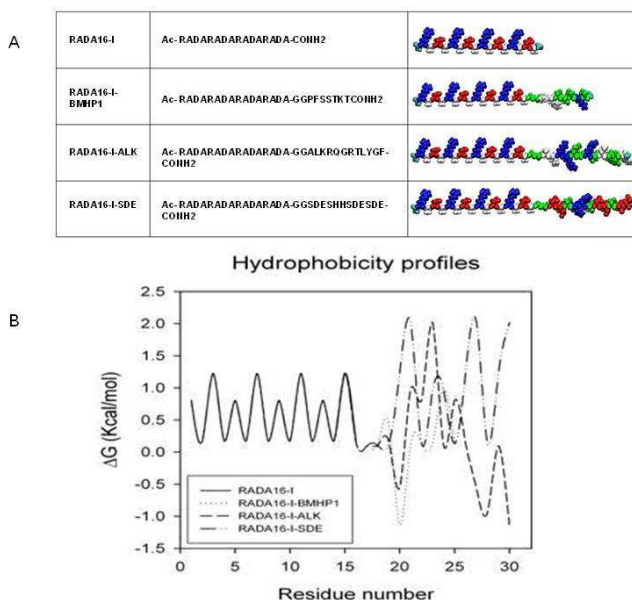
RADA16-I has been used as a three-dimensional cell culture scaffold for endothelial cells, (Sieminski et al., 2008) neural progenitor cells, (Semino, 2008) cardiac myocytes, (Davis et al., 2006) etc. The hydrogel can be customized for specific applications by linking various functional groups at the N- and C-terminus (Gelain et al., 2006). RADA16-I has been chosen as a self-assembling core to which a spacer consisting of two glycines and various biologically active motifs can be attached (Gelain et al., 2006). The Gly-Gly spacer is adopted to provide the FP with a highly flexible linker connecting the RADA16-I sequence, that is the assembling portion of FP, and the functional motif. This flexibility is considered as fundamental for the correct exposure of the functional motif to cell membrane receptors (Gelain et al., 2006). When RADA16-I is functionalized with the bone marrow homing peptide BMHP1 (PFSSTKT), it is capable of stimulating neural stem cell adhesion, proliferation and differentiation; when extended with bone-cell secreted signal peptide ALK (ALKRQGRTLYGF) it promotes mouse osteoblasts proliferation and differentiation (Horii et al., 2007); while the functionalization with the osteopontin derived peptide sequence SDE (SDESHHSDESDE), a bone ECM molecule regulating cell adhesion, migration and survival, (Horii et al., 2007) is a FP newly designed for bone regeneration applications.

Although our previous studies demonstrated the potential of FPs, they also suggested that different functional motifs significantly influence the propensity for self-assembly and the overall mechanical properties of the scaffold at the meso-scale. (Gelain et al., 2006)

To address this issue, we investigated the three abovementioned RADA16-I derived FPs (see Scheme 3a) by using a combination of material characterization techniques and molecular dynamic simulations. Notwithstanding RADA16-I has been characterized in various studies, the other FPs, derived from the same 16-mer core, still have to be fully characterized and their self-assembly explained. The three FPs tested differ in length, charge distribution, and hydrophobicity. The stability of the cross- β structure of each peptides was investigated using MD simulations. We also analyzed the assembled structures via Raman spectroscopy and atomic force microscopy (AFM), which were consistent with the “*in silico*” findings.

Raman micro-spectroscopy, a well-established technique already applied to characterize the molecular structure of proteins like amyloid protein α -synuclein (Apetri et al., 2006), has been used to investigate in a greater detail the secondary structure of the self-assembling peptides. As the same experimental conditions were

adopted in all tests, Raman spectra and AFM nanostructure morphologies analyzed can be directly correlated. Our results indicate that hydrophobicity of the functional group is a major factor responsible for the overall assembly: functionalization with too hydrophilic or too hydrophobic groups does not lead to filament assembly. Thus, when designing a FP, the sequence of the base peptide, the linker between the base peptide and the functional group must be adjusted to accommodate the hydrophobicity of the functional group, or *vice versa*. Lastly our work indicated Raman spectroscopy as a powerful technique for assessing peptide assembly in aqueous solutions, results confirmed and supported by MD and AFM tests. When applied to a wide spectrum of FPs, the synergistic use of computational and experimental modalities would be useful in elucidating their design principles.



Scheme3. A) The peptides used in this study. In the self-assembling “core” sequence basic residues (blue) alternates with acid residues (red) and hydrophobic ones (white). Polar neutral residues (green) are present in added functional motifs. A spacer of two glycines has been added between the self-assembling cores and the functional motifs. B) Superimposed hydrophobicity profiles of the tested peptides (see methods for details), positive values testify hydrophilic residues while negative ones are for hydrophobic patches.

Four different self-assembling peptides, comprising a self-assembling sequence and three functionalized versions of the same self-assembling “core”, showing various hydrophobic profiles at

their added functional motifs, have been analyzed (Fig.4) via molecular dynamics in order to understand their self-assembling propensity.

In details, the three FPs hydrophobicity profiles evince different hydrophobic status of the functional added motifs. RADA16-I-SDE peptides show charged or neutral residues, meanwhile RADA16-I-BMHP1 and RADA16-I-ALK have balanced functional motifs, and, notably, RADA16-I-ALK peptides shows the most hydrophobic residues of the all four ones (Scheme.3B). Notwithstanding all of the FPs are soluble (at 1% w/v concentration), only RADA16-I and RADA16-I-BMHP1 form macroscopic hydrogels when PBS (Phosphate Buffer Solution, pH 7.4) is added to the FP solutions.

While previous studies confirm our macroscopic findings for RADA16-I and RADA16-I-BMHP1(Zhang et al., 2002, Gelain et al., 2007b)more detailed tests are mandatory to asses the insights of molecular self-assembling of the other FPs, if any, involving a limited number of molecules and consequently not bringing to any structured macroscopic scaffold.

Then, we constructed filaments using the cross- β structure proposed by Park et al., with the RADA16-I part arranged to form a β -sheet bilayer. While these filaments can form larger bundles in experiments, differences in self-assembling propensity manifest at the single-filament level(Park et al., 2006). Thus our simulation on behaviors of pre-formed filaments should give an indicator of the self-assembling propensity of the constituent peptides. During MD, the three filaments exhibited different conformational behaviors (Fig.4). Although not all FPs assembled into filaments in experiments, imposing a filament structure and monitoring its stability in simulations is a way to infer how each functional group affects the self-assembly of the peptide. For RADA16-I-BMHP1 and RADA16-I-ALK, the β -sheet bilayer structure of the RADA16-I part remained stable even at 450 K during the simulation period (Fig.4A-B). The balance between hydrophobic and hydrophilic interactions plays a pivotal role in controlling the aggregation propensity and the aggregate morphology: if the added group is too hydrophobic, while aggregation is promoted, it is difficult to form an ordered fibril, since it is kinetically easier to form globular aggregates. On the other hand, strongly hydrophilic groups prevent aggregation and may impair solubility of the peptides. To better understand the influence of the peptide sequence on self-assembly, we monitored the solvent Accessible Surface Area (ASA) of a single peptide molecule during 2-ns MD simulations at 450 K (calculated every 80 ps; Fig. 5). The overall ASA profiles were consistent with the hydrophobicity of the peptides. In the case of the most hydrophobic RADA16-I-ALK, the

profile changed the least over the course of the simulation, maintaining one broad region of low ASA (AA 14-19), suggesting that the peptide underwent hydrophobic collapse right after the simulation started (Blue bands Fig. 5B). The less hydrophobic RADA16-I-BMHP1 shows overall higher ASA (average 55\AA^2) (Fig. 5A), although it is smaller than the most hydrophilic RADA16-I-SDE (average 97.74\AA^2).

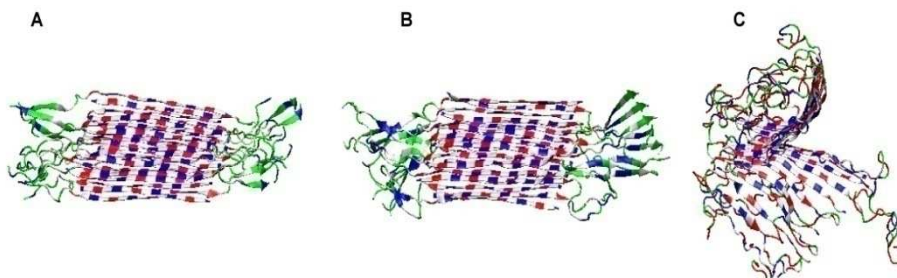


Fig.4. Final conformations of initially imposed β -sheet bilayer structures (15 molecules on each side) after 1-ns MD simulations ($n=5$). A) RADA16-I-BMHP1, B) RADA16-I-ALK, C) RADA16-I-SDE. Color schemes for residues are: blue (basic), white (hydrophobic), red (acidic), and green (polar). In the “cartoon” representation, arrows represent β -sheet structures. Notably, in (A) and (B) the functional groups form clusters and the bilayer structure remained stable during MD, while in (C) no clusters were formed among the functional groups and the two layers split.

The mean ASA for residue has been considered, as function of time, as a way to understand easily the behavior of each peptide. At 160ps of MD RADA16-I-SDE has 106\AA^2 of mean surface expose to solvent, while RADA16-I-BMHP1 has 87\AA^2 and RADA16-I-ALK 75\AA^2 . Moreover at 1000ps, RADA16-I-SDE maintains a high value mean surface area exposed (100\AA^2) till the end of simulation. RADA16-I-ALK also maintains 58\AA^2 of mean surface area till the end, instead RADA16-I-BMHP1 remains stable around a value of 76\AA^2 and only at 1600ps its mean surface area value of 60\AA^2 .

The swift hydrophobic collapse of RADA16-I-ALK molecule suggests that this peptide likely forms disordered aggregates since it would be difficult to self-assemble into double layer β -sheet structured nanofibers after the competing formation of random clusters. As to RADA16-I-BMHP1, as individual molecules explore wider conformational space, upon aggregation, they can still rearrange after assembly and make a transition into ordered fibrils. Our analysis of the ASA profile corroborates the proposed role of the balance between hydrophobic and hydrophilic interactions. Also, the effect of conformational flexibility of individual molecules – from RADA16-I-ALK (collapsed), to RADA16-

I-SDE (random coil-like) - is consistent with the view that partial denaturation of protein is an important condition for amyloid fibril formation (Fairman and Akerfeldt, 2005, Horii et al., 2007).

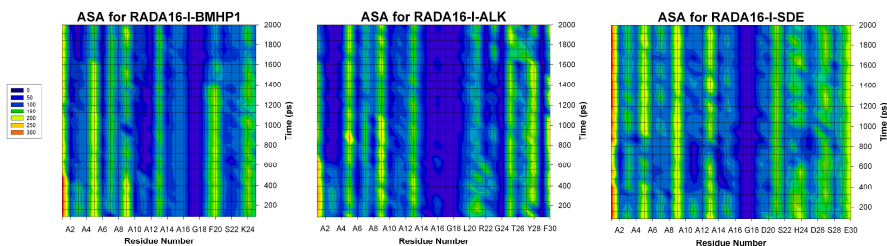


Fig.5. ASA profiles of individual side chains (single molecules per each investigated peptide) during 2-ns MD at 450 K. ASA calculations were obtained every 80 ps. The radius probe used is 1.4 Å.

AFM imaging showed remarkably different nanostructures among the four tested self-assembling peptides (Fig. 6). RADA16-I, the self-assembling “core” shared by the other FPs, forms nanofibers (Fig. 6A), as widely described in the previous works (Yokoi et al., 2005). The nanostructure of RADA16-I-BMHP1 (Fig. 6B) looks similar to the RADA16-I structure (Yokoi et al., 2005), in spite of an average nanofiber width (14.0 ± 1.6 nm) significantly larger than that one measured for RADA16-I nanofibers (9.4 ± 1.2 nm) whereas fiber thickness is observed to be multiple of 0.5 nm for both materials. The increase of the nanofiber width is expected as the effect of the added functionalized tails flagging from the self-assembled cores (Gelain et al., 2006, Horii et al., 2007). These findings suit with the molecular model of self-assembled molecular structures proposed by Zhang and colleagues for RADA16-I and its derived FPs. Width values are expressed as an average of multiple measurements corrected as described in the methods section. Noteworthy, the observed fibrillar assemblies give rise to fibers with multiple heights due to the formation of multiple layers, while the pace of these same heights is consistent with a double β -sheet model.

On the other hand RADA16-I-ALK nanostructure shown in Fig. 6C is remarkably different from those previously described. Indeed, RADA16-I-ALK molecules make globular aggregates rather than nanofibers and, as no recurrent lengths of these round-shaped aggregates have been detected, they seem to be non-ordered structures. In order to provide an indication of the average size of these aggregates, we considered their shape as actually spherical.

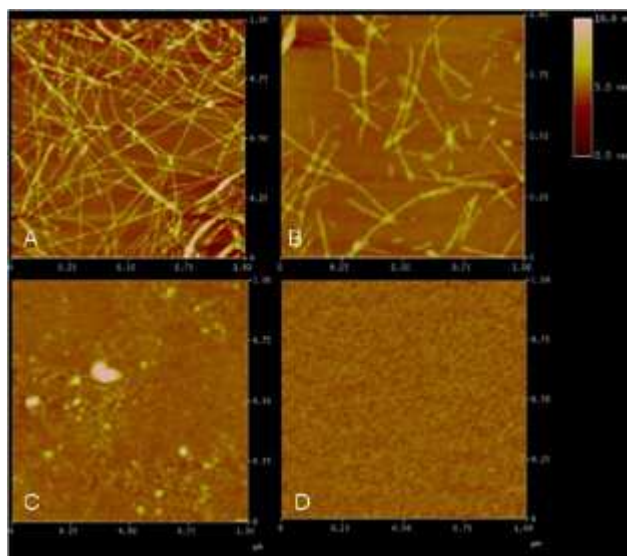


Fig.6.AFM images of the tested peptides at a concentration solution of 1% (w/v). A) RADA16-I self-assembles into nanofibers (average width: ~10 nm). B) RADA16-I-BMHP1 self-organize into nanofibers larger than those shown in (A) (~15 nm wide), this increase is due to the addition of the functional motif at the C-terminal. C) RADA16-I-ALK aggregates into globular structures of ~15 nm average diameter. D) RADA16-I-SDE evenly coats the mica surface.

The observed globes showed a wide spread size distribution; however, the average size of the aggregated particles is 15 ± 2 nm. Noteworthy, even isolated tiny particles were observed.

The globular shape of RADA16-I-ALK can be explained by the increased hydrophobicity given by the added functional motif. Compared to other intermolecular forces such as electrostatic and van der Waals interactions, hydrophobic interactions is longer-ranged thus is more relevant to earlier steps of aggregation. Indeed, as shown by the MD and the achieved stable ASA conformation, it is possible to that the strong hydrophobic effect in RADA16-I-ALK promotes the aggregation toward a kinetically trapped, globular structure rather than into more ordered fibrils (Schaefer and Karplus, 1996), thus exposing a decreased surface area to the solvent. To kinetically favor the formation of fibers for RADA16-I-ALK additional AFM experiments had been performed at peptide concentrations of 1% w/v. Indeed sporadic nanofibers were detected at such high concentration (Fig.7).

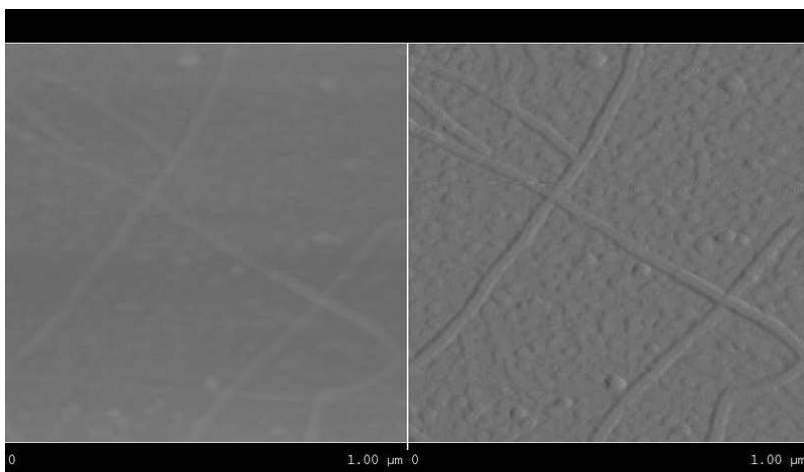


Fig.7. RADA16-I-ALK solution in MilliQ was used to a final concentration of 1% w/v. 5 μ l peptide solution was placed on mica surface and after 1 minute of adsorption the sample was washed with MilliQ water and dried carefully under a stream of nitrogen.

Still nanofiber formation for RADA16-I-ALK can be considered as a secondary phenomenon if compared to the occurrence of nanostructures in the case of RADA16-I and RADA16-I-BMHP1. RADA16-I-ALK fiber thickness is similar to RADA16-I and fiber average width (19 ± 1.5 nm) is consistent with a β -cross molecular structure. This experimental finding is in accordance with the MD data, where a statistically favored self-assembled nanofiber is a stable secondary structure.

RADA16-I-SDE (Fig.6D) exposure to PBS did not induce a detectable assembled nanostructure; however, an accurate observation of the sample surface and a comparison with images acquired in the same conditions on the bare mica surface evince that a uniform layer (rms: 0.2 nm) is formed on the mica surface. In order to confirm the presence of the peptide over the mica surface we managed to dig a square on the sample surface and measure the thickness of the layer itself (Fig.8).

From these measurements it is possible confirm that RADA16-I-SDE form a uniform monolayer on mica surface. RADA16-I-SDE does not arrange itself in a definite structure as indicated by the MD. The scarce self-assembling propensity of this FP is rather expected: ASA calculation shows a high and varying surface area exposed to the solvent. The highly hydrophilic SDE motif added to RADA16-I perturbs the otherwise stable structure of RADA16-I.

We also investigated the molecular vibrational modes evinced in the Raman spectra of the investigated materials in the range 900-1800 cm^{-1} (Fig.9).

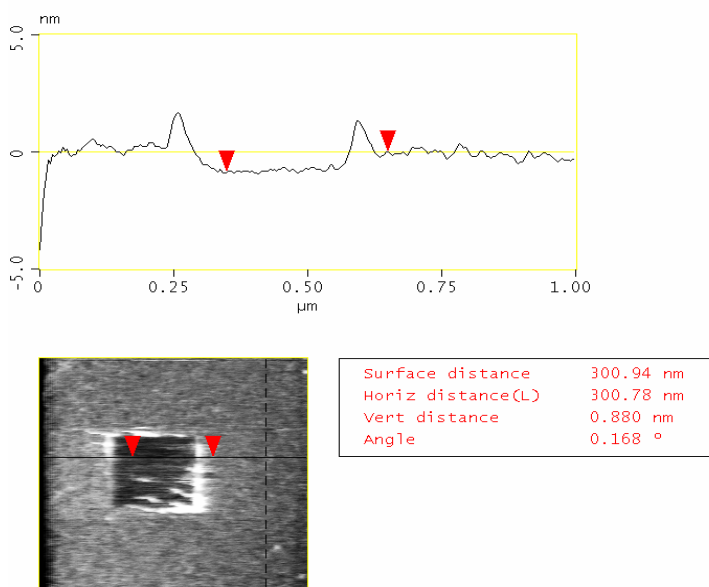


Fig.8.RADA16-I-SDE solution was diluted to a final concentration of 0.01% w/v. 5 μ l peptide solution was placed on mica surface and after 1 minute of adsorption the sample was washed with MilliQ water and dried carefully under a stream of nitrogen. All the images were taken in air in contact mode with a nominal spring constant of 0.16 N/m.

Several peaks and structured bands fall in this spectral region forming the patterns typically observed in proteins (Table 2), with spectral features grouped in contributions given by vibration modes of the backbone structures from C-C and C-N stretching (Jun et al., 2004) in the range 900-1100 cm^{-1} combination modes from C-N stretching and N-H bending involved in the peptide backbone in the range 1200-1300 cm^{-1} (amide III region)(Meyer et al., 1996), bending modes associated to CH_2 and CH_3 deformation in the 1300-1500 cm^{-1} regions, and C=O stretching mode at 1600-1700 cm^{-1} in the amide I region(Torreggiani et al., 2008). Further peaks are observed in two FPs (RADA16-I-BMHP1 and RADA16-I-ALK) due to ring vibrations of aromatic side-chains. Information on the secondary structure of peptides may be obtained from the analysis of the amide regions (Torreggiani et al., 2008). Particularly, the shape of the amide I band gives evidence of the contributions from α -helices, β -sheets, and unstructured β -strands. Indeed, peak conformation and possible asymmetries of the amide I band suggest a distribution of secondary structures. The analysis in Gaussian components shows that this region is satisfactorily reproduced by three main components with spectral positions and bandwidths reported in Table 3, besides added components accounting for aromatic

residues. The results of the analysis are consistent with findings from previous works demonstrating that the band at 1658 cm^{-1} is a marker of α -helices, the band around 1670 cm^{-1} is associated to β -sheets, while the broad band at higher energy is due to unstructured β -strands. A component above 1700 cm^{-1} arises from C=O stretching from aspartic and glutamic acids and is observed as a shoulder of amide I band in the spectra of Fig. 5. Ionization of carboxylic groups in side-chains may shift this mode to lower energy frequency at about 1405 cm^{-1} . However no relevant contribution of this component was observed.

Raman Spectra Peaks interpretation for the observed dehydrated peptides

RADA16-I Raman shift(cm^{-1})	RADA16-I-BMHP1	RADA16-I-ALK	RADA16-I-SDE	ASSIGNMENTS ^a
1674	1673	1664	1675	Amide I
	1610	1609		Phe/Tyr
1460	1457	1453	1434	δCH_2
1405	1405	1404	1405	νCOO^-
1327	1315	1314	1313	νCH_2
1237	1240	1269	1264	Amide III
	1205	1207		Phe/Tyr
	1157	1173		Phe/Tyr
1088	1086	1105	1086	$\nu\text{C-C}/\nu\text{C-N}$
	1028	1031		Phe
	1001	1003		Phe
980	975	975	974	$\nu\text{C-C}$
939	939	938	922	$\nu\text{C}\alpha\text{-C-N}$

^a Peak assignment are based on previous papers ³⁴ Abbreviations: ν =stretching mode, δ =deformation, γ =in plane bending, Phe= phenylalanine, Tyr= tyrosine

Table 2. principal vibration modes inside the peptide structure.

The different relative intensity of the components in the amide I band reveal a different propensity of the four peptides to take α -helix, β -sheet and unstructured β -strand as secondary conformation. Specifically, RADA16-I-BMHP1 shows a band shape quite similar to the parent molecule, RADA16-I. The band is dominated by the narrow peak at 1674 cm^{-1} , ascribable to C=O stretching in β -sheet aggregation, consistently with the formation of fibers observed in AFM images. The peak broadening in the amide I region is instead peculiar of the spectra of RADA16-I-ALK and RADA16-I-SDE and evinces the predominance of conformations dissimilar from β -sheet ones. By comparing Raman spectra and AFM images, this broadening appears as a clear-cut marker of the failure of fiber self-assembling. Band deconvolution (Table 3) gives further insights on the behavior of these functionalized peptides. In fact, the band broadening is different for the two FPs, and the intensity ratio between the components at 1655 and 1690 cm^{-1} drastically changes, indicating that the unstructured β -strand conformation is dominant in RADA16-I-SDE, while molecule torsions typical of α -helix structure

is favored in RADA16-I-ALK functionalized peptides. As AFM does not provide any reliable clue concerning the secondary structures of these molecules Raman analysis completes the information necessary to understand their assembling propensity. The Raman analysis suggests that the lack of aggregates in the AFM image of RADA16-I-SDE material has to be related to the high hydrophilic features of this FP, since the largely preferred unstructured β -strand random conformation reveals that molecules are not forced by the solvent to adopt a specific shape and consequently to arrange themselves in a secondary structure. A drastically different situation occurs in RADA16-I-ALK material, since AFM images showed aggregates, and sporadic nanofiber formation was detected at higher peptide concentrations. The relatively large contribution of α -helix component in the amide I band, coexistent with the main contribution from unstructured β -strand random conformation, strongly suggests that the molecule backbones do not take part to an ordered assembled structure. Therefore, the observed aggregates probably do not result from ordered self-assembling interactions among molecules, but rather from the nucleation of disordered aggregates formed by molecules whose internal conformation is mainly driven by single molecule hydrophobic tails exposure to the solvent and with no relevant inter-molecular interactions.

In this regard, Raman spectrum analysis in the spectral region of CH_2 and CH_3 deformation modes may give new tools to understand the behavior of this class of FPs. Even though this spectral region has not been considered in the past in the investigation of peptide conformations, it is apparent from Fig.9 that the relative intensity of the deformation band peaked at approximately 1440 cm^{-1} is strongly dependent on the peptide sequence. Specifically, this band is more intense, by a factor 3-4, in materials with no fiber self-assembling (RADA16-I-ALK and RADA16-I-SDE), with also a drastic change of relative intensity if compared with other peptide structures in the phonon spectrum. Indeed this appears as the main feature of non self-assembling peptides. These differences cannot be imputed to the different number of CH_2 and CH_3 groups in the different molecules. In fact, the CH_2/CH_3 calculated number, normalized to the peptide length, gives no notably different value within the set of investigated molecules, showing the maximum positive variation of 20% for RADA16-I, contrary to the relative intensities observed. Similar intensity changes of methyl deformation modes were reported by P ezolet and colleagues concerning poly-L-lysine in solutions at different pH values (Maiti et al., 2004). Although the work of McGarvey's group was focused on other spectral features, the reported results strongly support that the 1440 cm^{-1} intensity change

is strictly related to the pH-induced conformation change of polylysine. In order to verify the relevance of those results in our investigation, we have reproduced the same measurements of poly-L-lysine in the experimental configuration we used to investigate our FPs and results confirmed the effect. Specifically, we observed that CH_2 and CH_3 deformation modes appear extremely sensitive to self-assembling, showing higher intensity in non-assembled structure, either α -helix or β -strand, than in β -sheet fibers.

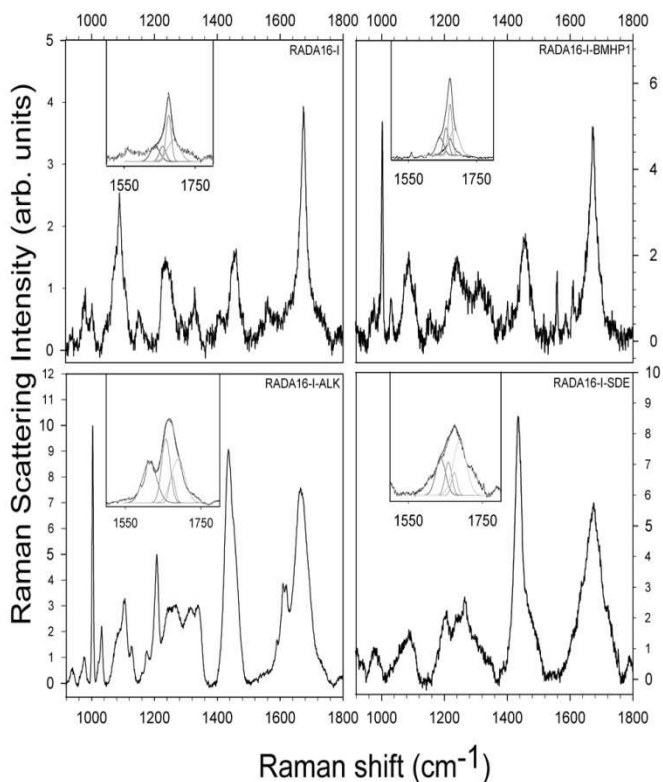


Fig.9. Raman Spectra (900-1800 cm^{-1} region) of the tested self-assembling peptides. Insets: deconvolution of Amide I region (1500-1800 cm^{-1}) for each spectra. Each spectra shows the typical features of proteins: Amide I and Amide III peaks are clearly visible (respectively ~ 1600 - 1700 cm^{-1} and 1200 - 1300 cm^{-1}). A) RADA16-I and B) RADA16-I-BMHP1 show similar spectra with the exclusion of the aromatic features given by the Phe residue in the aminoacidic sequence of RADA16-I-BMHP1. C) RADA16-I-ALK and D) RADA16-I-SDE spectra are significantly different from A) and B) especially in the region of CH_2 and CH_3 bending vibrational mode. Indeed peak intensity of this region appear to be correlated to the self-assembly propensity of FPs, showing higher values in FPs that do not self-assemble.

This is related to a larger Raman cross section of CH_2 bending modes in free configuration compared with situations where

molecules are faced and linked along the backbone through hydrogen bonds. Following this approach, the high intensity in RADA16-I-ALK material gives an important insight on the origin of the inhomogeneous aggregation observed in AFM images, suggesting that the aggregates are formed by randomly interacting molecules. The molecules are forced in α -helix and disordered β -strand conformations by their hydrophobic nature, and are kept together mainly by hydrophobic force, without relevant reciprocal interactions. Raman data give evidence that strong hydrophobic features of RADA16-I-ALK induce the formation of intra-molecular conformations that prevent that the peptide self-assembling in β -sheets, even though β -sheet inter-molecular interactions may probably be stable once they are formed, as suggested by the results of MD and AFM as clear from the Fig.7.

Band fitting and comparison of Amide I region of different FPs.

FP	Center (cm ⁻¹)	Width (cm ⁻¹)	% Area
RADA16-I	1658	18	18.86
	1675	15	40.34
	1689	35	40.80
RADA16-I-BMHP1	1658	18	25.20
	1675	15	12.30
	1689	35	37.55
RADA16-I-ALK	1658	22	42.20
	1674	15	12.30
	1689	35	45.50
RADA16-I-SDE	1658	18	20.10
	1674	15	11.90
	1689	35	68.00

Amide I region was fitted considering the three symmetrical components representing three different structural conformation of proteins: α -helix(1658 cm-1), β -sheet (1675 cm-1) and extended β -strand and PPII structure (1689 cm-1)

Molecular Dynamics simulations showed that the self- assembling propensity of three FPs is dependent on their hydrophobicity profiles. They also provided insights into the AFM and Raman results. In both MD and in AFM imaging, RADA16-I-BMHP1 maintained the β -sheet bilayer filament structure typical of its self-assembling “core” RADA16-I. In contrast, simulation of the RADA16-I-SDE filament showed a marked propensity to open the initial bilayer conformation, likely caused by solvation forces on the hydrophilic groups. In the AFM images, RADA16-I-SDE did not form organized nanostructures; it rather appeared to evenly cover the mica surface. At the end of the MD, RADA16-I-ALK showed a final molecular configuration similar to that of RADA16-I, but the AFM

analysis revealed different globular structures of heterogeneous sizes. ASA calculations also showed differences in the folding kinetic of the tested peptides. Slow folding seemed to be essential for constructing an organized structure, as fast hydrophobic collapse resulted in globular aggregates. Other studies will be necessary in the future to understand if there is a way to increase the formation of nanofibers formed by RADA16-I-ALK. Raman-spectroscopy measurements were performed to analyze with more details the secondary structure of the tested FPs. The decreased β -sheet structure component, showed via the deconvolution of the Amide I region for RADA16-I-ALK and RADA16-SDE peptides, suggested a minor tendency to form β -sheet double layers: indeed intramolecular interactions (mainly α -helix conformations) appeared to be preferred. Moreover, taking into account the CH_2 deformation region, a CH_2/CH_3 bending vibrational mode of RADA16-I-ALK and RADA16-SDE spectra significantly different from its counterpart in RADA16-I and RADA16-I-BMHP1 spectra, suggests a critical role played by this mode in the self-assembling process. MDs give the tendency of self-assembly of the chosen peptides and Raman micro-spectroscopy gave precious insights about the secondary structure of apparently similar self-assembling peptides. Raman spectroscopy data, fairly in accordance with AFM findings and MD simulations, provided new intriguing possibilities to investigate in aqueous solutions or lyophilized state the self-assembled structures of FPs, new promising biomaterials for tissue engineering, drug delivery and other applications. FP designing requires a better understanding of their secondary structure formation as a consequence of the added functional motifs. Thanks the synergistic use of these three different investigation techniques new strategies for designing and synthesizing novel functionalized self-assembling biomaterials can therefore be drawn and developed.

5.1.2 Glycine-spacers influence over functional motif exposure and self-assembling propensity of functionalized peptides

The “bottom up” approach for creating new biomaterials in nanomedicine and tissue engineering is achieving a consistent approval among the scientific community (Colombo et al., 2007). A considerable number of interdisciplinary publications, from physics to biology, describe guidelines to fabricate new nano-biomaterials for specific applications (Reddi, 2000, Drotleff et al., 2004, Hirst and Smith, 2004, Tsai et al., 2007, Ulijn and Smith, 2008). Molecular self-assembly became an alternative paradigm to create functional nanostructures

using spontaneous diffusion and specific association of molecules directed by weak interactions (Weigel et al., 2006). Because of the extensive research regarding proteins and peptides investigating the rationale behind their folding and stability self-assembling peptides claim a remarkable tailorability as building blocks of nanoscaled biomaterials. In peptide based biomaterials the main effort is driven towards the definition of the rules linking peptide sequences to their molecular structure organization and thus their functional properties (Davis et al., 2005). Self-assembling peptides can be prepared via solid-phase synthesis with precise control over sequence, molecular dimension and functionalization. Zhang and his co-workers developed short amphiphilic peptides like RADA16-I, mimicking the properties of extra cellular matrix (ECM) so to be an intriguing scaffold for tissue engineering applications (Yokoi et al., 2005). Depending on the tissue hosting the self-assembled implant (for example bone, cartilage, myocardium and nervous tissue) the required implant biomechanical and biochemical properties may vary. Moreover the bio-mimetic scaffold has also to adopt its nanostructure without harming the cells to be carried and implanted (Drury and Mooney, 2003). The 12- to 16-mer peptide class discovered by Zhang folds into double layered β -sheets to form nanofibers following a folding pathway similar to misfolding process of amyloid protein (Yokoi et al., 2005). In this self-assembling peptide class the process of assembling is triggered by external system conditions; indeed usually the formation of nano-structured scaffolds takes place at physiological conditions of pH and temperature. As a matter of fact, these pH-responsive self-assembling peptides properties make them particularly appealing for applications in nanomedicine (Davis et al., 2005). Numerous publications provided insights on this self-assembling peptide class and a wide variety of new biomaterials was then developed for *in vitro* and *in vivo* applications (Davis et al., 2006, Gelain et al., 2007a, Gambaretto et al., 2008, Semino, 2008). Additionally, functional motifs can be added by extending their primary self-assembling sequences. Rational modifications of the peptides sequence aim at directly controlling the peptide molecular aggregation within the fibril matrix and its bioactivity. Recent studies indicate that nanoscale features within a matrix influence cell adhesion, morphology and proliferation (Berry et al., 2004). Therefore, a wide range functionalized peptides (FPs) has been developed, adding a biological motif at the C-terminal of RADA16-I (Gelain et al., 2007a). A two glycines spacer (Gs) was placed between the RADA16-I sequence and the biological motif in order to confer a satisfactory exposure to cell membrane receptors. However, the “side effects” of this spacer over scaffold biological functionality and peptide self-assembling propensity has never been investigated. To better clarify this issue, we performed a

comprehensive set of measurements over self-assembling RADA16-I core peptides linked to functional motifs via glycine spacers of different lengths.

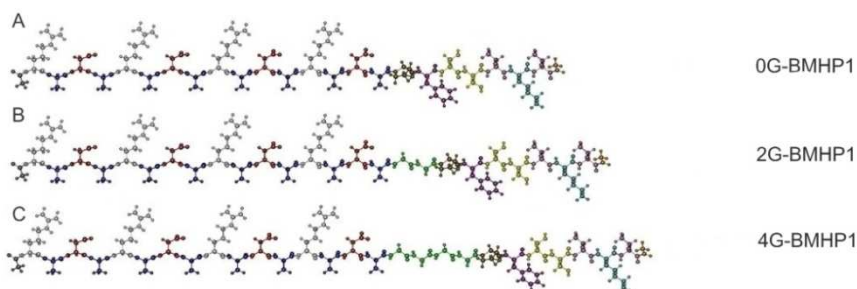


Fig. 10: The self-assembling peptides used in this study. (A) 0G-BMHP1, (B) 2G-BMHP1, (C) 4G-BMHP1. A spacer of two (B) or four glycines (C) (colored in green) was inserted between the self-assembling cores and the functional motif PFSSTKT.

2G-BMHP1 (GGPFSSKTK), a functionalized self-assembly peptide, stimulates neural stem cell adhesion proliferation and differentiation *in vitro* (Gelain et al., 2007a); we compared it with 0G-BMHP1 (PFSSTKT), lacking any Gs, 4G-BMHP1 (GGGGPFSSTKT), comprising a 4 long spacers, in order to assess the spacer's relevance over scaffold gelation and its biological influence over neural stem cells adhesion. We investigated the nanostructure of each peptide by atomic force microscopy AFM. To evaluate their process of self-assembly, Fourier transform infrared (FTIR) and Raman spectra of these peptides were collected at different pH conditions. Finally a thermal treatment via FTIR spectroscopy was performed on the peptides in solution in order to test their stability and their structural changes.

Our structural analysis suggests that the three peptides show a similar nanostructure, but the lack of Gly-spacer affects both the stability of the cross- β structure and a proper functional motif exposure. Neural stem cells (NSCs) adhesion experiments over our SAPeptides scaffolds confirmed the importance of long Gly-spacers to preserve the peptide bioactive functionality. The *in vitro* test confirmed our hypothesis and also strongly improved the biological functionalities of the biomaterials themselves. Our study shows how deepening our understanding in nanostructure assembly is crucial for this class of biomaterials in order to design new functionalized hydrogels tailored for the specific regenerative applications.

Thanks to our deep structural analysis we showed how an accurate structural investigation can lead up to a better understanding of new designing rules for new self-assembling peptides suited for specific applications. We tested four self-assembling peptides (Fig.10) with an identical functional motif (PFSSTKT) at the C-terminal of the RADA16-I peptide sequence used as a core capable of driving the

assembly process. The only difference among these peptides is the presence of two (2G-BMHP1) or four glycines (4G-BMHP1) between the RADA16-I sequence and the functional motif as depicted in Figure 1 (polar residues are green). Also a peptide lacking of glycines was synthesized (0G-BMHP1). The presence of side chains with minimal steric hindrances in glycines is likely to provide higher degrees of freedom to the overall molecules in comparison to those normally imposed by the radical groups of other aminoacids. Thus a glycines spacer (Gs) was used as a hinge between the two blocks of the peptide not to compromise the self-assembly of the RADA16-I part and the exposure of the biological motif to the environment. Nonetheless we tested a similarly functionalized peptide deprived of the Gs spacer (0G-BMHP1) to investigate the contribution of the Gs. Each peptide was dissolved in MilliQ solution, then PBS (pH=7.4) was added to test their propensity of forming hydrogel scaffolds at the macroscale. Each peptide formed a hydrogel upon exposure to the buffer.

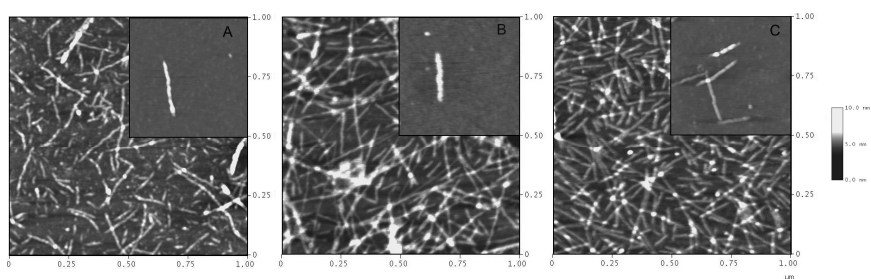


Figure 11: AFM images of FPs solutions at a concentration of 0.05% (w/v). 2G-BMHP1 (B) and 4G-BMHP1 (C) self-assemble into nanofibers (average width: ~15 nm). 0G-BMHP1 (A) self-organizes into nanofibers shorter than (B) and (C) but with approximately the same width. Inserts show high resolution images of single or few fibers of the same peptides at a concentration of 0.01% (w/v).

AFM measurements (in tapping mode) were performed to image the nanostructure of the self-assembling peptides. 0G-BMHP1, 2G-BMHP1 and 4G-BMHP1 formed nanofibers in MilliQ water with comparable dimensions as showed in Figure x. In particular the nanostructure of the peptides looks similar to the RADA16-I structure, in spite of an average nanofiber width (14.0 ± 1.4 nm) for 2G-BMHP1, a higher width for 4G-BMHP1 (14.2 ± 1.4 nm) and a lower width for 0G-BMHP1 (13.0 ± 1.6 nm). Peptide nanofibers are significantly wider than those of RADA16-I (9.4 ± 1.2 nm) (imaging data not shown), an expected finding given by the added functionalized tails flanking the self assembled cores. However, the experimental error ($\sim 10\%$) is of the same order of magnitude as the theoretical width difference among 0G-BMHP1, 2G-BMHP1 and 4G-BMHP1 making the measured width differences not significant.

Higher resolution measurements of the same peptides were taken via AFM tips with a smaller radius of curvature (2 nm) and confirmed the previous observations (see inserts). Thus, our AFM studies revealed that the nanostructure of each tested peptide is similar to that one of RADA16-I (Fig.11). It is plausible to assume that each peptide formed a cross- β structure when exposed to physiological pH. The only difference found was the length of the nanofibers: in fact Fig.11 evinces nanofibers formed by 0G-BMHP1 are shorter than those formed by 2G-BMHP1 and 4G-BMHP1. Our hypothesis is that the self-assembled nanostructure of 0G-BMHP1, lacking of Gs, as a result shows either higher stiffness and allows more closer electrostatic interactions between the added functional motif and the self-assembling core, thus respectively making its nanofibers less resistant to solvent stresses and interfering with the stability of the self-assembling cores.

We performed Raman and ATR/FTIR spectroscopy measurements to validate our hypothesis and to understand the direct contribution conferred by Gs to the stability of self-assembled nanostructure. FTIR spectroscopy of the peptide ensemble gave spectra comprising peaks with several absorption bands in the mid-infrared region. Among them we focused our attention on the Amide I band (from 1700 to 1600 cm^{-1}), precious indicator of the C=O stretching vibration sensitive to the peptide backbone conformation, thus giving information on protein secondary structures and intermolecular interactions. Moreover, the second derivative of the absorption spectrum was performed to better resolve the multiple spectral components overlapped in the Amide I region (Susi and Byler, 1986, Arrondo and Goni, 1999). Amide I region ATR/FTIR spectra of each peptide in each buffer condition are reproduced in Fig.12A while in figure 12B the relative second derivative spectra of the same region are shown. All peptides display two amide I components centered at $\sim 1618 \text{ cm}^{-1}$ and at $\sim 1696 \text{ cm}^{-1}$, typically observed in intermolecular anti-parallel β -sheet structures ((Javor et al., 2008) and references therein). A broad component around $1653\text{-}1649 \text{ cm}^{-1}$ was also found for each peptide in all conditions and assigned to random coil structures, in accordance with circular dichroism analysis (data not shown) (Baraldi and Tinti, 2008) and hydrogen/deuterium exchanges studied by FTIR (Arrondo and Goni, 1999) (see supplementary data for details). The most significant differences occurred in the second derivative spectra following pH displaces (buffer 3 and buffer 4).

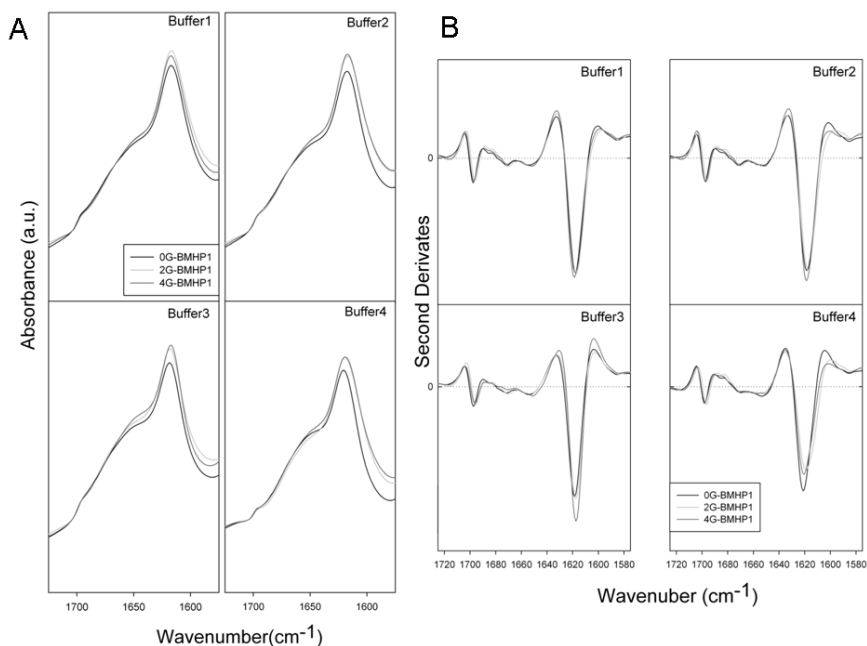


Fig.12. ATR/FTIR absorption spectra of self-assembling peptides. (A) ATR/FTIR absorption spectra of self-assembling peptides. (B) Second derivatives of ATR/FTIR spectra in different buffer conditions. Spectra show the intermolecular β -sheet band of the peptide folded structures ranging from 1618 cm^{-1} to 1696 cm^{-1} . The highest intensity of the β -sheet components is observed for 4G-BMHP1 in assembling conditions of buffer 3 (3B, buffer 3). 0G-BMHP1 displays an up shift of the 1618 cm^{-1} component in buffer 4 (3B, buffer 4), indicating a loosely packed assembly.

Indeed, among the tested peptides exposed to buffer 3 (assembling condition from pH 2 to pH 8), 4G-BMHP1 gave the highest $\sim 1618\text{ cm}^{-1}$ peak intensity indicating the highest amount of β -sheet structures. On the other hand, after re-suspending 0G-BMHP1 in buffer 4 we detected a 2 cm^{-1} peak shift towards higher wavenumbers of the $\sim 1618\text{ cm}^{-1}$ component. To assess the stability of the self-assembled molecular structures we performed a thermal treatment on each tested peptide (see methods for details) and on the RADA16-I here included as a positive control. Each peptide was dissolved in D_2O and incubated overnight at 4°C . The unfolding of the cross- β structure was then investigated by heating the sample at a linear rate of $0.2\text{ }^\circ\text{C}/\text{min}$. The cross- β structure band at 1618 cm^{-1} decreased as the temperature increased, as a consequence of the structure unfolding and/or of the increased structure dynamics that lead to hydrogen/deuterium (H/D) exchange. Therefore,

the 1618 cm^{-1} band variation gives hints of the overall stability of the assembled cross- β structures.

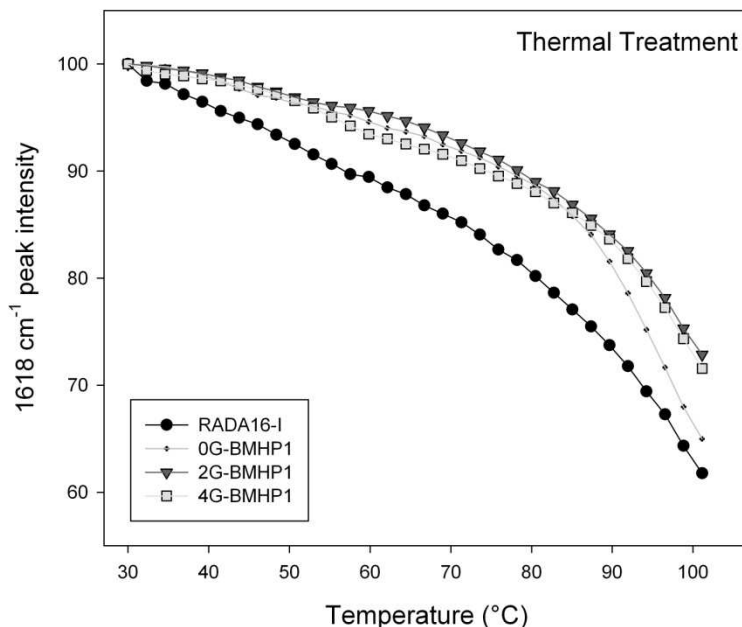


Fig.13: Thermal stability of the self-assembled peptides. Temperature dependence of the intermolecular β -sheet band intensity at 1618 cm^{-1} of the self-assembly peptides in D_2O solution, from $30\text{ }^\circ\text{C}$ to $100\text{ }^\circ\text{C}$. The FPs show a higher stability in comparison with RADA16-I. Noteworthy, 0G-BMHP1 at $100\text{ }^\circ\text{C}$ reduces its 1618 cm^{-1} peak intensity at $\sim 65\%$ similarly to RADA16-I, while 2G-BMHP1 and 4G-BMHP1 at the same temperature decrease to $\sim 74\%$. Standard deviation of the data from independent experiments is smaller than the symbol size.

In Fig.13 the 1618 cm^{-1} peak intensity is plotted as function of temperature. Even if RADA16-I self-assembled molecular structures look less stable than those of the functionalized peptides (its curve decreases appreciably faster than others and at the end of the thermal treatment approximately half of its β -sheet structures component is lost), the tested peptides maintained their cross- β structures up to $80\text{ }^\circ\text{C}$ and showed similar thermal unfolding profiles. At approximately $100\text{ }^\circ\text{C}$ 2G-BMHP1 and 4G-BMHP1 lost 28% of their initial β -sheet components, while 0G-BMHP1 decreased at a higher degree by losing 34% of its cross- β structure.

Therefore the presence or the absence of the chosen Gs spacers does not seem to prevent the cross- β structure formation in tested solvent conditions. Additionally our data let us infer how 0G-BMHP1

nanostructure is less stable than those of the other two peptides for two main reasons: i) when exposed to buffer 4 a shift of the 1618 cm^{-1} peak towards high wavenumbers presumably points out a relaxation of its β -sheet structure and ii) the thermal treatment indicates a lower stability of this peptide, which is the most sensitive to temperature increments.

Raman spectra of the hydrated films of the investigated materials in the $1600\text{-}1800\text{ cm}^{-1}$ range (Amide I region) and in the $2500\text{-}3100\text{ cm}^{-1}$ range are shown in Fig. 14A and 14B respectively. The region at lower energy, from 580 cm^{-1} to 1100 cm^{-1} (not shown in figure), contains the complex modes of proline ($\nu\text{C-N}$ and $\nu\text{C-C}$) at around $850\text{-}950\text{ cm}^{-1}$. This region is almost completely dominated by the second order phonon spectrum of the substrate (see methods for details) and it is not suitable for reliable analyses. Hints about the secondary structure of peptides can be obtained from the analysis of the amide I region from 1600 to 1700 cm^{-1} . Indeed, the peak conformation and a noticeable asymmetry of the amide I band suggest a distribution of secondary structures. An important peak component above 1700 cm^{-1} arises from C=O stretching from aspartic acids and is observed in the amide I band especially when the peptides (in particular 4G-BMHP1 and 2G-BMHP1) were in buffer 1 and buffer 4 conditions.

Buffer 4 induced significant changes in the shape of amide I region in 0G-BMHP1. In Fig. 14A the amide I peak of 0G-BMHP1 shows a broader shape than those obtained with the other peptides. Moreover, the amide I peak of 0G-BMHP1 shifted from 1675 (other buffers) to 1672 cm^{-1} (buffer 4). In Figure 4B the peak at 2090 cm^{-1} is due to the CH_2 stretching, while the peak at 3060 cm^{-1} is ascribable to CH_2 stretching in the aromatic ring (De Gelder et al., 2007). Therefore, the latter mode is a sensible probe of the status of phenylalanine, containing the sole aromatic ring in the peptide molecules located within the added functional motifs. The analysis of this region can provide useful indications for understanding the folding of the added functional tails. Noteworthy, another phenylalanine phonon mode previously assigned to ring breathing is observed at 1003 cm^{-1} (De Gelder et al., 2007) but its partial overlapping with the substrate spectrum compelled us to consider it as insufficiently reliable. In Fig. 14B only 4G-BMHP1 shows a relevant spectral modification related to the buffer conditions. In fact the intensity ratio between peaks at 2090 and 3060 cm^{-1} is completely interchanged passing from buffer 2 or 3 (i.e. favoring self-assembling) to respectively buffer 1 or 4. The drastic effect on the functional motif in 4G-BMHP1 evinces a larger mobility of the functional motif that makes it more sensitive to the solvent conditions.

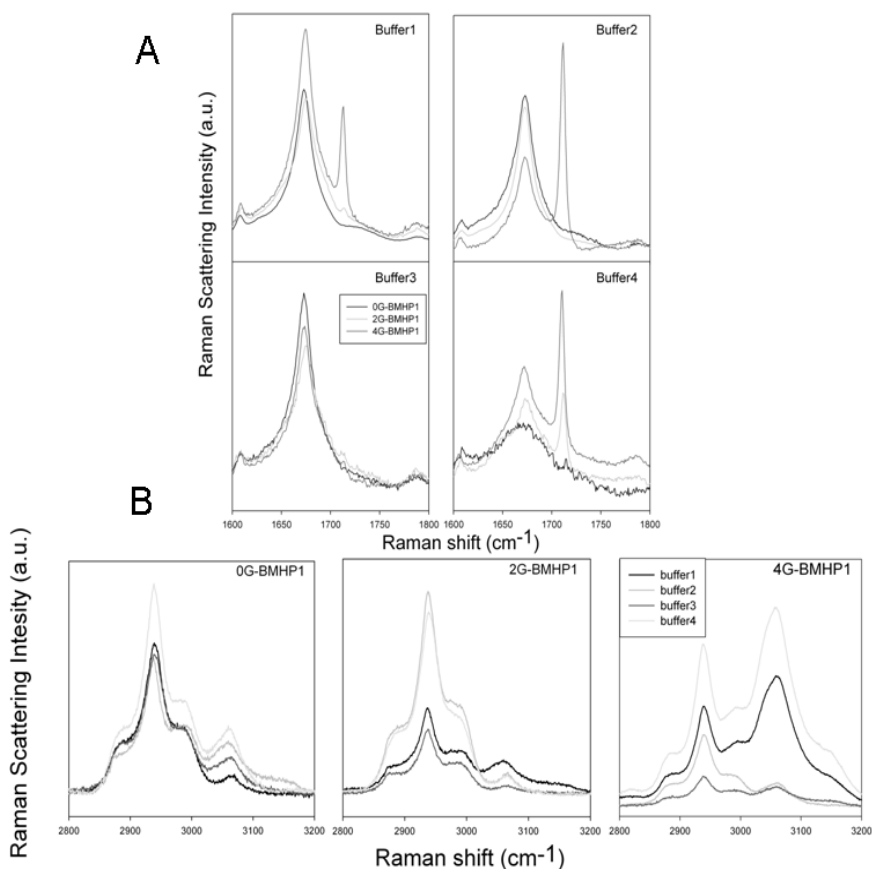


Fig.14: Raman Spectra of tested self-assembling peptides. (A) Raman Spectra (1600-1800 cm^{-1} region) of the tested self-assembling peptides. Each spectrum shows the peptide Amide I region in all buffered solutions. In buffer1, buffer2 and buffer3, each peptide shows a similar conformation of Amide I peak, suggesting a similar β -sheet conformation of the peptide centered in 1675 cm^{-1} . In buffer4 the pH shift alters the self-assembled structure of 0G-BMHP1 thus affecting the shape of its Amide I peak and suggesting a wider unordered component. (B) Raman Spectra of 2500-3100 cm^{-1} region of the tested self-assembling peptides (region of νCH_2) exposed to different buffers. The change in the relative intensity between the peak at $\sim 2940 \text{ cm}^{-1}$ (νCH_2) and the peak at $\sim 3061 \text{ cm}^{-1}$ (νCH_2 of Phe aromatic ring) can be appreciated in case of peptide 4G-BMHP1

Raman results just showed provide three main indications confirming our model: i) the analysis of the amide I mode shows that the total lack of the Gly spacer (data of BMHP1-L) affects the stability of the cross β -structure, in agreement with ATR-FTIR results; on the other hand, ii) no relevant effect is observed in this region as a function of the spacer; iii)

the analysis of the aromatic CH₂ modes evinces that longer Gly spacers make the bioactive motifs sensibly more exposed to the solvent.

To verify this hypothesis we tested the different materials directly with neural stem cells.

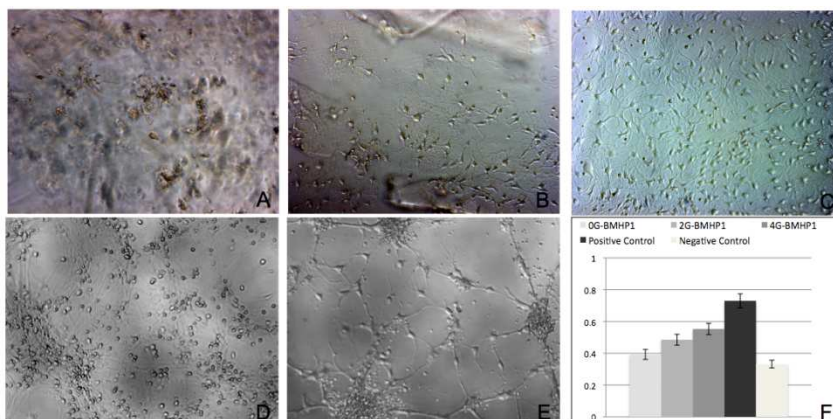


Fig.15: Phase contrast images of differentiating neural stem cells (7 days *in vitro*) over scaffolds composed of tested self-assembling peptides. (A) 0G-BMHP1, (B) 2G-BMHP1, (C) 4G-BMHP1 SApeptides. (D) Positive and (E) negative controls. 4G-BMHP1 coaxes NSCs to differentiate and survive most effectively while, in case of 0G-BMHP1, small clusters of poorly adhered NSCs testify a possible poor availability of the BMHP1 functional motif for cell membrane receptor binding and consequently cell differentiation pathways activation. Additionally, the “sinking” of NSCs within the assembled scaffold of 0G-BMHP1 (A) testifies a possible lower mechanical stiffness insufficient to bear the weight of NSCs seeded over the top surface of the substrate. CellTiter results (G) shows significant differences for all possible coupled experimental groups ($p > 95\%$) except for 0G-BMHP1 and negative control, 2G-BMHP1 and 4G-BMHP1, and positive control. Values are reported as means \pm standard error of the mean.

We adopted our well-established *in vitro* protocol (Gelain et al., 2007b) to evaluate differences, if any, occurred in NSC adhesion depending on the functionalized peptide substrate used. Negative control (untreated wells) and positive controls (Cultrex) were used. One week after seeding NSC proliferated and adhered as expected with 2G-BMHP1 (Figure 6B), less intensively in case of 0G-BMHP1 (Fig.6A), i.e. with isolated clusters of poorly branched cells, and remarkably more for 4G-BMHP1 (Fig.6C) where an almost confluent monolayer of branched differentiating cells was formed. Quantification of NSC proliferation and survival confirmed these observations by showing remarkable differences between FPs with longer spacers and negative controls. On the other hand the absence of any Gly spacer between the self-assembling sequence and the functional motifs seems to impair the biotactivity of the latter (no significant difference of absorbance values between 0G-BMHP1 and negative control). The structural findings are

in agreement with the NSC results *in vitro*. In fact this is clearly visible in Fig.15C, showing the direct application of these peptides as cell cultures scaffolds. 0G-BMHP1 fails to favour NSC proliferation and adhesion and, at the same time, the cells fall in the hydrogel scaffold suggesting that the nanostructured substrate biomechanical stiffness is insufficient for supporting seeded cells. This finding is in accordance with AFM results showing nanofibers with different lengths in the case of 0G-BMHP1. Nonetheless, while 4G-BMHP1 carries out its structural role exactly as 2G-BMHP1 it is also more effective in the NSC adhesion thanks to a better exposure of its functional motif.

This study describes an ensemble of approaches useful to investigate the self-assembled structures of peptides derived from the functionalization of RADA16-I. It elucidates not only how the functionalized peptides are more stable than RADA16-I in respect to temperature and pH variations, but that the insertion of longer glycines spacers between the self-assembling cores and the functional motifs improve the outcome of the functionalization of SApeptides, thus providing better tools for *in vitro* studies in cell biology and for applications in regenerative medicine therapies.

5.1.3 Further investigations about hydrophobic component in nanostructure stabilization

The aggregation of proteins and peptides *in vivo* plays a fundamental role in the onset of several human pathologies known as amyloid diseases (Kelly, 1998, Dobson, 2000). Despite the lack of significant sequence homology among the proteins involved in these diseases, amyloid fibrils seem to share a common structural motif, namely the cross- β -pleated sheet (Kirschner et al., 1986). The mechanisms responsible for fibril formation have been extensively investigated but they are still poorly understood, which makes it difficult to develop new drugs against these diseases and even to select suitable targets. Recent studies indicate that early aggregates and fibrils have a great contribution of hydrophobic interactions, whereas late amyloid fibrils are more stabilized by hydrogen bonds (Foguel et al., 2003, Cordeiro et al., 2004). However, the hydrophobic effect is considered to be the major driving force for the folding of globular proteins. The thermodynamic factors which give rise to the hydrophobic effect are complex and still incompletely understood. The free energy of transfer of a non-polar compound from some reference state, such as an organic solution, into water, ΔG_{tr} , is made up of an enthalpy, ΔH , and entropy, $-T\Delta S$, term.

$$\Delta G_{tr} = \Delta H_{tr} - T\Delta S_{tr}$$

Hydrophobic interactions are widely believed to be of dominating importance for protein structure, aggregation, and function. However, the molecular theories of hydrophobic interactions have not been used so far in molecular studies of protein structure. This is partly because these theories have limitations that are still being clarified and partly because of their complexity.

In this chapter some theoretical experiments will be showed, in order to describe the importance of hydrophobic compound for the process of self-assembly in the SApeptides already proposed in the last chapters: BMHP1, ALK and SDE.

A series of 10 short MD simulations (100ps at 300K) were run starting from the cross- β structure proposed by Park et al. (Park et al., 2006), with the RADA16-I part arranged to form an antiparallel β -sheet bilayer. During MD, the three filaments exhibited different conformational behaviors of the functionalized tail. In the Fig.16 is clear that the biological tag form different pattern of aggregation: BMHP1 form little cluster (formed by some fibers), SDE do not form any kind of cluster, while ALK seems to form large cluster of aggregate functional tail. In order to deeply investigate about this behavior that seems to be depending on the aminoacidic sequence a longer fiber was built. The fiber had the same structure but is composed by 100 molecules and only an half longitudinal section was considered, in order to simplify the system and to reduce the timescale (Fig.17).

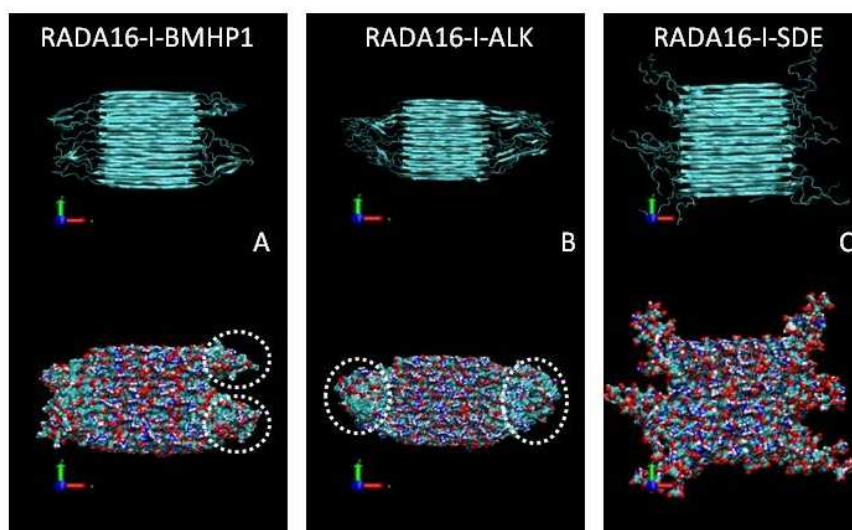


Fig.16. Final conformations of initially imposed β -sheet bilayer structures (15

molecules on each side) after 100ps MD simulations. A) BMHP1, B) ALK and C) SDE. Cluster formed by aggregated biological tail are pointed out by dash circles.

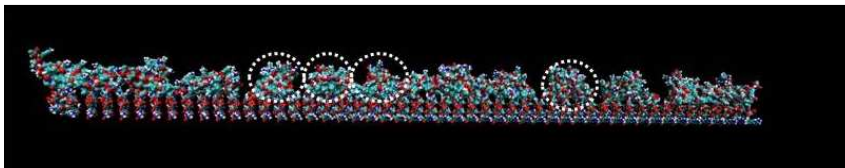


Fig.17. Final conformations of initially imposed β -sheet bilayer structures of BMHP1 (50 molecules on each side) after 1ns MD simulations. Cluster formed by aggregated biological tail are pointed out by dash circles.

100 MD simulations 1ns long were performed for each peptide. At the end number of cluster were counted using a cutoff distance of 7Å. The Fig.18A shows the results of sampling. Is it possible to mark that BMHP1 form significantly more cluster than ALK; SDE is not showed because applying the same counting algorithm it did not form any kind of aggregation. The hypothesis (summarized in Fig.18B) is that the size of cluster is depending on the level of hydrophobicity of the biological added tail. In fact the more hydrophilic peptide (SDE) did not form any kind of aggregation while the more hydrophobic one (ALK) form larger cluster. Further analysis will require verifying this hypothesis. If it will be confirmed the formed cluster could be a way to classify the self-assembling functionalized peptide and moreover to predict the possibility of the assembling.

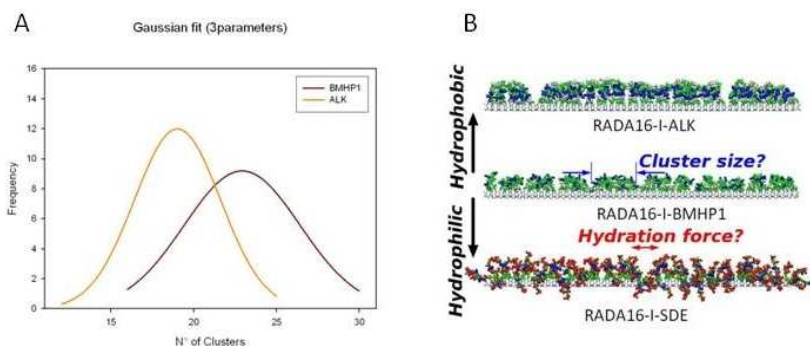


Fig.18.A) Number of cluster formed by BMHP1 and ALK. The data are fit by a 3parameters Gaussian. B) Hypothesis of cluster dimension in comparison to hydrophobic force.

5.2 Example of biomaterial application *in vivo*

5.2.1 Electrospun micro and nano-fiber tubes for functional nervous regeneration in sciatic nerve transaction

Following nerve injury, axonal elongation may occur by spontaneous regenerative capacity of the peripheral nervous system (Fu and Gordon, 1997). However, random nervous sprouting fails to regenerate complete transections where extensive loss of tissue is involved. In the case of transected nerves, the regenerative process can be enhanced by suturing the two nerve stumps or, if any nerve tissue has been lost, by surgically bridging the gap with either tissue from a donor (autograft or allograft) or with a synthetic conduit. However, a major drawback of autografts is that they partially denervate the donor site to reinnervate the injury site. A tubular conduit, acting as a physical guide fabricated from degradable or non-degradable polymers for the regenerating nerve, can guide and facilitate peripheral nerve regeneration. A variety of conduits have been produced for bridging nerve gaps where both synthetic and natural materials have been used. Literature shows that materials with the highest regenerative activity are collagen and synthetic biodegradable copolymers of poly(DL-lactide-co-glycolide) and poly(ϵ -caprolactone) (Yannas, 2001, Yannas and Hill, 2004).

A novel electrospun biodegradable micro- and nanofiber scaffold was developed by electrospinning solutions of PCL and PCL/PLGA (Fig. 19A, B). Fibers ranged in diameter from ~ 280 nm to $8 \mu\text{m}$ (see methods for details). A fibrous structure was preferred over stiff continuous tubes to obtain nerve guides with high flexibility, high porosity, high surface/volume ratio favouring protein adsorption and fibrous structures easy to be sutured to the sciatic nerve stumps (fig. 19D). The fibrous micro-structure of PCL/PLGA provides mechanical stability to soft tissues, while the nanostructure adds more substrate surface for cell attachment (and therefore a higher cell density per unit of space) compared with other structures and guarantees a high-permeability of the guide walls to allow for nutrient exchange. SEM analysis of the PCL/PLGA guides showed pores with variable dimensions but uniformly distributed on the longitudinal and cross-sections with small pores (700 nm) and large pores ($20 \mu\text{m}$).

At four months after surgery the nerve tube was still present in every examined animal: neither septic collections nor tube breakages were found in the surgical field. Formation of a thin fibrous tissue capsule external to the nerve guide conduit walls was observed and macroscopically no inflammatory response was noticed in any of the treated animals, indicating good tissue response to the synthetic conduit.

Tubular conduits collapsed in 16 (40%) of the treated rats due to prosthesis displacement and subsequent muscle compression exerted during the pacing of the rat. Collapsed tubes have not been considered in the following results.

In all rats of group 1 (transected sciatic nerve, Fig.19C) and group 2 (10-mm nerve gap left between the transected stumps) nervous tissue did not reconnect the two stumps of transected sciatic nerves and neural sprouting following injury did not show any significant difference between the two experimental groups. Hence group 1 and 2 are considered together and named as the control group hereafter. A spontaneous and random neural sprouting occurred from proximal stumps: however, nervous fibers targeted muscles located near the lesion site and the reconnection of the distal nerve segment was negligible. Distal nerve stumps in the control group showed macroscopic atrophy and neural degeneration (data not shown).

The flexible fibrous structure of the conduit we tested in this study (composed of PCL/PLGA degradable polymers) makes it easy to suture to the proximal and distal ends of the nerve stumps and to adapt it to the living systems. It has a porous structure, thus making it permeable to the entry of nutrients into the conduit lumen to promote the nerve regeneration. At the same time, the conduit has the necessary barrier to prevent the infiltration of unwanted tissues into the conduit from outside, as no ectopic tissues were seen in the cross section of the nerve regenerated in the inner lumen of the conduits. The developed conduit has no problem of tube breakage that is often encountered with other types of solid polymer conduits, and can easily be filled with physiologic solution or gel-like fillers like collagen and fibrin glue.

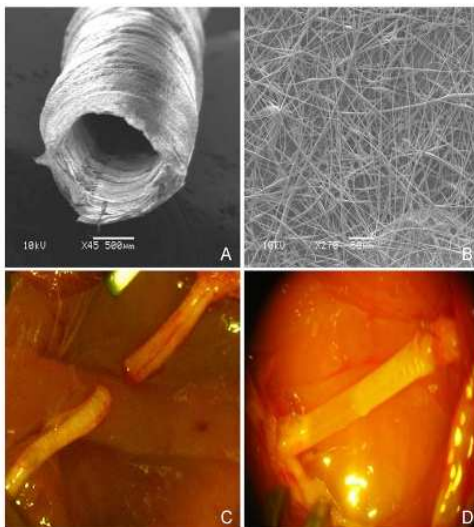


Fig.19. Experimental model. (A) SEM images of the electrospun PCL/PLGA nerve guide conduit and (B) magnified details of the tube wall: microfibers and nanofibers range in diameter from ~ 280 nm to 8 μ m. The non-woven fibrous microstructure is characterized by small pores (700 nm) and large pores (20 μ m). (C) Micrograph of sham-operated rat sciatic nerve (experimental group 1). (D) Micrograph of prosthesis implanted, filled with saline solution and sutured to the transected nerve (experimental group 3).

One advantage of electrospinning is that it does not involve heating or chemical reactions during tube synthesis. Thus, a material that is not stable to heat or chemicals, and cannot be processed by other methods, can be processed by electrospinning into microfibrinous or nanofibrinous form. No significant cavities or cysts have been detected in the regenerated tissue. Most of the regenerated tissue grown inside the guide channels was positive to Bielschowsky staining (Fig.20B) and to anti β -tubulin antibody (Fig.20C). Occasionally, nervous regeneration from the proximal nerve stump was detected on the prosthesis outer edge walls concomitantly with inner lumen regeneration: in that case, Bielschowsky and β -tubulin positive fibers infiltrated and crossed the tube wall outward and vice-versa. When outer nervous regeneration was absent, tube walls were infiltrated with fibrotic tissue only.

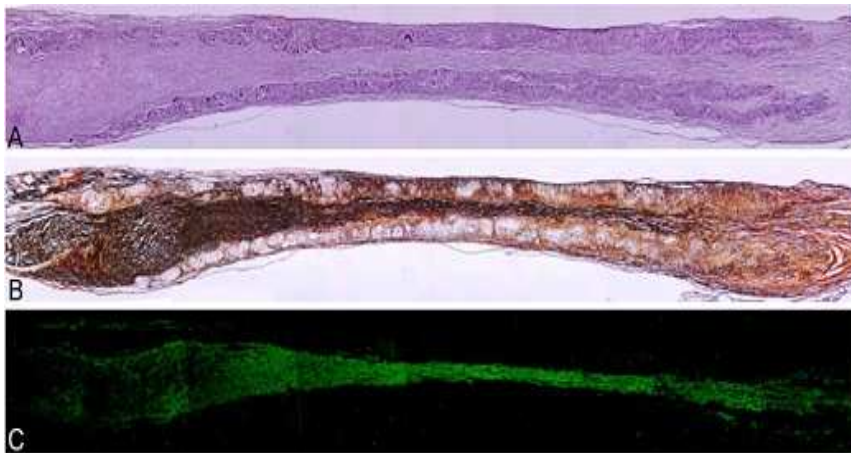


Fig.20. Longitudinal sections of nerve regenerated within the implanted guide channel. In the conduit, the regenerated nerve bridged the 10-mm gap, reconnecting the two sciatic nerve stumps. (A) 4 months after surgery hematoxylin-eosin staining shows the presence of regenerated tissue filling the conduit lumen; decreased lumen diameter is observable at middle length of the guidance channel. Regenerated tissue positive to Bielschowsky staining (B) and to anti β -tubulin antibody (C) shows nervous projections oriented along the major axis of the prosthesis bridging the 10-mm gap between the severed sciatic nerve stumps (image sequence collected at 4x magnification).

In order to quantify nervous regeneration, image analysis was performed on sciatic nerve transversal sections of 12 treated rats. Images acquired were processed to quantify the nervous regenerated area at specific equally spaced distances from the proximal stumps named as percentage distances over the total gap length (Fig.21A). Measurements of the cross-sectional area positive to Bielschowsky staining, anti β -tubulin and anti neurofilament NF200 antibody show similar values. Positive areas reveal nervous regeneration throughout the conduit length. Values show a minimum at approximately the

middle conduit length. It is noteworthy that the proposed channels showed a lumen shrinking near the mid-point of the 10-mm gaps (fig. 21B, C); this phenomena is jointly triggered by cellular infiltration within tube walls (thickening effect) and by muscle compression exerted during the pacing (compression effect).

Fibers positive to Fluororuby, a neural tracer injected proximally to the implanted prosthesis (see methods for details), were identified in all treated rats receiving the injections both at proximal and distal stumps, and concomitantly to the nervous regenerated areas (Fig.22A, B). No neural tracer-positive fibers have been found distally to the injuries in control groups.

CD68 staining of the regenerated tissue within the inner lumen of the electrospun scaffolds, identifying both macrophage and pluri-nucleated foreign body giant cells (Doussis et al., 1992, Al-Saffar et al., 1997)infiltration, was comparable in distribution and amount to that of healthy nerves (data not shown). On the other end, pluri-nucleated CD68 positive cells were detected within the tube walls, indicating a chronic foreign body reaction to the implanted tubular guides.

Myelinated axons were noticed throughout the tissue regenerated inside the conduits. Confocal images of the nervous area inside the conduit revealed noteworthy distribution of regenerated myelinated fascicles (MBP, CNPase, β -tubulin staining) at three quarters of the regenerated gap lengths (fig. 22C-F), as well as at the distal nerve stumps.

Collagen IV, one of the main components of the basal lamina in nervous tissue, was found in noticeable amounts and evenly distributed throughout the implant lumens in treated animals. However, its spatial organization (fig. 22H) was not as well organized as in healthy nerves (fig. 22G). The spatial disorganization of the regenerated tissue is further highlighted by a higher density of DAPI positive cell nuclei (Fig. 22B-K) respect to the healthy nerves (data not shown): this is consistent with the loss of cytoarchitecture and proper cell three dimensional distribution in the regenerated tissue. A low density of fibroblasts was found in the conduit lumen four months after surgery, although higher fibroblast concentrations were detected both nearby and within the conduit inner walls (Fig.22I-K). Functional reconnection of the severed nerve stumps has been unequivocally demonstrated by the following results: the presence of the neural tracer Fluororuby located both within and distally to the regenerated nervous tissue and the presence of muscular action potentials at the target muscles in 24 (70.6%) of the treated rats following electrode stimulations proximally to the regenerated gaps. It should be noted that the aforementioned functional recovery is still not satisfactory because of the lower nerve conduction rate, the bigger F-peak latency and the smaller amplitude of the detected cMAP respect to the contralateral nerve.

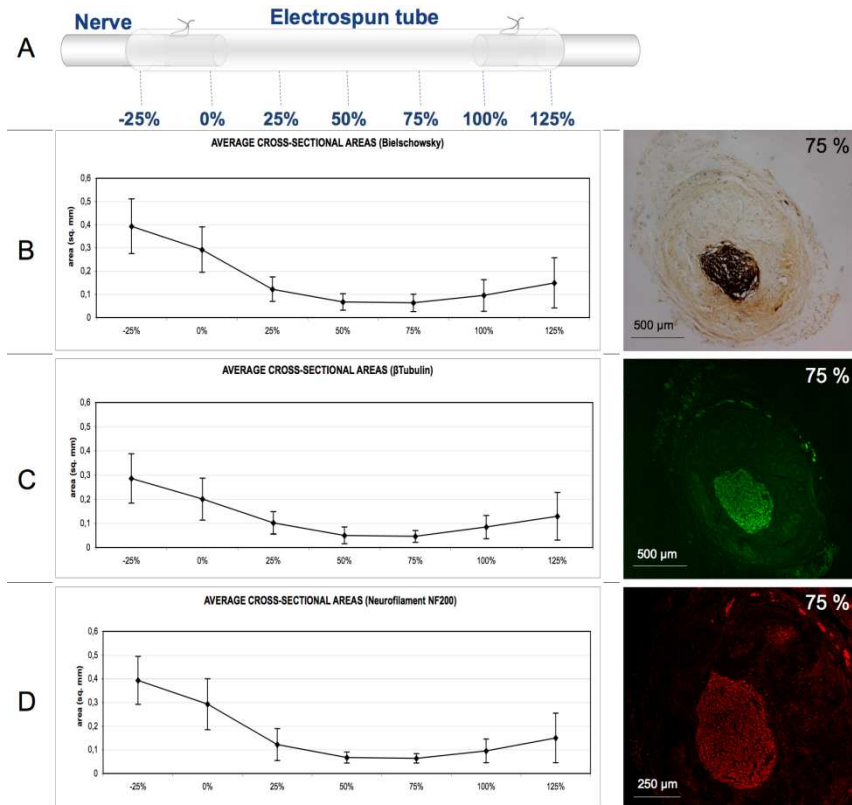


Fig.20. Morphometrical analysis of nervous regenerated area. (A) Scheme of the arbitrary coordinates representing the distance from the proximal side as a percentage of the total conduit length adopted to localize the estimated nervous regenerated cross-section. Cross-sectional area measurements positive to Bielschowsky reaction (B), to anti β -tubulin antibody (C) and to anti NF200 antibody (D) stainings are comparable and reveal regeneration throughout the conduit lengths. Images of regenerated area positive for the aforementioned stainings detected at 75% of the conduit length are shown on the right side of each graphic. Values for the regenerated area decrease at the middle length of the conduit. Area quantification is indicated in square mm. Error bars represent standard deviation ($N = 12$).

Our results let us infer a relatively early phase of nerve fiber regeneration and myelin repair following lesions: it is likely that a longer experimental frame would have displayed a more extensive remyelination and a higher nerve conduction velocity to the distal nerve. The sensory recovery outcome obtained with the Von-Frey test corroborates the results obtained with neural tracers and cAMP detection tests. However, sensory recovery will probably need a more deep investigation especially within the first weeks after treatment because of the intrinsic variability of the test, which has previously been demonstrated (Pitcher et al., 1999) and the reduced number of animals

analyzed, as a consequence of autophagy in both control and treated groups. Nevertheless, the trend of the treated group approaching the contralateral healthy nerves threshold is a good evidence of reinnervation. In addition, our work, making use of a standard rat sciatic nerve transection model and widely adopted evaluation techniques, can be compared with results published by other groups, testing nervous guides like silicon tubes or other biomaterials and fillers, by applying the widely accepted normalization theory developed by Yannas and co-workers (Yannas, 2001, Yannas et al., 2007). Indeed, in the case of silicon guides the percent of nerves fitted with a nerve guide that are bridged by myelinated axons decreases below 100% at approximately 7 mm while drops below 50% (critical axon elongation) at 9.7 ± 1.8 mm. This same parameter is unquestionably higher with our electrospun nerve guides because in all (100%) open tubes we found nervous regeneration and myelinated fibers reconnecting the 10-mm nerve gaps. Thus a more regenerative potential of our scaffolds compared to silicon tubes can be postulated.

While the multi-scaled structure of these nerve guides proved itself to be an useful improvement which makes jointly use of the advantages arising from both electrospun microfiber and nanofiber tubular scaffolds, further enhancements to the proposed scaffold can be adopted in the near future by modifying the electro-spinning proposed methodology in order to obtain nanofibers aligned along the longitudinal axis of the nerve guides while adopting a randomly oriented or, even better, a microbraided (Bini et al., 2004) micro structure, necessary to preserve the scaffolds mechanical properties. Indeed other works demonstrated that aligned electrospun fibers promote human Schwann cell maturation (Chew et al., 2008) and that nervous regeneration could be significantly enhanced with micropatterned conduits (Rutkowski et al., 2004) and scaffolds comprising oriented mats (King et al., 2003).

Moreover, the efficacy of our nerve guides can be improved by means of polymer functionalization (Kasemo, 2002), controlled release of growth factors, such as nerve growth factor (NGF), and/or other biological cues, such as Schwann cells or neural stem cells that can be introduced along the graft to promote and guide regeneration of peripheral axons in rats (Guenard et al., 1992, Paino et al., 1994, Bryan et al., 2000, Hadlock et al., 2000, Rodriguez et al., 2000).

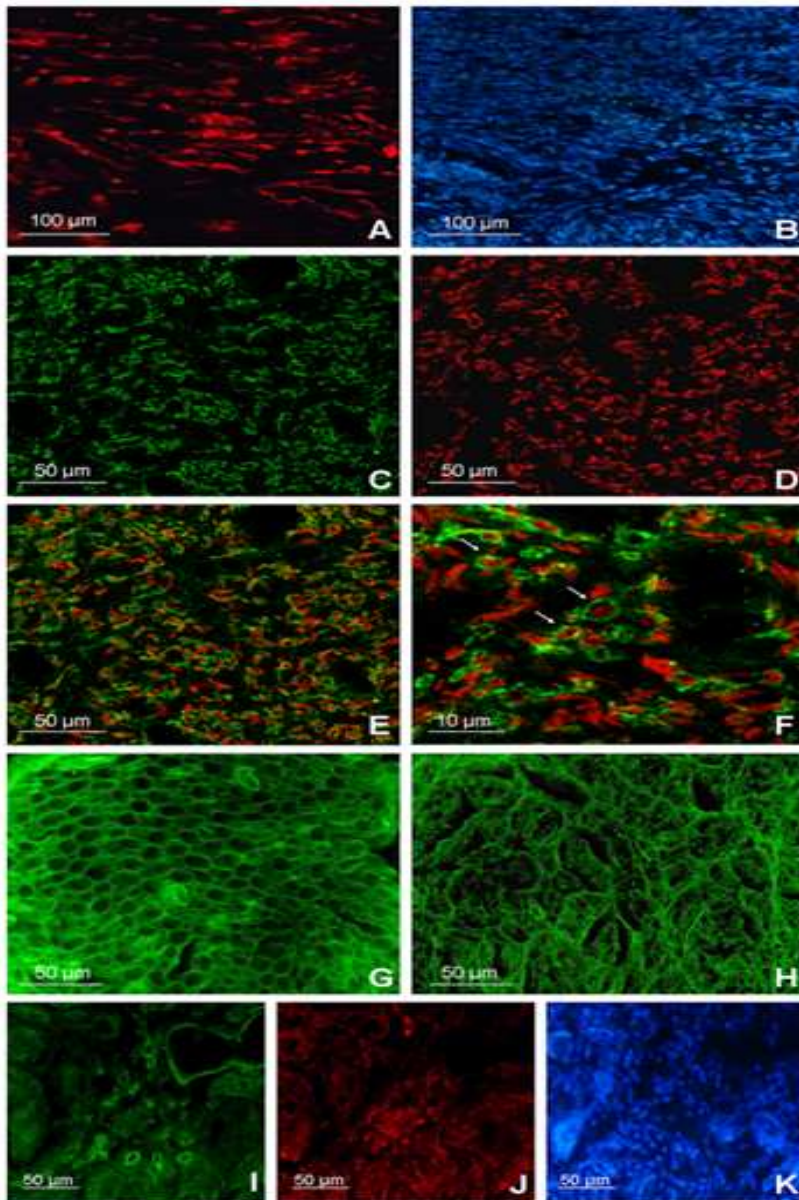


Fig.22. Immunofluorescence analysis. (A) Fluorescence imaging of a longitudinal section located distally to the implants shows cells positive to Fluororuby, a neural tracer injected proximally to the implanted prosthesis. Positive cells for the neural tracer in the nervous regenerated area were identified in all rats receiving the Fluororuby injection. (B) DAPI cell nuclei staining of the neuronal tracer positive area. Confocal cross-section image (75% of the conduit length) of myelin sheets, stained with MBP and CNPase (C), wrapping regenerated axons positive to β -tubulin staining. (D) Myelinated axons were noticed throughout the tissue regenerated inside the conduits. (E) Confocal merge image shows distribution of both myelinated and unmyelinated axons in the nervous area regenerated in the conduit lumen. (F) High magnification

confocal image, arrows indicate myelinated axons. Cross-section immunostainings for collagen IV in healthy sciatic nerves (G) and in regenerated tissues (H) show a noticeable amount of basement membrane component distributed throughout the prosthesis lumens of all the treated rats but with a remarkably different microstructure organization. Collagen IV is also detected both nearby and within the conduit inner walls (I) where low fibroblast density (J) is observable: same field DAPI cell nuclei staining (K).

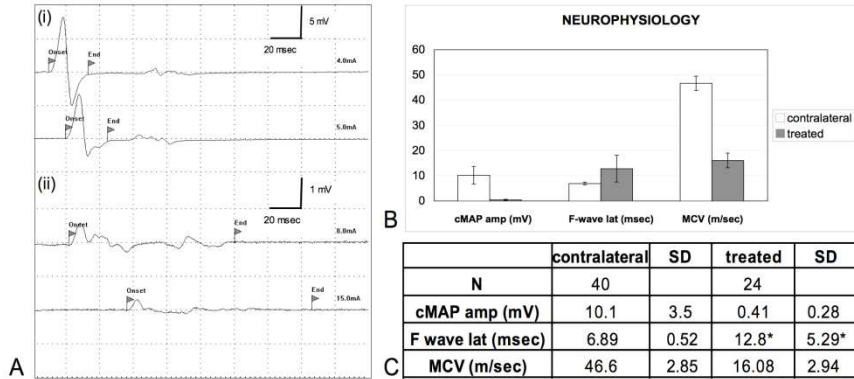


Fig.23. Neurophysiological results. No cMAP were recorded in both control group rats and in animals with collapsed prostheses. (Ai, Aii) The presence of the cMAP at the plantar muscles following sciatic nerve stimulation proximally to the implants was recorded in 24 of the treated rats. (B), (C) Mean cMAP amplitude as well as mean MCV (motor conduction velocity) are both significantly lower in the treated nerves in comparison with healthy contralateral nerves ($p < 0.0001$) showing a relatively early phase of nerve fibres regeneration and myelin repair after lesion. F-wave was recorded in 14 of the treated rats. (*) When detected in regenerated nerves, mean F-wave latency values are higher than in contralateral nerves.

6 WORK IN PROGRESS

From the collaboration with the Molecular Foundry of Lawrence Berkeley National Laboratory of Berkeley (CA, USA) we starting to develop a coarse-grained method to investigate about the aggregation process using a Virtual Move Monte Carlo algorithm (see methods for details).

We want to mimic a simple “tube” model developed from Hoang et al (Hoang et al., 2004) and applied to study the protein folding with great results. In this model the protein/peptide backbone is modeled as a chain of C_{α} atoms (Fig.24).

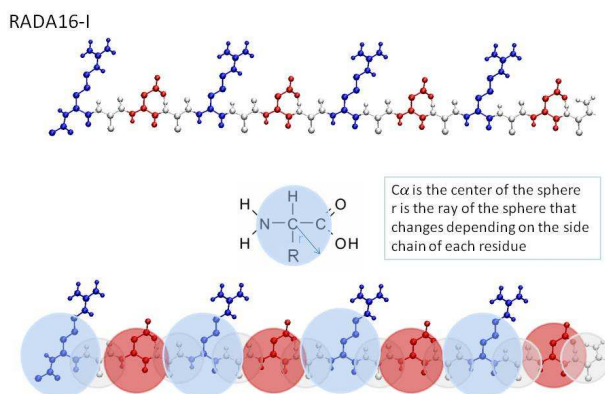


Fig.24. Scheme of tube model geometry applied to RADA16-I

Our idea is to switch this tube model adapting to RADA16-I and then to the functionalized peptide in order to investigate about the kinetics of aggregation. We want use a Coarse-Grained model in order to extend our computational characterization also at a timescale more comparable to the experimental timescale.

All the forces are parameterized as pairwise interactions. All bonds are characterized by a constant k of stretching, bending and rotational constant that for simplify the model are set as the same value.

The rigidity of the tube-peptide depends on the value of k (Fig.25). Studies in progress will use this model to validate the reasonable value of flexibility of the peptide chain. When all the parameterization of the self-assembling peptide system will be completed, this method will be applied to study the aggregation process of the SApeptides.

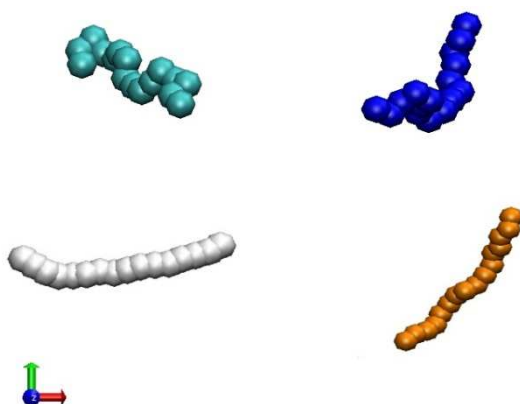


Fig.25. Variation of K value A) $k=5$, B) $k=10$, C) $k=20$ and D) $k=40$.

The usage of application of coarse grained approaches to study the wide class of self-assembling peptides (SAP) is increasing in these few years. The interest of the self-assembling peptides is due to the direct applications of these building blocks to nanotechnology and nanomedicine.

These peptides form extended β -sheet structures in physiological conditions similarly to amyloid fibrils formation. Considering these peptides importance and promise more efforts are due to understand the process of aggregation in order to unveil the fine details of the assembling process by which peptides aggregate in well-ordered structure.

The development of a coarse grained method for self assembling peptides forming fibers could be a new tool to design new materials with many different applications. Moreover the large characterization and analysis data of these nanostructures that we performed in the past years is a precious starting point for model validation and force field parameterization refinements. Great achievements in this field are improving the predictivity and also transferability of coarse grained methods to self assembling biopolymers, and the use of virtual move Monte Carlo method could be a promising way to accomplish to these aims. The goal of this project is principally the setup and testing of a CG method suited for studying the self-assembling phenomena and to identify how hydrophobic/hydrophilic residues mutations may alter the kinetics of superstructure formation and the self-assembled structure itself

7 CONCLUSIONS

The development of nanotechnology provides opportunities to characterize manipulate and organize matter systematically at the nanometer scale. Biomaterials with nano-scale organizations have been used as artificial matrices for tissue engineering. Traditional tissue-engineering scaffolds were based on hydrolytically degradable macroporous materials; current approaches emphasize the control over cell behaviors and tissue formation by nano-scale topography that closely mimics the natural extracellular matrix (ECM). The understanding that the natural ECM is a multifunctional nanocomposite motivated researchers to develop nanofibrous scaffolds through electrospinning or self-assembly. A biomaterial, both the drug-delivery vehicles and tissue-engineering scaffolds need to be biocompatible and biodegradable. The biological functions of encapsulated drugs and cells can be dramatically enhanced by designing biomaterials with controlled organizations at the nanometer scale. Commonly used scaffolds include synthetic biodegradable porous polymers or natural materials in the form of sponge, fibers or hydrogels, serving as the required 3D support for cell growth, differentiation and organization. The great feature of synthetic scaffolds is the potentiality to control their properties, while natural scaffolds are more efficient at fostering cell adherence.

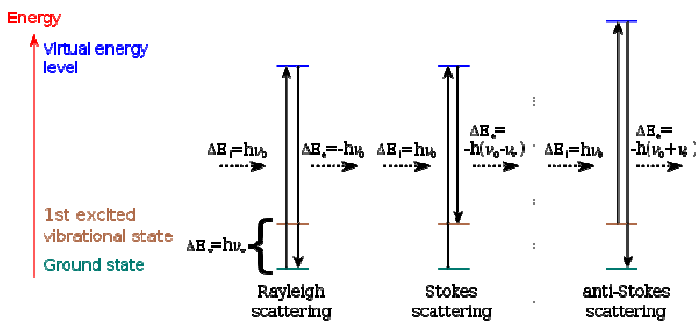
In this field peptide-based nanostructures are a great promise if we improve our knowledge of the mechanisms and physic-chemical determinants of peptide self-assembly. The achievements are that the self-assembled peptide structures with different modifications or decorations turn into useful products for the specific applications. In this context, obtaining full and rational control of the final spatial organization of aggregating peptides at the nanoscale starting from the sequence is the key challenge. Being able to realize tailored structures with remarkable properties, as RADA16-BMHP1, is highly attractive for future technological applications. The control and understanding of the sequence/structure properties relationships of these macromolecular systems will be crucial to take the necessary steps towards full exploitation of the potential of peptide self-assembly.

In this thesis computational and experimental ways of investigation were shown. It was possible to provide a methodology of self-assembling peptide study starting from computational and theoretical methods with the limitation of time and length scale. Except that thing, the computational results were successfully compared with experimental measurements. Spectroscopic techniques were applied for the first time to these kinds of biomaterials displaying new methodology

to investigation about the nanostructures. Moreover the investigation strategies at nanoscopic level showed how is possible to modify self-assembling peptides in order to amplify its features for a direct applications. Many other studies are in progress right now, and will bring to an enhancement of the knowledge about this interesting process of self-assembling in order to create new biomaterials for many applications.

8 APPENDIX

Raman scattering or the **Raman** is the inelastic scattering of a photon. That's mean that when light is scattered from an atom or molecule, most photons are elastically scattered (Rayleigh scattering). The scattered photons have the same energy (frequency) and wavelength as the incident photons. However, a small fraction of the scattered light (approximately 1 in 10 million photons) is scattered by an excitation, with the scattered photons having a frequency different from, and usually lower than, the frequency of the incident photons.



The different possibilities of visual light scattering: Rayleigh scattering (no Raman effect), Stokes scattering (molecule absorbs energy) and anti-Stokes scattering (molecule loses energy)

The interaction of light with matter in a linear regime allows the absorption or simultaneous emission of light precisely matching the difference in energy levels of the interacting electrons.

The Raman effect corresponds, in perturbation theory, to the absorption and subsequent emission of a photon via an intermediate electron state, having a virtual energy level. There are four possibilities:

1. no energy exchange between the incident photons and the molecules (and hence no Raman effect)
2. energy exchanges occur between the incident photons and the molecules. The energy differences are equal to the differences of the vibrational and rotational energy-levels of the molecule. In crystals only specific photons are allowed (solutions of the wave equations which do not cancel themselves) by the periodic

structure, so Raman scattering can only appear at certain frequencies. In amorphous materials like glasses, more photons are allowed and thereby the discrete spectral lines become broad.

3. molecule absorbs energy: Stokes scattering. The resulting photon of lower energy generates a Stokes line on the red side of the incident spectrum.

4. molecule loses energy: anti-Stokes scattering. Incident photons are shifted to the blue side of the spectrum, thus generating an anti-Stokes line.

These differences in energy are measured by subtracting the energy of the mono-energetic laser light from the energy of the scattered photons. The absolute value, however, doesn't depend on the process (Stokes or anti-Stokes scattering), because only the energy of the different vibrational levels is of importance. Therefore, the Raman spectrum is symmetric relative to the Rayleigh band. In addition, the intensities of the Raman bands are only dependent on the number of molecules occupying the different vibrational states, when the process began. Thus lower energy states will have more molecules in them than will higher (excited) energy states. Therefore, the Stokes spectrum will be more intense than the anti-Stokes spectrum.

9 BIBLIOGRAPHY

- Aggeli, A., Nyrkova, I. A., Bell, M., Harding, R., Carrick, L., McLeish, T. C., Semenov, A. N. and Boden, N., (2001). Hierarchical self-assembly of chiral rod-like molecules as a model for peptide beta-sheet tapes, ribbons, fibrils, and fibers. *Proc Natl Acad Sci U S A* 98, 11857-11862.
- Al-Saffar, N., Revell, P. A. and Kobayashi, A., (1997). Modulation of the phenotypic and functional properties of phagocytic macrophages by wear particles from orthopaedic implants. *J Mater Sci Mater Med* 8, 641-648.
- Alvarez-Buylla, A. and Lim, D. A., (2004). For the long run: maintaining germinal niches in the adult brain. *Neuron* 41, 683-686.
- Apetri, M. M., Maiti, N. C., Zagorski, M. G., Carey, P. R. and Anderson, V. E., (2006). Secondary structure of alpha-synuclein oligomers: characterization by raman and atomic force microscopy. *J Mol Biol* 355, 63-71.
- Arrondo, J. L. and Goni, F. M., (1999). Structure and dynamics of membrane proteins as studied by infrared spectroscopy. *Prog Biophys Mol Biol* 72, 367-405.
- Baraldi, P. and Tinti, A., (2008). Raman spectroscopy in art and archaeology. *Journal of Raman Spectroscopy* 39, 963-965.
- Berry, C. C., Charles, S., Wells, S., Dalby, M. J. and Curtis, A. S. G., (2004). The influence of transferrin stabilised magnetic nanoparticles on human dermal fibroblasts in culture. *International Journal of Pharmaceutics* 269, 211-225.
- Bielschowsky, M., 1908. Eine modifikation meines silver-impregnationsverfahrens zur darstellung der neurofibrillen. In: *J. Psychol Neurol*), pp. 12: 135-137.
- Bini, T. B., Gao, S., Xu, X., Wang, S., Ramakrishna, S. and Leong, K. W., (2004). Peripheral nerve regeneration by microbraided poly(L-lactide-co-glycolide) biodegradable polymer fibers. *J Biomed Mater Res A* 68, 286-295.
- Brooks, B. R., Bruccoleri, R. E., Olafson, B. D., States, D. J., Swaminathan, S. and Karplus, M., (1983). Charmm - a Program for Macromolecular Energy, Minimization, and Dynamics Calculations. *Journal of Computational Chemistry* 4, 187-217.
- Bryan, D. J., Holway, A. H., Wang, K. K., Silva, A. E., Trantolo, D. J., Wise, D. and Summerhayes, I. C., (2000). Influence of glial growth factor and Schwann cells in a bioresorbable guidance channel on peripheral nerve regeneration. *Tissue Eng* 6, 129-138.

- Cai, J., Peng, X., Nelson, K. D., Eberhart, R. and Smith, G. M., (2005). Permeable guidance channels containing microfilament scaffolds enhance axon growth and maturation. *J Biomed Mater Res A* 75, 374-386.
- Carrier, D. and Pezolet, M., (1984). Raman-Spectroscopic Study of the Interaction of Poly-L-Lysine with Dipalmitoylphosphatidylglycerol Bilayers. *Biophysical Journal* 46, 497-506.
- Chacon, P., Tama, F. and Wriggers, W., (2003). Mega-Dalton biomolecular motion captured from electron microscopy reconstructions. *J Mol Biol* 326, 485-492.
- Chamberlain, L. J., Yannas, I. V., Hsu, H. P., Strichartz, G. and Spector, M., (1998). Collagen-GAG substrate enhances the quality of nerve regeneration through collagen tubes up to level of autograft. *Exp Neurol* 154, 315-329.
- Chew, S. Y., Mi, R., Hoke, A. and Leong, K. W., (2008). The effect of the alignment of electrospun fibrous scaffolds on Schwann cell maturation. *Biomaterials* 29, 653-661.
- Chun, Y. W. and Webster, T. J., (2009). The Role of Nanomedicine in Growing Tissues. *Annals of Biomedical Engineering* 37, 2034-2047.
- Colombo, G., Soto, P. and Gazit, E., (2007). Peptide self-assembly at the nanoscale: a challenging target for computational and experimental biotechnology. *Trends in Biotechnology* 25, 211-218.
- Cordeiro, Y., Lima, L. M. T. R., Gomes, M. P. B., Foguel, D. and Silva, J. L., (2004). Modulation of prion protein oligomerization, aggregation, and beta-sheet conversion by 4,4'-dianilino-1,1'-binaphthyl-5,5'-sulfonate (bis-ANS). *Journal of Biological Chemistry* 279, 5346-5352.
- Davis, M. E., Hsieh, P. C., Takahashi, T., Song, Q., Zhang, S., Kamm, R. D., Grodzinsky, A. J., Anversa, P. and Lee, R. T., (2006). Local myocardial insulin-like growth factor 1 (IGF-1) delivery with biotinylated peptide nanofibers improves cell therapy for myocardial infarction. *Proc Natl Acad Sci U S A* 103, 8155-8160.
- Davis, M. E., Motion, J. P., Narmoneva, D. A., Takahashi, T., Hakuno, D., Kamm, R. D., Zhang, S. and Lee, R. T., (2005). Injectable self-assembling peptide nanofibers create intramyocardial microenvironments for endothelial cells. *Circulation* 111, 442-450.
- De Gelder, J., De Gussem, K., Vandenabeele, P. and Moens, L., (2007). Reference database of Raman spectra of biological molecules. *Journal of Raman Spectroscopy* 38, 1133-1147.

- Dobson, C. M., (2000). Protein folding, misfolding, and disease. Abstracts of Papers of the American Chemical Society 219, U277-U277.
- Doussis, I. A., Puddle, B. and Athanasou, N. A., (1992). Immunophenotype of multinucleated and mononuclear cells in giant cell lesions of bone and soft tissue. *J Clin Pathol* 45, 398-404.
- Drotleff, S., Lungwitz, U., Breunig, M., Dennis, A., Blunk, T., Tessmar, J. and Gopferich, A., (2004). Biomimetic polymers in pharmaceutical and biomedical sciences. *Eur J Pharm Biopharm* 58, 385-407.
- Drury, J. L. and Mooney, D. J., (2003). Hydrogels for tissue engineering: scaffold design variables and applications. *Biomaterials* 24, 4337-4351.
- Dunetz, J. R., Sandstrom, C., Young, E. R., Baker, P., Van Name, S. A., Cathopolous, T., Fairman, R., de Paula, J. C. and Akerfeldt, K. S., (2005). Self-assembling porphyrin-modified peptides. *Org Lett* 7, 2559-2561.
- Elbert, D. L. and Hubbell, J. A., (2001). Conjugate addition reactions combined with free-radical cross-linking for the design of materials for tissue engineering. *Biomacromolecules* 2, 430-441.
- Ellis-Behnke, R. G., Liang, Y. X., Tay, D. K., Kau, P. W., Schneider, G. E., Zhang, S., Wu, W. and So, K. F., (2006). Nano hemostat solution: immediate hemostasis at the nanoscale. *Nanomedicine* 2, 207-215.
- Engel, E., Michiardi, A., Navarro, M., Lacroix, D. and Planell, J. A., (2008). Nanotechnology in regenerative medicine: the materials side. *Trends Biotechnol* 26, 39-47.
- Evans, G. R., (2000). Challenges to nerve regeneration. *Semin Surg Oncol* 19, 312-318.
- Fairman, R. and Akerfeldt, K. S., (2005). Peptides as novel smart materials. *Curr Opin Struct Biol* 15, 453-463.
- Foguel, D., Suarez, M. C., Ferrao-Gonzales, A. D., Porto, T. C. R., Palmieri, L., Einsiedler, C. M., Andrade, L. R., Lashuel, H. A., Lansbury, P. T., Kelly, J. W. and Silva, J. L., (2003). Dissociation of amyloid fibrils of alpha-synuclein and transthyretin by pressure reveals their reversible nature and the formation of water-excluded cavities. *Proceedings of the National Academy of Sciences of the United States of America* 100, 9831-9836.
- Fu, S. Y. and Gordon, T., (1997). The cellular and molecular basis of peripheral nerve regeneration. *Mol Neurobiol* 14, 67-116.

- Gambaretto, R., Tonin, L., Di Bello, C. and Dettin, M., (2008). Self-assembling peptides: Sequence, secondary structure in solution and film formation. *Biopolymers* 89, 906-915.
- Gelain, F., Bottai, D., Vescovi, A. and Zhang, S., (2006). Designer self-assembling Peptide nanofiber scaffolds for adult mouse neural stem cell 3-dimensional cultures. *PLoS ONE* 1, e119.
- Gelain, F., Horii, A. and Zhang, S., (2007a). Designer self-assembling peptide scaffolds for 3-d tissue cell cultures and regenerative medicine. *Macromol Biosci* 7, 544-551.
- Gelain, F., Lomander, A., Vescovi, A. L. and Zhang, S., (2007b). Systematic studies of a self-assembling peptide nanofiber scaffold with other scaffolds. *J Nanosci Nanotechnol* 7, 424-434.
- Goodman, C. S., Bastiani, M. J., Doe, C. Q., du Lac, S., Helfand, S. L., Kuwada, J. Y. and Thomas, J. B., (1984). Cell recognition during neuronal development. *Science* 225, 1271-1279.
- Guenard, V., Kleitman, N., Morrissey, T. K., Bunge, R. P. and Aebischer, P., (1992). Syngeneic Schwann cells derived from adult nerves seeded in semipermeable guidance channels enhance peripheral nerve regeneration. *J Neurosci* 12, 3310-3320.
- Hadlock, T., Elisseeff, J., Langer, R., Vacanti, J. and Cheney, M., (1998). A tissue-engineered conduit for peripheral nerve repair. *Arch Otolaryngol Head Neck Surg* 124, 1081-1086.
- Hadlock, T., Sundback, C., Hunter, D., Cheney, M. and Vacanti, J. P., (2000). A polymer foam conduit seeded with Schwann cells promotes guided peripheral nerve regeneration. *Tissue Eng* 6, 119-127.
- Hinsen, K., Reuter, N., Navaza, J., Stokes, D. L. and Lacapere, J. J., (2005). Normal mode-based fitting of atomic structure into electron density maps: application to sarcoplasmic reticulum Ca-ATPase. *Biophys J* 88, 818-827.
- Hirst, A. R. and Smith, D. K., (2004). Self-assembly of two-component peptidic dendrimers: dendritic effects on gel-phase materials. *Org Biomol Chem* 2, 2965-2971.
- Hoang, T. X., Trovato, A., Seno, F., Banavar, J. R. and Maritan, A., (2004). Geometry and symmetry presculpt the free-energy landscape of proteins. *Proc Natl Acad Sci U S A* 101, 7960-7964.
- Hohman M, M. S., G R, MP B, (2001). Electrospinning and electrically forced jets. II. Applications. *Physics of Fluids*. 13, 2221-2236.
- Horii, A., Wang, X., Gelain, F. and Zhang, S., (2007). Biological designer self-assembling Peptide nanofiber scaffolds

- significantly enhance osteoblast proliferation, differentiation and 3-D migration. *PLoS One* 2, e190.
- Hua, F. J., Kim, G. E., Lee, J. D., Son, Y. K. and Lee, D. S., (2002). Macroporous poly(L-lactide) scaffold 1. Preparation of a macroporous scaffold by liquid-liquid phase separation of a PLLA--dioxane--water system. *J Biomed Mater Res* 63, 161-167.
- Hwang, W., Zhang, S., Kamm, R. D. and Karplus, M., (2004). Kinetic control of dimer structure formation in amyloid fibrillogenesis. *Proc Natl Acad Sci U S A* 101, 12916-12921.
- Javor, S., Natalello, A., Doglia, S. M. and Reymond, J. L., (2008). alpha-Helix Stabilization within a Peptide Dendrimer. *J Am Chem Soc* 130, 17248-17249.
- Jun, S., Hong, Y., Imamura, H., Ha, B. Y., Bechhoefer, J. and Chen, P., (2004). Self-assembly of the ionic peptide EAK16: The effect of charge distributions on self-assembly. *Biophysical Journal* 87, 1249-1259.
- Karplus, M., (2003). Molecular dynamics of biological macromolecules: A brief history and perspective. *Biopolymers* 68, 350-358.
- Kasemo, B., 2002. Biological surface science. In: *Surface Science*), pp. 500: 656-677.
- Keeley, R. D., Nguyen, K. D., Stephanides, M. J., Padilla, J. and Rosen, J. M., (1991). The artificial nerve graft: a comparison of blended elastomer-hydrogel with polyglycolic acid conduits. *J Reconstr Microsurg* 7, 93-100.
- Kelly, J. W., (1998). The environmental dependency of protein folding best explains prion and amyloid diseases. *Proceedings of the National Academy of Sciences of the United States of America* 95, 930-932.
- King, V. R., Henseler, M., Brown, R. A. and Priestley, J. V., (2003). Mats made from fibronectin support oriented growth of axons in the damaged spinal cord of the adult rat. *Exp Neurol* 182, 383-398.
- Kirschner, D. A., Abraham, C. and Selkoe, D. J., (1986). X-Ray-Diffraction from Intraneuronal Paired Helical Filaments and Extraneuronal Amyloid Fibers in Alzheimer-Disease Indicates Cross-Beta Conformation. *Proceedings of the National Academy of Sciences of the United States of America* 83, 503-507.
- Kleinman, H. K., McGarvey, M. L., Hassell, J. R., Star, V. L., Cannon, F. B., Laurie, G. W. and Martin, G. R., (1986). Basement membrane complexes with biological activity. *Biochemistry* 25, 312-318.

- Koh, H. S., Yong, T., Chan, C. K. and Ramakrishna, S., (2008). Enhancement of neurite outgrowth using nano-structured scaffolds coupled with laminin. *Biomaterials* 29, 3574-3582.
- Luis, A. L., Rodrigues, J. M., Geuna, S., Amado, S., Shirosaki, Y., Lee, J. M., Fregnan, F., Lopes, M. A., Veloso, A. P., Ferreira, A. J., Santos, J. D., Armada-da-Silva, P. A., Varejao, A. S. and Mauricio, A. C., (2008). Use of PLGA 90:10 Scaffolds Enriched with In Vitro-Differentiated Neural Cells for Repairing Rat Sciatic Nerve Defects. *Tissue Eng Part A* 14, 979-993.
- Madaghiele, M., Sannino, A., Yannas, I. V. and Spector, M., (2008). Collagen-based matrices with axially oriented pores. *J Biomed Mater Res A* 85, 757-767.
- Maiti, N. C., Apetri, M. M., Zagorski, M. G., Carey, P. R. and Anderson, V. E., (2004). Raman spectroscopic characterization of secondary structure in natively unfolded proteins: alpha-synuclein. *Journal of the American Chemical Society* 126, 2399-2408.
- Marchesi, C., Pluderi, M., Colleoni, F., Belicchi, M., Meregalli, M., Farini, A., Parolini, D., Draghi, L., Fruguglietti, M. E., Gavina, M., Porretti, L., Cattaneo, A., Battistelli, M., Prella, A., Moggio, M., Borsa, S., Bello, L., Spagnoli, D., Gaini, S. M., Tanzi, M. C., Bresolin, N., Grimoldi, N. and Torrente, Y., (2007). Skin-derived stem cells transplanted into resorbable guides provide functional nerve regeneration after sciatic nerve resection. *Glia* 55, 425-438.
- Meek, M. F., den Dunnen, W. F., Robinson, P. H., Pennings, A. J. and Schakenraad, J. M., (1997). Evaluation of functional nerve recovery after reconstruction with a new biodegradable poly (DL-lactide-epsilon-caprolactone) nerve guide. *Int J Artif Organs* 20, 463-468.
- Meyer, D., Petta, M., Fouchet, M. H., Vadel, M., Schaefer, M., DugastZrihen, M. and Guillemot, M., (1996). Stabilization of the hydrophilic sphere of iobitridol, a new nonionic iodinated contrast agent. *Acta Radiologica* 37, 8-16.
- Micheletti, C., Carloni, P. and Maritan, A., (2004). Accurate and efficient description of protein vibrational dynamics: Comparing molecular dynamics and Gaussian models. *Proteins-Structure Function and Bioinformatics* 55, 635-645.
- Nagai, Y., Unsworth, L. D., Koutsopoulos, S. and Zhang, S., (2006). Slow release of molecules in self-assembling peptide nanofiber scaffold. *J Control Release* 115, 18-25.
- Natalello, A., Ami, D., Brocca, S., Lotti, M. and Doglia, S. M., (2005). Secondary structure, conformational stability and glycosylation

- of a recombinant *Candida rugosa* lipase studied by Fourier-transform infrared spectroscopy. *Biochemical Journal* 385, 511-517.
- Natalello, A., Santarella, R., Doglia, S. M. and de Marco, A., (2008). Physical and chemical perturbations induce the formation of protein aggregates with different structural features. *Protein Expression and Purification* 58, 356-361.
- Nevin, A., Osticioli, I., Anglos, D., Burnstock, A., Cather, S. and Castellucci, E., (2008). The analysis of naturally and artificially aged protein-based paint media using Raman spectroscopy combined with Principal Component Analysis. *Journal of Raman Spectroscopy* 39, 993-1000.
- Paino, C. L., Fernandez-Valle, C., Bates, M. L. and Bunge, M. B., (1994). Regrowth of axons in lesioned adult rat spinal cord: promotion by implants of cultured Schwann cells. *J Neurocytol* 23, 433-452.
- Panseri, S., Cunha, C., Lowery, J., Del Carro, U., Taraballi, F., Amadio, S., Vescovi, A. and Gelain, F., (2008). Electrospun micro- and nanofiber tubes for functional nervous regeneration in sciatic nerve transections. *BMC Biotechnol* 8, 39.
- Park, J., Kahng, B., Kamm, R. D. and Hwang, W., (2006). Atomistic simulation approach to a continuum description of self-assembled beta-sheet filaments. *Biophys J* 90, 2510-2524.
- Pitcher, G. M., Ritchie, J. and Henry, J. L., (1999). Paw withdrawal threshold in the von Frey hair test is influenced by the surface on which the rat stands. *J Neurosci Methods* 87, 185-193.
- Ramon, C. L., Cajal, Y. and Martinez, R. O., (2007). Effects of vitamin E on the response of the fetal middle cerebral artery to the pressure test. *J Matern Fetal Neonatal Med* 20, 133-139.
- Reddi, A. H., (2000). Morphogenesis and tissue engineering of bone and cartilage: inductive signals, stem cells, and biomimetic biomaterials. *Tissue Eng* 6, 351-359.
- Riehemann, K., Schneider, S. W., Luger, T. A., Godin, B., Ferrari, M. and Fuchs, H., (2009). Nanomedicine--challenge and perspectives. *Angew Chem Int Ed Engl* 48, 872-897.
- Rodriguez, F. J., Verdu, E., Ceballos, D. and Navarro, X., (2000). Nerve guides seeded with autologous schwann cells improve nerve regeneration. *Exp Neurol* 161, 571-584.
- Rutkowski, G. E., Miller, C. A., Jefthinija, S. and Mallapragada, S. K., (2004). Synergistic effects of micropatterned biodegradable conduits and Schwann cells on sciatic nerve regeneration. *J Neural Eng* 1, 151-157.

- Schaefer, M. and Karplus, M., (1996). A comprehensive analytical treatment of continuum electrostatics. *Journal of Physical Chemistry* 100, 1578-1599.
- Semino, C. E., (2008). Self-assembling peptides: from bio-inspired materials to bone regeneration. *J Dent Res* 87, 606-616.
- Sieminski, A. L., Semino, C. E., Gong, H. and Kamm, R. D., (2008). Primary sequence of ionic self-assembling peptide gels affects endothelial cell adhesion and capillary morphogenesis. *J Biomed Mater Res A* 87, 494-504.
- Spilker, M. H., Asano, K., Yannas, I. V. and Spector, M., (2001). Contraction of collagen-glycosaminoglycan matrices by peripheral nerve cells in vitro. *Biomaterials* 22, 1085-1093.
- Susi, H. and Byler, D. M. (Eds.), 1986. Resolution-enhanced Fourier transform infrared spectroscopy of enzymes, vol.130.
- Taraballi, F., Campione, M., Sassella, A., Vescovi, A., Paleari, A., Hwang, W. and Gelain, F., (2009). Effect of functionalization on the self-assembling propensity of beta-sheet forming peptides. *Soft Matter* 5, 660-668.
- Thomas, G. J., (1999). Raman spectroscopy of protein and nucleic acid assemblies. *Annual Review of Biophysics and Biomolecular Structure* 28, 1-+.
- Tinti, A., Di Foggia, M., Taddei, P., Torreggiani, A., Dettin, M. and Fagnano, C., (2008). Vibrational study of auto-assembling oligopeptides for biomedical applications. *Journal of Raman Spectroscopy* 39, 250-259.
- Tirion, M. M., (1996). Large Amplitude Elastic Motions in Proteins from a Single-Parameter, Atomic Analysis. *Phys Rev Lett* 77, 1905-1908.
- Torreggiani, A., Domenech, J., Atrian, S., Capdevila, M. and Tinti, A., (2008). Raman study of in vivo synthesized Zn(II)-metallothionein complexes: structural insight into metal clusters and protein folding. *Biopolymers* 89, 1114-1124.
- Torreggiani, A., Tamba, A., Bonora, S. and Fini, G., (2003). Raman and IR study on copper binding of histamine. *Biopolymers* 72, 290-298.
- Tsai, W. B., Wang, P. Y., Chang, Y. and Wang, M. C., (2007). Fibronectin and culture temperature modulate the efficacy of an avidin-biotin binding system for chondrocyte adhesion and growth on biodegradable polymers. *Biotechnol Bioeng* 98, 498-507.
- Ulijn, R. V. and Smith, A. M., (2008). Designing peptide based nanomaterials. *Chemical Society Reviews* 37, 664-675.
- Vleggeert-Lankamp, C. L., de Ruiter, G. C., Wolfs, J. F., Pego, A. P., van den Berg, R. J., Feirabend, H. K., Malessy, M. J. and

- Lakke, E. A., (2007). Pores in synthetic nerve conduits are beneficial to regeneration. *J Biomed Mater Res A* 80, 965-982.
- Vleggeert-Lankamp, C. L., Wolfs, J., Pego, A. P., van den Berg, R., Feirabend, H. and Lakke, E., (2008). Effect of nerve graft porosity on the refractory period of regenerating nerve fibers. *J Neurosurg* 109, 294-305.
- Weigel, T., Schinkel, G. and Lendlein, A., (2006). Design and preparation of polymeric scaffolds for tissue engineering. *Expert Review of Medical Devices* 3, 835-851.
- Y., U., H, T. and N., G., (1978). Studies on protein folding, unfolding and fluctuations by computer simulation. A three-dimensional lattice model of lysozyme. *Biopolymers* 17, 1531-1548.
- Yan, H., Nykanen, A., Ruokolainen, J., Farrar, D., Gough, J. E., Saiani, A. and Miller, A. F., (2008). Thermo-reversible protein fibrillar hydrogels as cell scaffolds. *Faraday Discussions* 139, 71-84; discussion 105-128, 419-120.
- Yang, F., Murugan, R., Wang, S. and Ramakrishna, S., (2005). Electrospinning of nano/micro scale poly(L-lactic acid) aligned fibers and their potential in neural tissue engineering. *Biomaterials* 26, 2603-2610.
- Yannas, I. V., (2001). *Tissue and organ regeneration in adults*. Springer 10.
- Yannas, I. V. and Hill, B. J., (2004). Selection of biomaterials for peripheral nerve regeneration using data from the nerve chamber model. *Biomaterials* 25, 1593-1600.
- Yannas, I. V., Zhang, M. and Spilker, M. H., (2007). Standardized criterion to analyze and directly compare various materials and models for peripheral nerve regeneration. *J Biomater Sci Polym Ed* 18, 943-966.
- Yokoi, H., Kinoshita, T. and Zhang, S. G., (2005). Dynamic reassembly of peptide RADA16 nanofiber scaffold. *Proceedings of the National Academy of Sciences of the United States of America* 102, 8414-8419.
- Zhang, S., (2003). Fabrication of novel biomaterials through molecular self-assembly. *Nat Biotechnol* 21, 1171-1178.
- Zhang, S., Holmes, T. C., DiPersio, C. M., Hynes, R. O., Su, X. and Rich, A., (1995). Self-complementary oligopeptide matrices support mammalian cell attachment. *Biomaterials* 16, 1385-1393.
- Zhang, S., Marini, D. M., Hwang, W. and Santoso, S., (2002). Design of nanostructured biological materials through self-assembly of peptides and proteins. *Curr Opin Chem Biol* 6, 865-871.

Zhang, Z., Shi, Y. and Liu, H., (2003). Molecular dynamics simulations of peptides and proteins with amplified collective motions. *Biophys J* 84, 3583-3593.